

SOLVING ATOMIC STRUCTURES USING STATISTICAL MECHANICAL SEARCHES ON
X-RAY SCATTERING DERIVED POTENTIAL ENERGY SURFACES

by

Christopher James Wright

Bachelor of Science
Brown University 2014

Submitted in Partial Fulfillment of the Requirements

for the Degree of Master of Science in

Chemical Engineering

College of Engineering and Computing

University of South Carolina

2016

Accepted by:

Xiao-Dong Zhou, Director of Thesis

Mark Uline, Reader

Jochen Lauterbach, Reader

John Weidner, Reader

Lacy Ford, Senior Vice Provost and Dean of Graduate Studies

© Copyright by Christopher James Wright, 2016
All Rights Reserved.

DEDICATION

To Diane & Donald Wright

My first scientific advisers

To see a World in a Grain of Sand

- William Blake

ACKNOWLEDGMENTS

This work would not have been possible without my entire ensemble of colleagues, advisers, friends, and family.

To my parents, I don't know if any language could correctly render the magnitude of my gratitude for everything you have done.

To Dr. Sanjit Ghose thank you very much for getting me started in the x-ray field and sticking with me, even when I went into the mathematical deep end.

To Dr. Yan Li, thank you very much for always pushing my simulations to be the best they could be, and pushing me to search every possible nook and cranny of parameter space.

To Daniel DeCiccio I am eternally grateful, you were with this project from the start and have always been a constant source of support, advice, and friendship.

To Dr. Thomas Caswell, Dr. Eric Dill, and Dr. Dan Allen, I would not be $1e^{-6}$ of the programmer I am today with out your guidance, conversation, and explanations.

To Prof. Scopatz, thank you very much for your insights, conversation, and being a spectacular developer role model.

To Emir Dogdibegovic, thank you very much for being my partner in beamtime. I hope you continue your x-ray work.

To my many readers, I'd like to say thank you, that is, if my thesis hasn't put you to sleep already. I'd also like to thank the NSLS-II XPD team for their experimental, intellectual, and moral support.

Last, but certainly not least, Prof. Zhou. I am certain that I could not have gotten a better start in research science than working with you.

ABSTRACT

Engineering the next generation of materials, especially nanomaterials, requires a detailed understanding of the material's underlying atomic structure. These structures give us better insight into structure-property relationships, allowing for property driven material design on the atomic level. Even more importantly, understanding structures *in-situ* will translate stimuli and responses on the macroscopic scale to changes on the nanoscale. Despite the importance of precise atomic structures for materials design, solving atomic structures is difficult both experimentally and computationally. Atomic pair distribution functions (PDFs) provide information on atomic structure, but the difficulty of extracting the PDF from x-ray total scattering measurements limits their use. Translating the PDF into an atomic structure requires the search of a very high dimensional space, the set of all potential atomic configurations. The large computational cost of running these simulations also limits the use of PDF as an atomistic probe.

This work aims to address these issues by developing 1) novel statistical mechanical approaches to solving material structures, 2) fast simulation of x-ray total scattering and atomic pair distribution functions (PDFs), and 3) data processing procedures for experimental x-ray total scattering measurements. First, experimentally derived potential energy surfaces (PES) and the statistical mechanical ensembles used to search them are developed. Then the mathematical and computational framework for the PDF and its gradients will be discussed. The combined PDF-PES-ensemble system will be benchmarked against a series of nanoparticle structures to ascertain the efficiency and effectiveness of the system. Experimental data processing proce-

dures, which maximize the usable data, will be presented. Finally, preliminary results from experimental x-ray total scattering measurements will be discussed. This work presents one of the most complete end-to-end systems for processing and modeling x-ray total scattering PDF data, potentially allowing for high-throughput structural solution.

TABLE OF CONTENTS

DEDICATION	iii
ACKNOWLEDGMENTS	iv
ABSTRACT	v
LIST OF FIGURES	x
CHAPTER 1 INTRODUCTION	1
CHAPTER 2 STATISTICAL MECHANICAL ENSEMBLES AND POTENTIAL ENERGY SURFACES	3
2.1 Introduction	3
2.2 Potential Energy Surfaces	3
2.3 Ensembles	6
2.4 Conclusions	13
CHAPTER 3 ATOMIC PAIR DISTRIBUTION FUNCTION: THEORY AND COMPUTATION	15
3.1 Introduction	15
3.2 Theory	16
3.3 Computation	19
3.4 Conclusions	26

CHAPTER 4 BENCHMARKS	27
4.1 Introduction	27
4.2 Structural Solutions	30
4.3 Discussion and Conclusion	38
 CHAPTER 5 X-RAY TOTAL SCATTERING DATA ACQUISITION AND PROCESSING	 41
5.1 Introduction	41
5.2 Detector Q resolution	41
5.3 Automated Mask Generation	43
5.4 Automated Image Azimuthal Integration	53
5.5 Conclusions	54
 CHAPTER 6 PHASE CHANGES AND ANNEALING DYNAMICS OF Pr_2NiO_4 AND ITS DERIVATIVES	 58
6.1 Introduction	58
6.2 Experiments	59
6.3 Data Processing	59
6.4 Data Analysis	60
6.5 Simulation	73
6.6 Conclusions	73
 CHAPTER 7 CONCLUSION	 75
 BIBLIOGRAPHY	 78

APPENDIX A SUPPLEMENTAL INFORMATION: PHASE CHANGES AND AN-
NEALING DYNAMICS OF Pr_2NiO_4 AND ITS DERIVATIVES . . . 84

LIST OF FIGURES

Figure 2.1	Addition biasing with a Lennard Jones potential.	14
Figure 3.1	Comparison of the CPU and GPU chip architectures	20
Figure 3.2	Speed comparison of CPU and GPU implementations	25
Figure 4.1	Au ₅₅ PDF fitting of DFT-optimized <i>c</i> -Au ₅₅ .	31
Figure 4.2	Au ₅₅ PDF fitting of surface-disordered Au ₅₅ .	32
Figure 4.3	Similar to figure 4.2 for DFT-optimized amorphous Au ₅₅ .	34
Figure 4.4	Similar to Fig. 4.2 for Au ₁₀₂ as in DFT-optimized Au ₁₀₂ MBA ₄₄ cluster.	36
Figure 4.5	Similar to Fig. 4.4 with Marks decahedron as the starting structure.	37
Figure 5.1	Scattering onto a flat detector	42
Figure 5.2	Q resolution as a function of Q .	43
Figure 5.3	Number of pixels as a function of Q , binned at the Q resolution of the detector.	44
Figure 5.4	Generated dead/hot pixel masks for a detector with 100 bad pixels.	46
Figure 5.5	Generated dead/hot pixel masks for a detector with 300 bad pixels.	47
Figure 5.6	Generated dead/hot pixel masks for a detector with 500 bad pixels.	47
Figure 5.7	Generated dead/hot pixel masks for a detector with 1000 bad pixels.	48
Figure 5.8	Generated beamstop holder masks for a beamstop holder with 10% transmittance.	48

Figure 5.9 Generated beamstop holder masks for a beamstop holder with 30% transmittance.	49
Figure 5.10 Generated beamstop holder masks for a beamstop holder with 50% transmittance.	49
Figure 5.11 Generated beamstop holder masks for a beamstop holder with 90% transmittance.	49
Figure 5.12 Generated beamstop holder masks which is rotated away from vertical.	50
Figure 5.13 Masked experimental data.	51
Figure 5.14 Masked experimental data with Pt single crystal signal.	51
Figure 5.15 Masked experimental data with Pt single crystal signal using figure's 5.13 mask as a starting mask.	52
Figure 5.16 Masking, average, and standard deviation of an example x-ray total scattering measurement with with no mask.	55
Figure 5.17 Masking, average, and standard deviation of an example x-ray total scattering measurement with with only an edge mask.	56
Figure 5.18 Masking, average, and standard deviation of an example x-ray total scattering measurement with combining an edge mask and the automatically generated mask.	57
Figure 6.1 PDF as a function of temperature for as synthesized PNO showing the full PDF	61
Figure 6.2 PDF as a function of temperature for as synthesized PNO showing a close up on the short range section	62
Figure 6.3 PDF as a function of temperature for PNO annealed at 750 °C for 25 hours showing the full PDF	63
Figure 6.4 PDF as a function of temperature for PNO annealed at 750 °C for 25 hours showing a close up on the short range section	64
Figure 6.5 $I(Q)$ as a function of temperature for as synthesized PNO showing the full XRD	66

Figure 6.6 $I(Q)$ as a function of temperature for as synthesized PNO showing a close up on the low Q section	67
Figure 6.7 $I(Q)$ as a function of temperature for PNO annealed at 750 °C for 25 hours showing the full XRD	68
Figure 6.8 $I(Q)$ as a function of temperature for PNO annealed at 750 °C for 25 hours showing a close up on the low Q section	69
Figure 6.9 Comparison of PNO sample PDFs as a function of annealing time high-temp	71
Figure 6.10 Comparison of PNO sample $I(Q)$ as a function of annealing time high-temp	72
Figure A.1 PDF as a function of temperature for PNO annealed at 750 °C for 50 hours showing the full PDF	85
Figure A.2 PDF as a function of temperature for PNO annealed at 750 °C for 50 hours showing a close up on the short range section	86
Figure A.3 PDF as a function of temperature for PNO annealed at 750 °C for 100 hours showing the full PDF	87
Figure A.4 PDF as a function of temperature for PNO annealed at 750 °C for 100 hours showing a close up on the short range section	88
Figure A.5 PDF as a function of temperature for PNO annealed at 750 °C for 200 hours showing the full PDF	89
Figure A.6 PDF as a function of temperature for PNO annealed at 750 °C for 200 hours showing a close up on the short range section	90
Figure A.7 $I(Q)$ as a function of temperature for PNO annealed at 750 °C for 50 hours showing the full XRD	91
Figure A.8 $I(Q)$ as a function of temperature for PNO annealed at 750 °C for 50 hours showing a close up on the low Q section	92
Figure A.9 $I(Q)$ as a function of temperature for PNO annealed at 750 °C for 100 hours showing the full XRD	93
Figure A.10 $I(Q)$ as a function of temperature for PNO annealed at 750 °C for 100 hours showing a close up on the low Q section	94

Figure A.11 $I(Q)$ as a function of temperature for PNO annealed at 750 °C for 200 hours showing the full XRD	95
Figure A.12 $I(Q)$ as a function of temperature for PNO annealed at 750 °C for 200 hours showing a close up on the low Q section	96
Figure A.13 Comparison of PNO sample PDFs as a function of annealing time at room temperature	98
Figure A.14 Comparison of PNO sample PDFs as a function of annealing time at room temperature	99
Figure A.15 Comparison of PNO sample PDFs as a function of annealing time at room temperature	100
Figure A.16 Comparison of PNO sample PDFs as a function of annealing time at room temperature	101
Figure A.17 Comparison of PNO sample PDFs as a function of annealing time at operating temperature	102
Figure A.18 Comparison of PNO sample PDFs as a function of annealing time at operating temperature	103
Figure A.19 Comparison of PNO sample PDFs as a function of annealing time at operating temperature	104
Figure A.20 Comparison of PNO sample PDFs as a function of annealing time at operating temperature	105
Figure A.21 Comparison of PNO sample PDFs as a function of annealing time cooled back to room temperature	106
Figure A.22 Comparison of PNO sample PDFs as a function of annealing time cooled back to room temperature	107
Figure A.23 Comparison of PNO sample PDFs as a function of annealing time cooled back to room temperature	108
Figure A.24 Comparison of PNO sample PDFs as a function of annealing time cooled back to room temperature	109
Figure A.25 Comparison of PNO sample $I(Q)$ as a function of annealing time at room temperature	110

Figure A.26 Comparison of PNO sample $I(Q)$ as a function of annealing time at operating temperature 111

Figure A.27 Comparison of PNO sample $I(Q)$ as a function of annealing time cooled back to room temperature 112

CHAPTER 1

INTRODUCTION

Engineering materials and chemicals on the atomic scale has long been a goal for the chemistry, physics, materials science, and chemical engineering fields. Realizing this goal could lead to more durable fuel cell catalysts, bioavailable pharmaceuticals, and radiation resistant shielding. Before we can even think of making atomistically exact, durable, or reproducibly changing structures, we need to know the precise atomic structure. This work bridges the gap in structural knowledge by developing a methodology for solving the structure of materials by matching experimental x-ray total scattering data with simulated atomic structures.

Chapter 2 develops the statistical mechanical system used to match experimental and theoretical structures. §2.2 focuses on potential energy surfaces, including potential energy and force equations, which have minima where experimental results and simulated structures agree the most. §2.3 will discuss the statistical mechanical ensembles which search the potential energy surface for minima.

Chapter 3 develops the mathematical and computational framework for the atomic pair distribution function (PDF). §3.3 will focus on the rapid graphical processing unit based calculation of the PDF and its gradients.

Chapter 4 will discuss the benchmarking of the the combined statistical mechanical optimizer and PDF calculation systems against a series of theoretical nanoparticles. These benchmarks will focus on understanding the limitations of the method and the relationship between goodness of fit and structure reproduction.

Chapter 5 will focus on the acquisition of experimental data, their management,

and processing. §5.2, 5.3, and 5.4 will discuss the derivation of the Q resolution function, the automated masking of 2D area detectors using the previously derived Q resolution, and the impact of different averaging methods and masks on azimuthal integration, respectively.

Chapter 6 will discuss preliminary experimental results investigating the phase changes and local structure of Pr_2NiO_4 , revealing the influence of thermal history on the structure. This chapter will also analyze the discrepancy between the reciprocal space scattering and the PDF.

CHAPTER 2

STATISTICAL MECHANICAL ENSEMBLES AND POTENTIAL ENERGY SURFACES

2.1 INTRODUCTION

The approach taken in this work for solving the atomic structures of materials is one of optimization. The plan is to develop a potential energy surface (PES) which has minima associated with atomic structures who's properties match the experimentally observed properties. Thus, the various positional variables of the structure can be solved by optimizing the structure against the PES. This approach is popular in the PDF community for solving the structure of materials using both extensive large box models and simpler small box models.

In this chapter we discuss the development of the various PESs used in the PDF community for comparing theoretical and experimental PDFs. Special attention will be paid to the gradients of the potential energy functions, as these are important to some optimization techniques. Additionally, we also discuss the use of statistical mechanical ensembles for finding minima on the PES.

2.2 POTENTIAL ENERGY SURFACES

A PES simply describes the potential energy of the system as a function of all its relevant coordinates in phase space, essentially providing a mapping $\mathbb{R}^n \rightarrow \mathbb{R}$, where \mathbb{R} is the set of real numbers and n is the number of positional parameters in the system. Usually these coordinates are the positions of the atoms q and their conjugate the

momenta p . Note that there could be more variables associated with the system, for instance the magnetic moments of the atoms could play a role in describing the system. In this magnetic system there would be positional variables for the atom-wise spin vectors and their "momenta". Application of the term "momenta" might seem odd here, as the magnetic spin does not have a mass or a velocity. However, since the magnetic "position" is defined on the PES we need to describe its conjugate variable to properly formulate Hamiltonian dynamics and the kinetic portion of the PES.

Experimentally Derived Potential Energy Surfaces

Generally PESs are obtained from purely computational experiments including: ab-initio DFT, classical approximations via the embedded atom method, or even parameter driven models with experimentally fitted parameters. However, one can derive a PES from an experiment which describes how well the model reproduces the experimental data. In this case one needs a theoretical and computational framework mapping the atomistic variables of the simulation to the same space of the data obtained from the experiment. This allows the experiment to be compared directly against the predicted data via an experimentally derived PES.

Potentials

For an experiment which produces 1D data, like powder diffraction, EXAFS or XPS, the implemented potentials are:

$$\chi^2 = \sum_{a=a_{\min}}^{a_{\max}} (A_{\text{obs}} - \alpha A_{\text{calc}})^2 \quad (2.1)$$

$$Rw = \sqrt{\frac{\sum_{a=a_{\min}}^{a_{\max}} (A_{\text{obs}} - \alpha A_{\text{calc}})^2}{\sum_{a=a_{\min}}^{a_{\max}} A_{\text{obs}}^2}} \quad (2.2)$$

$$\chi^2_{\text{INVERT}} = \frac{1}{N} \sum_j \sum_r [A_{\text{obs}}(r) - \alpha A_{j_{\text{calc}}}(r)]^2 \quad (2.3)$$

$$\alpha = \frac{\sum_{a=a_{\min}}^{a_{\max}} A_{\text{obs}} A_{\text{calc}}}{\sum_{a=a_{\min}}^{a_{\max}} A_{\text{calc}}^2} = \frac{\vec{A}_{\text{obs}} \cdot \vec{A}_{\text{calc}}}{|\vec{A}_{\text{calc}}|^2} \quad (2.4)$$

where A_{calc} and A_{obs} are the calculated and observed 1D experimental data and $A_{\text{calc},j}$ is the calculated data for a single atom interacting with the other atoms of the system. Note that A_{calc} has a dependence on q , the positions of the system. Rw and χ^2 potentials have been reported numerous times. [46, 35, 7, 36, 48] Essentially these potentials measure the least squares distance between the observed scattering and the predicted scattering providing a way to quantify the agreement between the model and experiment.

While Rw and χ^2 are now standard in the PDF community, the INVERT potential is fairly new and aims to incorporate descriptions of the structural symmetry into the PES. [10, 11] In the case of the INVERT potential NMR or other symmetry sensitive data is used to describe the number of unique atomic coordinations. This is then used to describe the number of unique atom-wise pair distribution functions, thus causing systems with more or less unique coordination environments to be higher in energy. This approach has been shown to be useful for C_{60} and other systems which are highly symmetric, creating a PES with an easier to find minima. [10, 11] However, many times this kind of data is unavailable when refining the structure causing the potential to be less useful. Additionally, this potential introduces an element of user bias as the refiner must decide, based on some spectroscopic data, how many unique environments are in the material. This bias could be removed by using one of the other potentials with a method for simulating the observed spectra, allowing the computational system decide what structures properly reproduce all the observed data.

Forces

$$\vec{\nabla} \chi^2 = -2 \sum_{a=a_{\min}}^{a_{\max}} (\alpha \frac{\partial A_{\text{calc}}}{\partial \gamma_{i,w}} + A_{\text{calc}} \frac{\partial \alpha}{\partial \gamma_{i,w}})(A_{\text{obs}} - \alpha A_{\text{calc}}) \quad (2.5)$$

$$\vec{\nabla} R w = \frac{R w}{\chi^2} \sum_{a=a_{\min}}^{a_{\max}} (\alpha \frac{\partial A_{\text{calc}}}{\partial \gamma_{i,w}} + A_{\text{calc}} \frac{\partial \alpha}{\partial \gamma_{i,w}}) (\alpha A_{\text{calc}} - (A_{\text{obs}})) \quad (2.6)$$

$$\vec{\nabla} \chi^2_{\text{INVERT}} = \frac{-2}{N} \sum_{a=a_{\min}}^{a_{\max}} \sum_j (\alpha \frac{\partial A_{j,\text{calc}}}{\partial \gamma_{i,w}} + A_{j,\text{calc}} \frac{\partial \alpha}{\partial \gamma_{i,w}}) (A_{\text{obs}} - \alpha A_{j,\text{calc}}) \quad (2.7)$$

$$\frac{\partial \alpha}{\partial \gamma_{i,w}} = \frac{(\sum_{a=a_{\min}}^{a_{\max}} A_{\text{obs}} \frac{\partial A_{\text{calc}}}{\partial \gamma_{i,w}} - 2\alpha \sum_{a=a_{\min}}^{a_{\max}} A_{\text{calc}} \frac{\partial A_{\text{calc}}}{\partial \gamma_{i,w}})}{\sum_{a=a_{\min}}^{a_{\max}} A_{\text{calc}}^2} \quad (2.8)$$

where $\gamma_{i,w}$ is the i th arbitrary positional variable in the w th direction. The concept of an "arbitrary positional variable" might seem a bit cumbersome but it allows us to define the forces for any atomic parameter which can be represented as a vector in 3-space. This comes in handy when trying to define the forces acting on variables like anisotropic displacement parameters or atomic magnetic spins.

2.3 ENSEMBLES

While PESs describe which atomic configurations are the most desirable and how the atoms would like to get there, the ensemble describes how the atoms move on the PES. The abstraction of the PES from the ensemble is an important one, as it allows for the reuse and exchange of both PESs and ensembles for a wide array of problems. Statistical mechanical ensembles can be described in two ways, analytically and scholastically. For long simulation times and fine enough numerical or analytical integration these two descriptions should be identical.

In either case one starts by defining the Hamiltonian, \mathcal{H} , as the total energy of the system. Thus, the Hamiltonian is described as the sum of the potential $U(q)$ and kinetic $K(p)$ energies, where q is the positions of the atoms and p is their momenta

$$\mathcal{H}(q, p) = U(q) + K(p) \quad (2.9)$$

where $K(p) = \frac{1}{2} \sum_i \frac{p_i^2}{m_i}$ and i denotes the i th particle.

Analytically one generally defines a partition function, which describes the sum of probabilities over all potential atomic states.

$$\Xi = \sum_i P_i(q, p) \quad (2.10)$$

where P_i is the probability of the i th state and is a function of the total energy of that state. This partition function can then be used to obtain the probability of any specific state. The relationship of the probability of a state to the state's energy and other properties depends on the ensemble being used.

For the canonical ensemble the partition function is probability is:

$$Q(N, V, T) = \exp\left(\frac{-\mathcal{H}(q, p)}{k_b T}\right) \quad (2.11)$$

where k_b is the Boltzmann constant and T is the temperature of the system. [37]

Monte Carlo Modeling

Monte Carlo can be used to simulate a statistical mechanical ensemble which can not be solved analytically. In most Monte Carlo systems the ensemble is simulated by randomly changing one of the system parameters and comparing the energy of the new system against the energy of the old system. If the energy of the new system is lower than the current energy then the new configuration is accepted. Otherwise the new system is rejected unless

$$\exp\left(\frac{-\Delta E}{E_T}\right) < u \quad (2.12)$$

where u is a random number $[0, 1)$ and E_T is the thermal energy characteristic to the system. The ability of Monte Carlo modeling to accept “bad” moves allows the system to hop out of local energy minima during the search for the global minimum. Reverse Monte Carlo (RMC) is similar to Monte Carlo except it uses χ^2 as the PES.[36]

Despite the utility of RMC, and its wide use in the x-ray scattering community, as Hoffman and Gelman state “Not all MCMC [Markov Chain Monte Carlo] algorithms

are created equal".[24] RMC, similar to standard Monte Carlo simulations, samples from the PES at random, usually by translating atoms in the system randomly. This creates a less efficient, random walk based, exploration of the PES.[24, 38] Thus, methods for suppressing this random walk nature, while still searching the potential energy surface fully are needed.

Hamiltonian Monte Carlo

Hybrid or Hamiltonian Monte Carlo (HMC) can help to address some of these issues. HMC was developed originally in the lattice quantum chromodynamics community and provides a more efficient, more scalable approach to PES sampling for Monte Carlo.[15, 39] In HMC the PES is explored using Hamiltonian dynamics, essentially following the gradient of the PES to find more acceptable configurations.

In order to model dynamics we need to describe the motion of the particles in our system, thus:

$$\frac{dq_i}{dt} = \frac{\partial \mathcal{H}}{\partial p_i} = p_i \quad (2.13)$$

$$\frac{dp_i}{dt} = -\frac{\partial \mathcal{H}}{\partial q_i} = -\vec{\nabla}U \quad (2.14)$$

Using these equations we can derive the position and momentum vectors at any point in time using the leap-frog algorithm:

$$p_i(t + \delta t/2) = p_i(t) - \frac{\delta t}{2} \frac{\partial}{\partial q_i} U(q(t)) \quad (2.15)$$

$$q_i(t + \delta t) = q_i(t) + \delta t * p_i(t + \delta t/2) \quad (2.16)$$

$$p_i(t + \delta t) = p_i(t + \delta t/2) - \frac{\delta t}{2} \frac{\partial}{\partial q_i} U(q(t + \delta t)) \quad (2.17)$$

Note that $\frac{\partial}{\partial q_i}$ is the gradient with respect to q where i denotes the i th atom being

moved. Using this notation the gradient is

$$\vec{\nabla}U = \begin{bmatrix} \frac{\partial U}{\partial q_{0,x}} & \frac{\partial U}{\partial q_{0,y}} & \frac{\partial U}{\partial q_{0,z}} \\ \vdots & \frac{\partial U}{\partial q_{i,w}} & \vdots \\ \frac{\partial U}{\partial q_{n,x}} & \frac{\partial U}{\partial q_{n,y}} & \frac{\partial U}{\partial q_{n,z}} \end{bmatrix} = \begin{bmatrix} \vec{\mathcal{F}}_0 \\ \vdots \\ \vec{\mathcal{F}}_i \\ \vdots \\ \vec{\mathcal{F}}_n \end{bmatrix} \quad (2.18)$$

where $\frac{\partial}{\partial q_{i,w}}$ is the derivative with respect to q where w denotes direction of the derivative (x , y , or z), n is the number of atoms and U is the potential which depends on q , and $\vec{\mathcal{F}}_i$ is the "force" on the i th atom. Using these equations new potential configurations are proposed from the PES. These proposals are checked against the standard Metropolis criteria discussed above, except that the change in potential energy ΔE is replaced with the change in the Hamiltonian $\Delta\mathcal{H}$. Note that while this sampling closely simulates the canonical ensemble, it is not exactly the same. Usually the canonical ensemble is formulated as microcanonical ensembles in contact with an infinite heat bath at a given temperature, or a set of microcanonical ensembles which exchange thermal energy. However, the HMC ensemble presented here has a momentum bath instead of a temperature bath. One could imagine the atoms sitting in a simulation box which has walls which can toggle their thermal exchange. Initially the box starts in the momentum bath, allowing the atoms to come to equilibrium with the bath momentum. The box is then removed from the bath causing it to become adiabatic. Hamiltonian dynamics are then propagated inside the box, essentially running a microcanonical simulation. Once the dynamics are finished the energy of the system is checked with the Metropolis criteria and the box is reintroduced to the momentum bath and the process starts again.

No-U-Turn Sampling

Two parameters must be specified in HMC simulations, the step size δ and the number of steps N . The step size is critical to the stability of the fitting procedure: with a too small δ the simulation runs inefficiently producing structures too close to the previous, whereas with a too big δ the linear approximation for the forces breaks down and often the simulated NP explodes. The number of steps to take during the dynamics is equally important and an inappropriate choice may result in backtracking or random walk characteristics in the simulations. In this work, we employ the No-U-Turn Sampling (NUTS) method recently proposed by Hoffman and Gelman to address this issue [24]. In the NUTS method δ and N are dynamically computed by examining the ratio of accepted to rejected configurations as well as whether or not the simulation has started to take a U-turn. The U-Turn criteria makes certain that the simulation stops when it begins to backtrack, preventing excess computation on configurations that have very little new information to offer. The use of NUTS leaves us with two simulation parameters: the simulation temperature and the target acceptance. Hoffman and Gelman have empirically shown that the ideal target acceptance, which governs the dynamics time steps, is .65, which we have used for all of the simulations here. The simulation temperature sets the magnitude of the random starting momenta for the atoms at the beginning of each dynamics run [24].

Grand Canonical Ensemble

While NUTS-HMC simulations provide a system to find minima on PESs, the simulation is fundamentally run in the Canonical Ensemble thus the variables in the simulation are limited to a fixed number of particles, simulation volume, and thermal energy. Fixing the thermal energy and simulation volume is not a problem, as they are not variables of interest in the final structure. However, specifying the number of atoms in the system can be problematic, as the exact number of atoms in a sample

can be difficult to count or a sample could have a distribution of particle sizes. Thus, a new ensemble needs to be used to allow the number of atoms to vary as a function of the PES. This new ensemble is the Grand Canonical Ensemble.

Ensemble description

In the Grand Canonical Ensemble (GCE) two sets of variables are allowed to change, the atomic positions, and the total number of atoms and their associated identities. These two variables are controlled by temperature, or average momentum, and chemical potential. The partition function is

$$\Xi = \sum_{N=0}^{\infty} Q(N, V, T) \exp \frac{N\mu\beta}{T} \quad (2.19)$$

where $Q(N, V, T)$ is the Canonical partition function discussed above, μ is the chemical potential. [37] This is translated into a Monte Carlo system, producing Grand Canonical Monte Carlo (GCMC).

Grand Canonical Monte Carlo

While the probabilities for atomic motion are the same as in the Canonical Ensemble, the addition or removal of an atom have their own probabilities. For the addition of an atom the probability is formally:

$$\min[1, \frac{V}{(N+1)\Lambda(T)^3} e^{-\beta\Delta U + \beta\mu}] \quad (2.20)$$

Similarly the removal of an atom has the probability:

$$\min[1, \frac{(N)\Lambda(T)^3}{V} e^{-\beta\Delta U - \beta\mu}] \quad (2.21)$$

However, both of these equations depend of the overall simulation volume and the thermal wavelength, which is undesirable as these are not really properties that we are of interest to these simulations. Thus, we roll them into the definition of the chemical potential, essentially setting the base chemical potential to counteract these

effects. This makes certain that our simulation does not change if we change the overall cell volume. A GCMC move consists of creating a new atomic configuration, where an atom has been added or removed, and checking the above criteria. However, previous results have shown that this method is computationally expensive in dense liquids, and exceedingly expensive in solid materials. The long simulation times are due to the random nature of the atomic additions or removals which produce: over-tightly packed atoms, atoms in the middle of nowhere, or nonphysical vacancies. These configurations are rejected by the GCMC criteria but their probability of being sampled is much higher than configurations which are lower in energy, since the number of incorrect ways to add/remove atoms is much larger than the correct ways. Thus, we have implemented methods for biasing the atomic addition positions and the atomic removals toward configurations which are more likely to be accepted.

GCMC biasing

The basic idea of GCMC biasing is mapping, in 3 dimensions, where an atomic addition or removal is most likely to be accepted. Thus, the simulation volume is broken up into voxels, 3 dimensional volumes which are contained by the total simulation volume, with a pre-set size. Each voxel is given a probability of being chosen for a trial insertion where the probability is:

$$P_{i,j,k} = \frac{e^{\beta\Delta U_{i,j,k}}}{\sum_{i,j,k} e^{\beta\Delta U_{i,j,k}}} \quad (2.22)$$

where $\Delta U_{i,j,k}$ is the change in energy. However, calculating $\Delta U_{i,j,k}$ can be particularly expensive, especially when calculating scattering from atomic positions. The computational expense can be mitigated by using a cheaper potential, if only for the evaluation of the voxel energy, as previously shown. Similar to previous work we can use the Lennard Jones potential to approximate the addition potential, lowering the computational burden. [52]

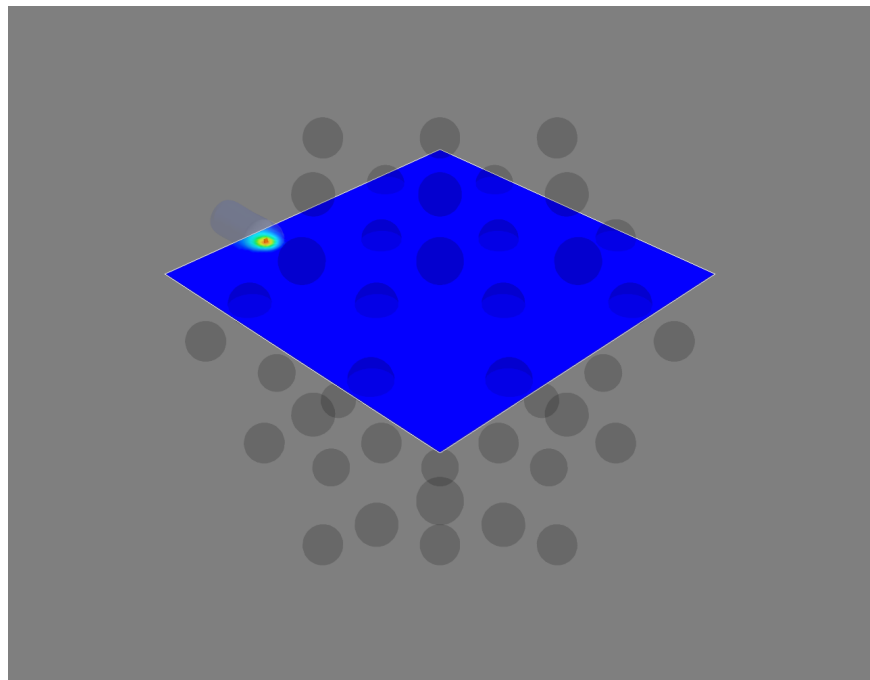
Atomic deletion follows a similar biasing procedure, calculating the energy of each atom and biasing the probability of each atom to be chosen for removal by its energy. This way atoms which add the most energy to the system are more likely to be removed.

Figure 2.1a shows an example map for atomic addition in a Au54 atom system, with an Au55 atom target. Figure 2.1b shows the results of a few GCMC insertions with biasing, showing the focusing of the simulation on the missing atom. The high density of insertions around the missing atom would not have been possible without the biasing.

2.4 CONCLUSIONS

In this chapter we have presented the development of both PES and the statistical mechanical ensembles used to search them. We expanded the classical concept of a PES to a more general mapping from positional variable space to energy space. This expansion allowed for the implementation of experimentally derived PES, where the disagreement between experimental and computed results can be included in the PES. Common experimental PESs were discussed, and their forces derived. The implementation of various statistical mechanical ensembles, used for searching the PES for minima, was also discussed with a special focus on No-U-Turn-Sampling Hamiltonian Monte Carlo. Grand Canonical Monte Carlo was also discussed, with an emphasis on the use of biasing to increase the overall acceptance rate. Future work in this area may include the development of PESs which leverage 2 dimensional data, like STEM images, or ensembles which help to eliminate tuned parameters like parallel tempering.

(a)



(b)

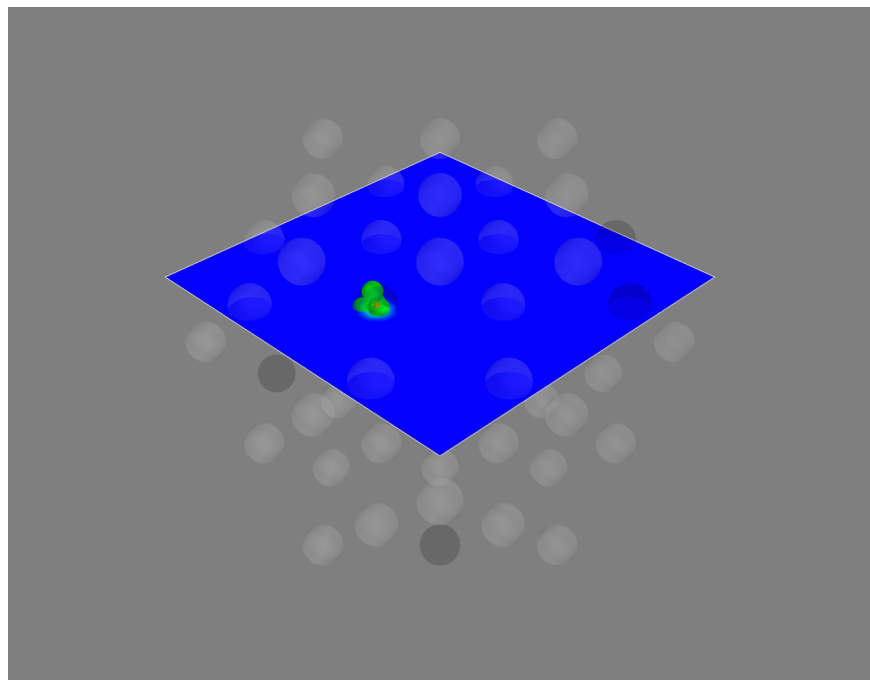


Figure 2.1: These figures show slices of the three dimensional addition potential energy surface. a) shows the addition probability, with the red area most probable. b) shows the results of trial insertions, where the green spheres denote where insertions were attempted.

CHAPTER 3

ATOMIC PAIR DISTRIBUTION FUNCTION: THEORY AND COMPUTATION

3.1 INTRODUCTION

Atomistic structural insight is essential for understanding and controlling a material’s properties and functions, which has led to some of the most exciting advances in modern materials science and engineering. X-ray diffraction techniques are one of the most powerful tools for probing atomic structures with ultimate precision. Traditionally, thousands of diffraction peaks are analyzed using refinements of a structural model with few parameters to determine the 3D structure of bulk single crystals with high precision [21]. However, real engineered materials differ from ideal single crystals by showing a complexity in morphology, crystallite size, and atomic structure. The X-ray Powder Diffraction method (XPD) is among the most widely used methods for solving the structure of micro-crystals. The XPD technique utilizes hundreds of diffraction peaks and constrains the refinement of the structural model to few parameters in order to resolve the structure [42]. Solving the atomic structure becomes difficult using traditional x-ray diffraction techniques when the size of the material or its important features is reduced to the nanometer scale with non-periodic or short-periodic atomic arrangements. Materials consisting of particles with sizes less than a few tens of nanometers, often called nanoparticles (NPs), are structurally more complex than their bulk cousins. This structural complexity is often attributed to the large number of surface atoms which have incomplete coordination spheres [53],

surface relaxation [25], and surface environment effects [47, 23, 34]. These effects make the precise determination of 3D atomic structure of NPs far more complicated and problematic [4].

Over the years many advances have been made to address the famous “nanostructure problem”[4], for example, by using the atomic Pair Distribution Function (PDF) analysis of x-ray and neutron total scattering data [17, 40, 48], PDF analysis combined with molecular dynamics simulations [56, 22], bulk crystallography approaches [26], and others. Attempts with non-diffraction based approaches have also been made, including Transmission Electron Microscopy (TEM) [12], Raman spectroscopy[29], Extended X-ray Absorption Fine-Structure Spectroscopy (EXAFS)[20] and Nuclear Magnetic Resonance (NMR) [2].

In this chapter the PDF and its gradients will be derived. These expressions, when combined with the PES and statistical mechanical treatment from chapter 2, will allow for the solution of atomic structures. This chapter will also develop a computational framework for evaluating the PDF and its gradients using Graphical Processing Units (GPUs) to enable fast structural solution.

3.2 THEORY

To properly understand the PDF and its limitations we need to derive its mathematics. The PDF has been previously derived many times so it is not re-derived here. This discussion of the PDF and its gradients use the notation of Farrow and Billinge. [18]

Derivation

Many of the above techniques require the gradient of the PES. This in turn requires the gradient of the PDF to be derived. Mathematically treating thermal vibrations will also be discussed in this section. Systems which are truly extended materials, like

powders with particle sizes larger than 10nm, are best formulated as systems with periodic boundaries. Thus, the equations for a periodically bound PDF need to be developed as well, with their gradients.

Analytically Gradients

Many optimization algorithms and simulations methodologies, including HMC, require not only the potential energy of a given configuration but also the forces acting on that configuration. These forces are described by the gradient of potential energy of the system which in turn requires the gradient of the PDF. As previously shown the PDF is the Fourier Transform of the Debye equation. Since the Fourier Transform is expressed as an integral we can exchange the order of the gradient and the integral, allowing us to calculate the analytical gradient of the Debye equation and Fast Fourier Transform (FFT) the resulting function. The Debye equation, with a Debye-Waller vibrational correction is

$$F(Q) = \frac{1}{N\langle f \rangle^2} \sum_{j \neq i} f_i^*(Q) f_j(Q) \exp\left(-\frac{1}{2}\sigma_{ij}^2 Q^2\right) \frac{\sin(Qr_{ij})}{r_{ij}} \quad (3.1)$$

where

$$\sigma_{ij}^2 = (\vec{u}_{ij} * \hat{d}_{ij})^2 \quad (3.2)$$

$$\vec{u}_{ij} = \vec{u}_i - \vec{u}_j \quad (3.3)$$

$$\hat{d}_{ij} = \frac{\vec{d}_{ij}}{r_{ij}} \quad (3.4)$$

$$r_{ij} = \|\vec{d}_{ij}\| \quad (3.5)$$

$$\vec{d}_{ij} = \begin{bmatrix} q_{ix} - q_{jx} \\ q_{iy} - q_{jy} \\ q_{iz} - q_{jz} \end{bmatrix} \quad (3.6)$$

where Q is the scatter vector, f_i is atomic scattering factor of the i th atom, \vec{u}_i is the anisotropic displacement parameter (ADP) for the i th atom and r_{ij} is the distance

between atoms i and j and has q dependence. [27] The ADPs measure the magnitude and direction of atomic thermal motion. For simplicity's sake we will break up $F(Q)$ so that

$$F(Q) = \alpha \sum_{j \neq i} \beta_{ij} \tau_{ij} \Omega_{ij} \quad (3.7)$$

where

$$\alpha = \frac{1}{N\langle f \rangle^2} \quad (3.8)$$

$$\beta_{ij} = f_i^*(Q) f_j(Q) \quad (3.9)$$

$$\tau_{ij} = \exp(-\frac{1}{2} \sigma_{ij}^2 Q^2) \quad (3.10)$$

$$\Omega_{ij} = \frac{\sin(Qr_{ij})}{r_{ij}} \quad (3.11)$$

The derivatives are as follows:

$$\frac{\partial}{\partial q_{i,w}} F(Q) = \alpha \sum_j \beta_{ij} \left(\frac{\partial \tau_{ij}}{\partial q_{i,w}} \Omega_{ij} + \tau_{ij} \frac{\partial \Omega_{ij}}{\partial q_{i,w}} \right) \quad (3.12)$$

where

$$\frac{\partial \Omega_{ij}}{\partial q_{i,w}} = \frac{Q \cos(Qr_{ij}) - \Omega_{ij}}{r_{ij}^2} (q_{i,w} - q_{j,w}) \quad (3.13)$$

$$\frac{\partial \tau_{ij}}{\partial q_{i,w}} = \frac{\sigma_{ij} Q^2 \tau_{ij}}{r_{ij}^3} ((q_{i,w} - q_{j,w}) \sigma_{ij} - (u_{i,w} - u_{j,w}) r_{ij}^2) \quad (3.14)$$

Since \vec{u}_{ij} is a variable as well, we need the derivative with respect to it as well.

Thus

$$\frac{\partial}{\partial u_{i,w}} F(Q) = \alpha \sum_j \beta_{ij} \frac{\partial \tau_{ij}}{\partial u_{i,w}} \Omega_{ij} \quad (3.15)$$

$$\frac{\partial \tau_{ij}}{\partial u_{i,w}} = -\frac{\sigma_{ij} Q^2 \tau_{ij}}{r_{ij}} (q_{i,w} - q_{j,w}) \quad (3.16)$$

Without ADPs

Without ADPs the equations simplify down to

$$F(Q) = \frac{1}{N\langle f \rangle^2} \sum_{j \neq i} f_i^*(Q) f_j(Q) \frac{\sin(Qr_{ij})}{r_{ij}} \quad (3.17)$$

and

$$\frac{\partial}{\partial q_{i,w}} F(Q) = \alpha \sum_j \beta_{ij} \frac{\partial \Omega_{ij}}{\partial q_{i,w}} \quad (3.18)$$

use of these equations, when ADPs are not appropriate (like at cryogenic temperatures), greatly speeds up the computation.

Periodic Boundary Conditions

Periodic boundary conditions can be helpful when simulating extended solids or large nanoparticles. In this case all the non-crystallinity is contained within the simulation box and the box is repeated to create the longer distance peaks observed in the PDF. To perform this we can break up the Debye equation into two main parts, the part that describes the interatomic distances within the simulation box and those between boxes. Neglecting the thermal motion portion:

$$F(Q) = \frac{1}{N\langle f \rangle^2} \left(\sum_{j \neq i} f_i^*(Q) f_j(Q) \frac{\sin(Qr_{ij})}{r_{ij}} + \sum_{i,j} f_i^*(Q) f_j(Q) \frac{\sin(QR_{ij})}{R_{ij}} \right) \quad (3.19)$$

where

$$R = |\vec{r} + \vec{\nu}| \quad (3.20)$$

$$\vec{\nu} = \gamma_1 * \vec{a} + \gamma_2 * \vec{b} + \gamma_3 * \vec{c} \quad (3.21)$$

where γ_i is the number of copies of the simulation box in the i th direction, and $\vec{a}, \vec{b}, \vec{c}$ are the lattice or superlattice directions.

3.3 COMPUTATION

Simply deriving the equations for the PDF is not enough. The many body nature of the PDF equation make analytical solution of the structure from the PDF impossible. Thus, the PDF must be computed from a structural candidates and compared against experimental results to evaluate the reliability of the model. These computations were implemented using high performance or high throughput computing methods (HPC or HTC) and Graphical Processing Units to provide quicker solutions.

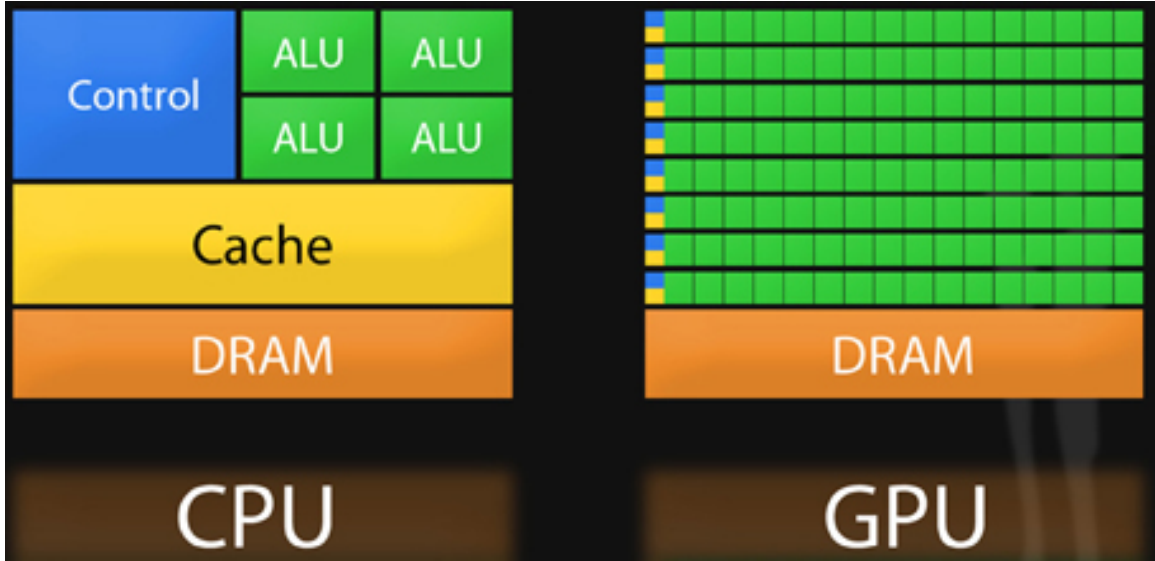


Figure 3.1: Comparison of the central processing unit (CPU) and GPU chip architectures from [6]. The arithmetic logic unit (ALU) are the arithmetic logic units which perform the mathematical operations, the dynamic random-access memory (DRAM) holds most of the data, although it is slower to access, the Cache holds rapidly accessed data, and the Control controls the execution of software. Note the greater number of ALUs on the GPU, the comparatively smaller cache, and the allocation of caches and controls to entire rows of processors.

HPC and GPUs

To properly solve the structure of materials the PDF will need to be computed many times and checked against experimental results. This requires computation of the PDF, potentially over many atoms. Calculating these PDFs requires a fast, highly parallelized, computational framework.

Gpus and Parallelization

Computing the PDF is an embarrassingly parallel problem. The basic procedure is to calculate the reduced structure factor $F(Q)$ for each atom pair and momentum transfer vector, sum over all the atom pairs, and Fourier transform the structure to the PDF. The first part of this procedure is perfectly parallelizable, as each atom pair is separate from the others. The summation over all the atomic reduced structure factors can be parallelized via distributed summing. Lastly the FFT can be parallelized using

existing algorithms.

Graphical Processing Units (GPUs) are particularly well suited to the task of computing PDFs. GPU chip architecture is designed to perform many task simultaneously by having potentially thousands of cores. Figure 3.1 show the comparison of CPU and GPU architectures. As the figure shows the GPUs have a very different layout of computational processors (ALUs) and memory. While each ALU is simpler on the GPU, requiring the instructions to be less demanding in terms of memory, there are many more of them. The greater number of processors allows each atomic pairing to be placed on its own processor, so long as the math can be broken into simpler operations. The equations are broken up on the GPUs into various pieces which correspond to the α, β, τ and Ω as shown in equations 3.8-3.11 and sub-equations as needed. For example, while β is computed in one step, Ω requires the computation of the displacement array, then the distance array and finally the Ω array. The exact breakdown of processes, how the problems are broken down and spread across the processor has been optimized for speed and reliability.

Map from ij space to k space

The above equations, although formally correct, are very inefficient. $F(Q)$ and its gradient are indexed over all the atoms twice, however there are symmetries that allow us to only compute over the atom pairs essentially mapping from an $n \times n$ space, ij space, to a $\frac{n(n-1)}{2}$ space, k space. For $F(Q)$ we apply the following mapping where

$$\begin{array}{ccccc} & & \psi & & \\ E & \xrightarrow{\quad} & E' & \xrightarrow{\Sigma} & Z \\ \phi \downarrow & & & \nearrow \Sigma' & \\ B & \xrightarrow{\quad} & B' & \xrightarrow{\psi'} & \end{array}$$

E denotes the atomic coordinates in ij space, E' denotes $F(Q)$ before the summation

in ij space, B denotes the atomic pairs in k space, B' denotes $F(Q)$ in k space, and Z denotes the final summed $F(Q)$. For the operators, ϕ denotes the mapping from ij space to k space $k = j + i * \frac{i-1}{2}$, ψ and ψ' denote the $F(Q)$ operation in ij and k space, respectively. Σ denotes the sum over all the atoms.

To properly define Σ' we must establish whether $F(Q)$ is an even function. We can accomplish this by examining each of the portions of $F(Q)$, $\alpha, \beta, \tau, \Omega$. Ω is even, since r_{ij} is the interatomic distance, which is the same despite a flip of indices, Q does not depend on the atomic indices, and since Qr_{ij} is even so is $\sin Qr_{ij}$. Thus, Ω is even. Providing similar analysis to τ we can see that while \vec{u}_{ij} is odd, so is the unit displacement vector between the two atoms, thus the two odds cancel out. Intuitively this makes sense, since the $F(Q)$ equation is fundamentally interested in the interatomic distances which is even. Thus, switching atom indices does not change $F(Q)$. Due to the even nature of the $F(Q)$ operator the Σ' operator sums over all the atom pairs, and multiplies by two to reflect the double counting of the Σ operator.

For the gradient a similar mapping is used:

$$\begin{array}{ccccc} & & \psi & & \\ E & \xrightarrow{\quad} & E' & \xrightarrow{\Sigma} & Z \\ \phi \downarrow & & & \nearrow \tilde{\phi}\Sigma & \\ B & \xrightarrow{\quad} & B' & & \end{array}$$

In this mapping, however, we use the $\tilde{\phi}\Sigma$ operator. This operator simultaneously performs a reverse mapping from k to ij space, and a summation with the correct symmetry. In this case the ψ and ψ' operators, which denote the $\vec{\nabla}F(Q)$ operator in ij and k space, are antisymmetric. Intuitively this makes sense as an extension of Newton's Second Law, since each particle's interaction is felt oppositely by its partner.

GPU Memory Allocation

While GPUs are very fast computational engines they tend to be memory bound. While a gradient array for a 10nm Au nanoparticle, consisting of 31,000 atoms and half a billion unique distances, occupies 1.5 TB of memory a single GPU's RAM allotment varies from 4GB on a NVIDIA GTX970 to 24 GB on a NVIDIA Tesla K80. Thus, it is important to determine exactly how many atoms can fit on a GPU of arbitrary size as a function of the number of atoms and the Q range. The memory required per array is:

$$q[=]3n \quad (3.22)$$

$$d[=]3k \quad (3.23)$$

$$r[=]k \quad (3.24)$$

$$scatter[=]nQ \quad (3.25)$$

$$normalization[=]kQ \quad (3.26)$$

$$\Omega[=]kQ \quad (3.27)$$

$$F_k(Q)[=]kQ \quad (3.28)$$

$$Sum[=]kQ \quad (3.29)$$

$$Sum2[=]kQ \quad (3.30)$$

$$F(Q)[=]Q \quad (3.31)$$

where n is the number of atoms, k is the number of unique distances, Q is the scatter vector, and the $[=]$ operator denote the number of single precision floating point values in memory. Each of the above arrays are used in the computation and thus must be able to be held in memory. Thus the number of atom pairs that can fit on a GPU with am bytes of available memory is:

$$k_{perGPU} = \frac{1}{16Q + 16} (-4Qn - 4Q + am - 12n) \quad (3.32)$$

If ADPs are included in the calculation, then the following arrays are also added to the memory allocation:

$$adps = 3n \quad (3.33)$$

$$\sigma = k \quad (3.34)$$

$$\tau = kQ \quad (3.35)$$

Thus the pair allotment is:

$$k_{perGPU} = \frac{-4Qn - 4Q + am - 24n}{20Q + 20} \quad (3.36)$$

For the Gradient we need to calculate $F(Q)$ and its gradient, so the total memory overhead is equal to the previously mentioned arrays plus:

$$\vec{\nabla}\Omega = 3kQ \quad (3.37)$$

$$\vec{\nabla}F_k(Q) = 3kQ \quad (3.38)$$

$$\vec{\nabla}F_n(Q) = 3nQ \quad (3.39)$$

Thus the gradient allotment is:

$$\vec{\nabla}k_{perGPU} = \frac{-16Qn + am - 12n}{32Q + 16} \quad (3.40)$$

For the gradient with ADPs the ADP gradient array is:

$$\vec{\nabla}\tau = 3kQ \quad (3.41)$$

Thus the allocation is:

$$\vec{\nabla}k_{perGPU} = \frac{-16Qn + am - 24n}{48Q + 20} \quad (3.42)$$

These equations were solved by sympy as their validity is very important to the overall reliability of the software. If the GPU is over allocated then the system may crash or return meaningless results.

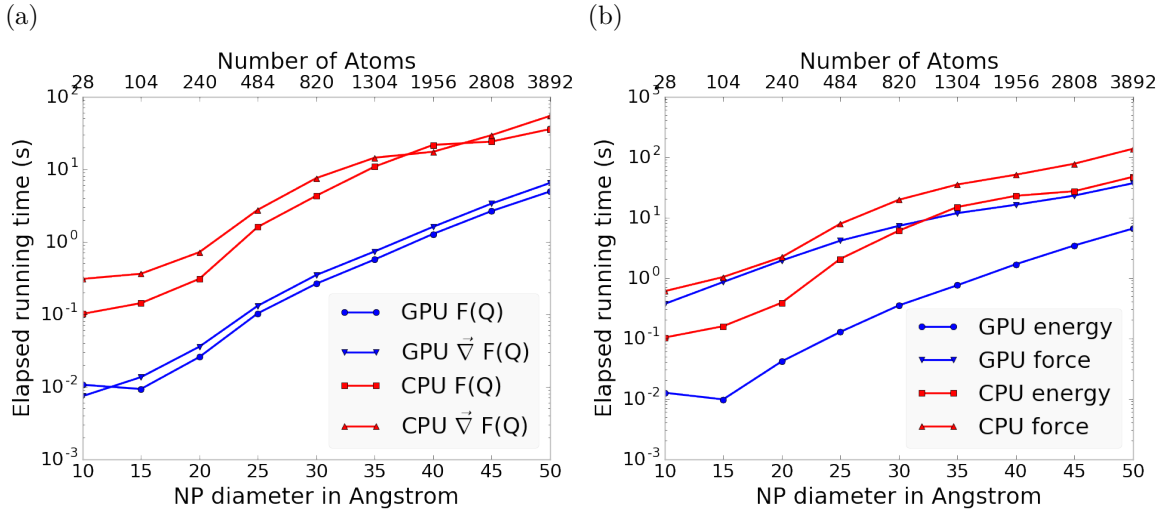


Figure 3.2: Speed comparison of CPU and GPU implementations. a) shows the time to compute the $F(Q)$ by itself. b) shows the time to compute the Rw based energy for Au NPs of various sizes, which includes computing $F(Q)$, its FFT, and the Rw .

Speed and Scaling of PDF Computation

To understand exactly how much the GPUs speed up the computation of $F(Q)$ and the PDF a series of time studies were run Au nanoparticles of varying size. Figure 3.2 shows the results of these time studies. CPU and GPU calculations were carried out on an Intel i7-4820K @3.70GHz Quad-Core and one NVIDIA GTX970s, respectively. The $F(Q)$ computations show a 100x to 10x speedup using the GPUs over the CPUs. Additionally, the $\vec{\nabla} F(Q)$ and $F(Q)$ computations seem to have similar computation time and scaling relationships on the GPU. This implies that the two processes may have similar bottlenecks, most likely in the $F(Q)$ computation workflow. This relationship is similarly preserved, although to a lesser extent, in the CPU scaling.

Interestingly, the tight run time relationship between $F(Q)$ and its gradient are not preserved in the Rw based force calculations. While the energy calculations are very similar to the $F(Q)$ calculations in terms of run time, the GPU and CPU force calculations are much closer, with the GPU calculations being much slower. This is

due to the force bottleneck being the $3n$ FFT operations which must be performed on the $\vec{\nabla}F(Q)$ array to produce the $\vec{\nabla}\text{PDF}$ array. While the GPU is leveraged to perform the FFT, the data must be loaded off the GPU and back on, causing a potential slowdown. Larger systems of atoms were not tried as the CPU computation quickly becomes very slow. Even higher GPU speedup is expected on more advanced GPUs like the NVIDIA Tesla series.

3.4 CONCLUSIONS

In this chapter we developed the gradients of the PDF in the discrete and periodic boundary condition case. We also developed the computational implementation of the PDF equations. This implementation emphasized use of GPUs to compute the PDF and its gradient. The GPU software was further sped up by mapping the computation to atom pairs rather than atom by atom. Finally, the speed of the GPU implementation was checked against the CPU implementation via speed benchmarking.

CHAPTER 4

BENCHMARKS

4.1 INTRODUCTION

Having developed the ensemble, PES, and PDF mathematics in chapters 2 and 3 this chapter will now benchmark the system to check its ability to produce reasonable structures from PDFs. The benchmarks shown here are certainly not exhaustive, nor are they even all the benchmarks run against the NUTS-HMC system. However, they do provide a good window into the workings, limitations, and abilities of the system.

The formation of NPs with both crystallographic and non-crystallographic structures [34] and with different chemical patterns [19] are well documented. For simplicity, we chose monometallic Au clusters as benchmarks and considered two groups of structures with different size and degrees of structural disorder in order to assess the reliability and efficiency of our HMC method for solving atomic structures from PDFs. The first group consists of Au_{55} clusters with different degrees of disorder, including a crystalline cluster structure in O_h (Octahedral) symmetry, a structure with a disordered surface, and an amorphous structure. The second group consists of the crystallographically solved Au_{102} structure as in the $\text{Au}_{102}\text{MBA}_{44}$ nanocrystals [26, 33]. We used optimized structures from the Density Functional Theory (DFT) as target structures and generated the corresponding PDF, G_{obs} , according to

$$G_{\text{obs}} = \frac{2}{\pi} \int_{Q_{\min}}^{Q_{\max}} Q[S_{\text{obs}}(Q) - 1] \sin(Qr) dQ \quad (4.1)$$

where S_{obs} is the target structure's structure factor. Since all the target structures

were optimized by DFT at zero Kelvin the target and model PDF profiles were calculated at zero temperature, with no atomic displacement parameters (ADPs). However, ADPs would have a considerable impact on the calculation of the PDF, especially for nanoparticles at non-zero temperatures.

Target Setup

Spin-polarized DFT calculations were carried out using the Vienna ab initio simulation package (VASP) [32, 31] within the Perdew-Burke-Ernzerhof (PBE) exchange-correlation functional [43]. The projected augmented wave method [5] and a kinetic energy cutoff of 400 eV were used. Structural optimization was performed until the total energy and ionic forces were converged to 10^{-6} eV and 10 meV/Å, respectively. The amorphous Au_{55} structures were generated by simulated annealing using the classical embedded atom method potential [50]. Different annealing temperatures between 1200 K and 1670 K (bulk melting temperature of Au) were used and the thermally equilibrated structures were cooled down to 300 K before minimization at 0 K. Further optimization using DFT leads to total energies that vary within 1-2 eV among different amorphous structures and the lowest energy one was used as the target structure. The target structure of Au_{102} was taken as the Au_{102} core of the DFT-optimized $\text{Au}_{102}\text{MBA}_{44}$ cluster [33].

All systems were solved using a PES which consists of a linear combination of Rw , the repulsive and attractive thresholded spring potentials. The total potential energy in the Hamiltonian in Eq. (2.9) is expressed as:

$$U(q) = U_{Rw}(q) + U_{\text{spring}}(q, R_{\min}) + U_{\text{spring}}(q, R_{\max}) \quad (4.2)$$

The thresholded spring potentials are based on those previously proposed on by Petersen [44], i.e. $U_{\text{spring}}(q, r_t) = \frac{\kappa}{2} \sum_{i,j} (r_{i,j} - r_t)^2$ for all atomic distance $r_{i,j}$ outside the bounds of the spring threshold r_t . The resulting restoring forces on the out-of-bound

atoms bring the system back within the bounds of the PDF, R_{\min} and R_{\max} , and therefore preventing the system from exploding or collapsing. Otherwise, incorrect solutions may result by having atomic pair distances out of the PDF bounds. κ is the spring constant in eV/Å and the Rw potential is converted from unitless to eV via multiplication by a conversion factor λ .

Whereas the choice of the absolute values of λ and κ is somewhat arbitrary, their relative values are important in determining which term in Eq. (4.2) dominates the PES, especially when considering the effect of the simulation temperature. Generally, the ratio between the total potential energy and the temperature determines how much random motion will dominate the dynamics; a lower ratio implies that random motion will play a large role in the dynamics. The ratio between λ and κ of each spring describes how far the PDF can push the system below or above the bounds set by the spring potentials. Heuristically, too stiff a spring forbids the system to access new configurations, e.g. high energy “transition states” which may involve shorter bonds or a larger system size. Conversely, too small a spring constant makes it slower for the system to snap back within bounds and may lead to an explosion or implosion of the system, leaving the dynamics to drift aimlessly.

Model Parameters

Unless otherwise stated, the PDFs of the target and starting structures were generated using Eqn. (4.1) with a step of $\delta R = .01$ Å, $Q_{\min} = 0.1$ Å⁻¹, $Q_{\max} = 25.0$ Å⁻¹. R_{\min} and R_{\max} correspond to the first minimum before the first PDF peak and that after the last PDF peak, respectively, which ensure that the full meaningful region of the PDF is modeled. For each of the simulations, the Q resolution was calculated by

$$\delta Q = \frac{\pi}{R_{\max} + \frac{12\pi}{Q_{\max}}} \quad (4.3)$$

The HMC simulation was run with $N = 300$ iterations, a target acceptance rate of

0.65, and an average starting momentum for each NUTS iteration of 10 eVfs/Å. Both repulsive and attractive spring potentials are used with $\kappa = 200$ eV/Å and thresholds matching R_{\max} and R_{\min} of the PDF, respectively. $\lambda = 300$ eV was used as conversion factor for Rw . Each simulation was run with a pair of NVIDIA GTX970 graphics cards, with one card partially occupied with desktop visualization.

4.2 STRUCTURAL SOLUTIONS

Case I: crystalline Au₅₅

We first test our algorithm by solving the crystalline Au₅₅ (*c*-Au₅₅) cluster structure from its PDF. The starting structure is taken as the bulk-cut cuboctahedron of Au₅₅ with a uniform bond length of 2.89 Å. Due to finite-size and surface effects, the DFT-relaxed cluster structure shows a distinctively different bond length distribution as a function of the bond's distance to the cluster center of mass, and therefore is difficult to model with a small box approach which assumes an identical unit cell throughout the whole system.

R_{\min} and R_{\max} for this simulation were 2.45 Å and 11.4 Å, respectively, with $\delta Q = 0.24$ Å⁻¹. The simulation ran for approximately 34 minutes, over a total of ∼40 thousand configurations. The results are shown in Fig. 4.1.

The PDF, radial bond distribution, and bond angle distribution show good agreement between the target and final fitted structures, with a Rw of 0.3% whereas Rw of the starting structure is as high as 44.8%. DFT calculations yield a total energy of the final structure very close to that of the target structure (within a few meV). The success in the fitting is largely attributed to the factor that the target structure is only locally (and mildly) disturbed from its bulk-like counterpart and therefore there is no need to overcome any high PES barriers to reach the correct solution. As shown below, the situation is rather different for much more disordered target structures.

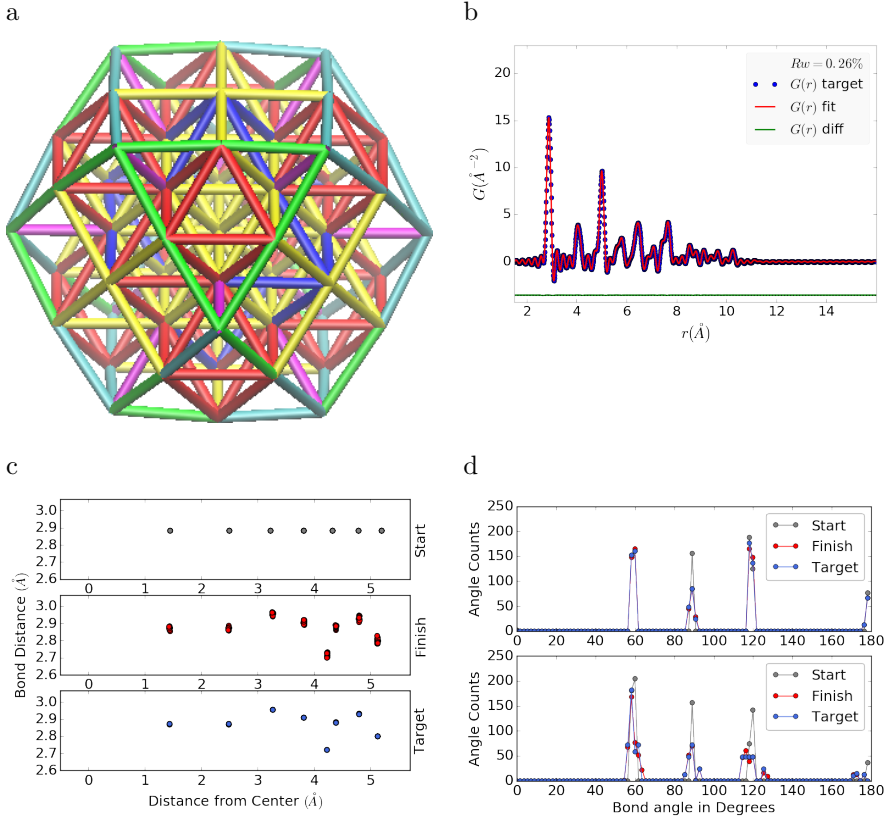


Figure 4.1: Au₅₅ PDF fitting of DFT-optimized c -Au₅₅. a) the final structural solution ($Rw=0.3\%$) with bond lengths color-coded by step of 0.05Å, b) the target PDF(blue dots) overlaid with the PDF of the final structure (solid red lines) with the difference in green lines offset below, c) the radial bond distribution, and d) bond angle distribution.

Interestingly, the small-box solution using PDFgui[17] yields a rather large Rw of 43%, due to the failure to fit the surface contracted atoms with a unit cell. The PDF fits of the starting structure and small-box solution are shown in Fig. S1 in the Supporting Information.

Case II: Au₅₅ with surface disorder

In addition to surface relaxation, the structure of a cluster or nanoparticle is often disrupted by the presence of defects and/or ligand bound to the surface. To mimic such surface disorders, we took the DFT-optimized c -Au₅₅ structure from case I as

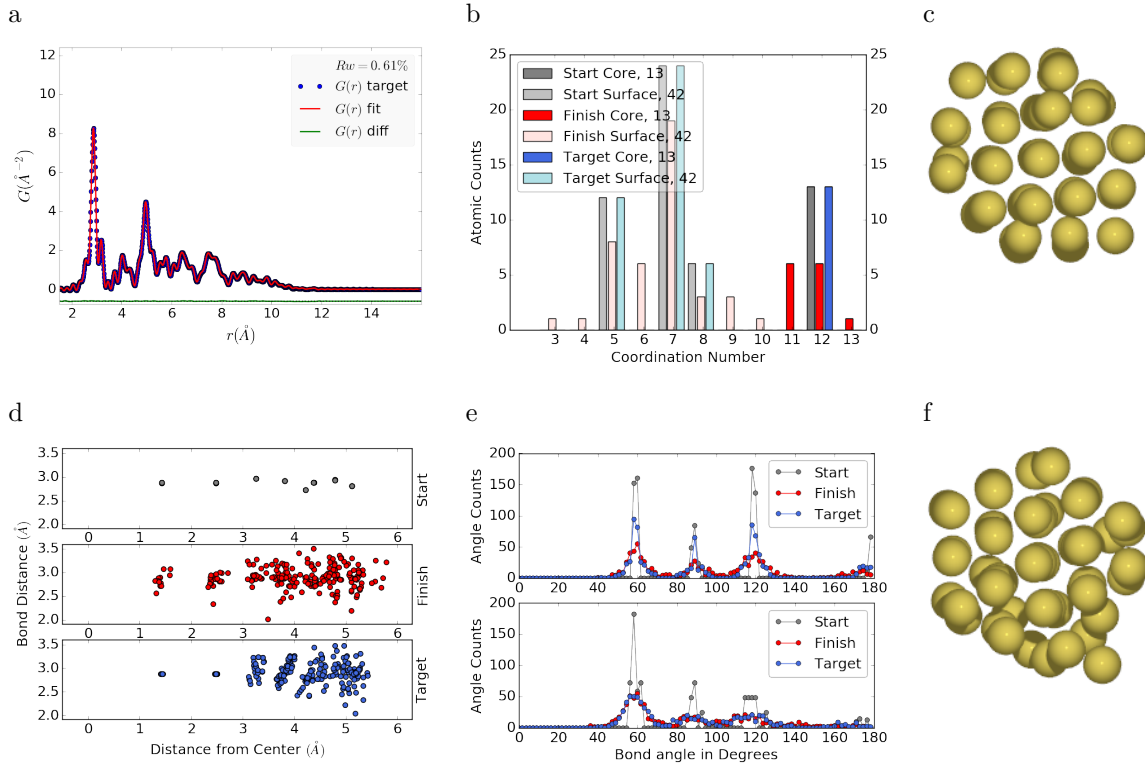


Figure 4.2: Au_{55} PDF fitting of surface-disordered Au_{55} . (a) the comparison of PDFs, (b) the CN distribution, (c) the target structure, (d) the radial bond distribution, (e) the bond angle distribution, and (f) the final structural solution ($Rw=0.6\%$)

the starting structure and randomly displaced the surface atoms with a normal distribution of $\sigma = 0.2 \text{ \AA}$. All atoms are allowed to move in the HMC simulation, including the originally undisturbed core, which is a Au_{13} cluster with O_h symmetry.

R_{\min} and R_{\max} for this simulation were 1.95 \AA and 12.18 \AA , respectively, with $\delta Q = 0.23 \text{ \AA}^{-1}$. The simulation ran for approximately 3.6 hours, over a total of ~ 270 thousand configurations. The results of the simulation are shown in Fig. 4.2.

Overall, good agreement is found between PDFs of the target structure and the final structural solution, even out to larger r , with an $Rw = 0.6\%$ starting from an $Rw = 50.4\%$ (see Fig. S2). The radial bond distribution and angle distribution show reasonably good agreement, but with lower degree of crystallinity in the final structure compared to the target structure. The discrepancy is most obvious in the core: despite the identical core structure in the starting and target structures,

the core atoms were displaced in the HMC simulations in order to achieve a “best” solution. This is because PDF measures the global average of interatomic distances between each atomic pair and does not contain direct information about the locality of such pairs, e.g. on the surface or cores. If such information is obtained a priori, for example, from theoretical prediction or other experimental measurements, the core structure can then be fixed and excluded from HMC dynamics.

Similar discrepancies are found in the CN distribution. Since the initial displacements of the surface atoms are relatively mild, the interatomic connectivities remain more or less the same and therefore the target structure has an identical CN distribution to the starting (unperturbed) structure. This is, however, not the case for the final fitted structure, which shows discernible differences, especially at the low and high CN numbers. This is partly caused by the displacement of the core atoms mentioned above, and partly by the lack of CN constraints for the PDF fitting, which has been previously demonstrated in the case of α -Si [10]. Additional experimental data, e.g. from EXAFS or NMR, may help to steer the simulations towards better agreement in both PDF and CN distribution.

Case III: amorphous Au₅₅

Next, we turn to the case in which the entire cluster structure is disordered. We used a DFT-optimized amorphous Au₅₅ (*a*-Au₅₅) as the target structure, and the DFT-relaxed *c*-Au₅₅ cluster from Case I as the starting structure. The total energy of *a*-Au₅₅ was computed to be *lower* than that of *c*-Au₅₅ by as large as 2.9 eV, consistent with the 3.0 eV found in previous DFT work [13].

R_{\min} and R_{\max} for this simulation were 2.6 Å and 11.26 Å, respectively, with $\delta Q = 0.25 \text{ \AA}^{-1}$. The simulation ran for approximately an hour, over a total of ~ 87 thousand configurations. The results of the simulation are shown in Fig. 4.3.

Our PDF fitting yielded a final structure of Rw of 1.7%, whereas that of the

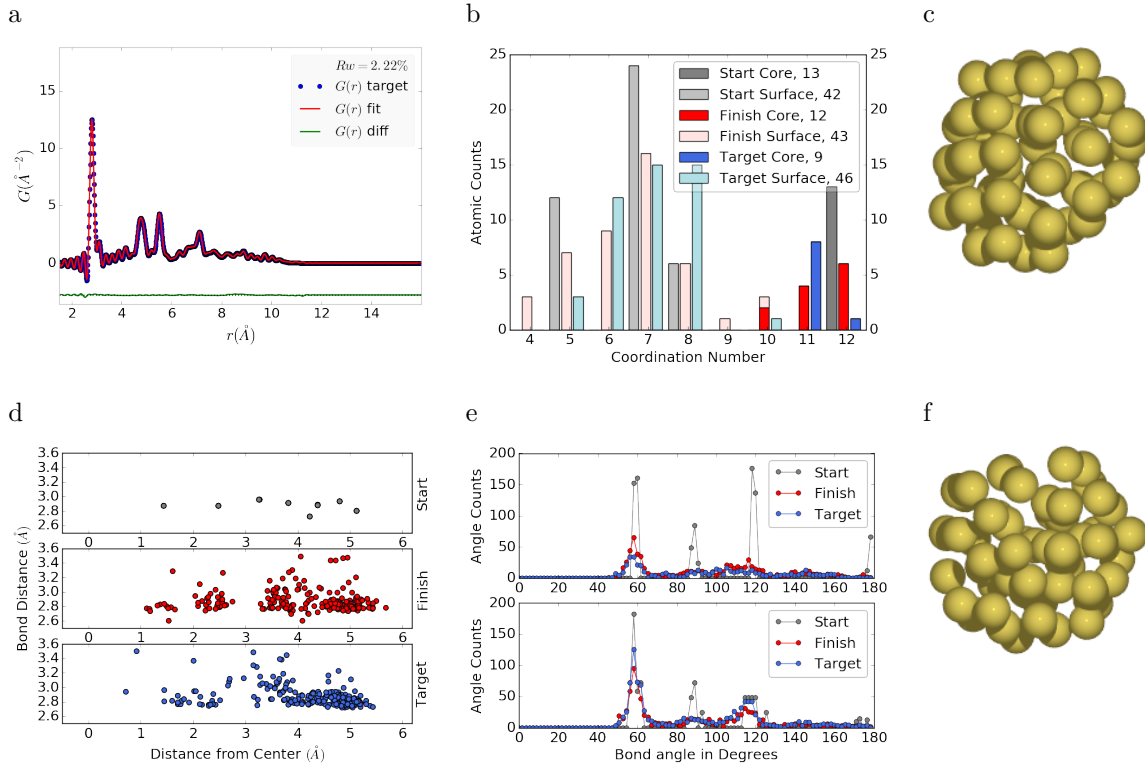


Figure 4.3: Similar to figure 4.2 for DFT-optimized amorphous Au_{55} .

initial structure is as high as 76.1% (see Fig. S3), due to the drastically different atomic structure of the crystalline and amorphous Au_{55} clusters. Overall reasonable agreement in PDF, bond angle distribution, and radial bond distance distribution was found, and the wide spread of the bond lengths was qualitatively reproduced. However, the mismatch in CNs is problematic, partly due to the lack of information and/or constraints on the CNs. The total energy of the final structure is computed to be ~ 6 eV higher than that of the target structure and the difference is substantially larger then the variation among different amorphous structures computed by DFT ($\Delta E_{\text{tot}} \sim \pm 1\text{-}2$ eV). Such a fitting result, despite the rather small Rw , clearly indicates the importance of complementary information and/or constraints necessary for reliably solving disordered NP structures from PDF.

Case IV: ligand-protected Au₁₀₂

Our final benchmark is Au₁₀₂, whose structure was initially solved by Jadzinsky and coworkers using x-ray crystallography [26] and further confirmed by DFT studies [33]. The Au₁₀₂ structure consists of three main parts, a 49-atom Marks decahedron core, two C_5 caps consisting of 20 atoms each, and 13 equatorial atoms. Unlike previous cases, the multi-symmetry nature of the structure, i.e. each part has its own distinct symmetry, poses a challenge for PDF-based solution of the structure. This is because of the atomically centralized nature of the PDF, in which each atom “sees” a density of other atoms surrounding it and has a strong tendency towards becoming the center of the main symmetry group. Such tendency may lead to a solution where some of the correct atomic symmetries are discarded in favor of the core symmetry.

Starting from fcc structure

The starting structure was generated by a spherical cut of the fcc bulk lattice, with two surface atoms removed to conserve the total number of Au atoms.

R_{\min} and R_{\max} for this simulation were 2.7 Å and 16. Å, respectively, with $\delta Q = 0.18 \text{ \AA}^{-1}$. The simulation ran for approximately two hours, over a total of ~ 82 thousand configurations. The results of the simulation are shown in Fig. 4.4.

The initial structure of an fcc bulk-cut cluster, had a starting Rw of 77.6% (see Fig. S4), whereas the final structure has a Rw as low as 8.1%. The disagreement between the final and target PDFs shows that the majority of the error is in the high R region, which is related to the long range distances between the core, caps, and equatorial atoms. The agreement for other structural metrics is less satisfactory. The bond angle distribution for core atoms in the final structure has a poor correlation with those in the target structure, with much broader peak widths. This is likely caused by the high kinetic barrier to change from one high-symmetry core structure (fcc) to another (Marks Decahedron). In contrast, the bond angle distribution for surface

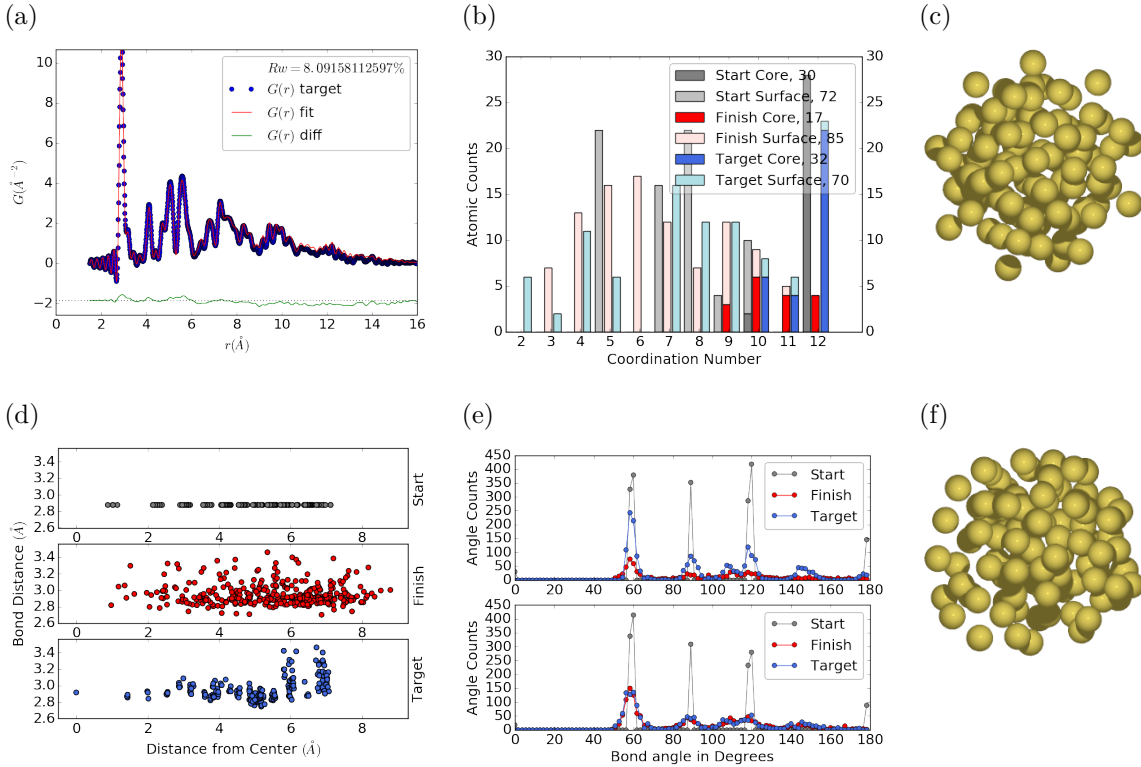


Figure 4.4: Similar to Fig. 4.2 for Au_{102} as in DFT-optimized $\text{Au}_{102}\text{MBA}_{44}$ cluster.

atoms, which are of lower symmetry than the core, show a much better agreement. This is due to the preference of Monte Carlo techniques for higher entropy, and thus lower symmetry, structures. Similarly, the radial bond distance does not show the correct clustering of bond lengths as expected from an ordered structure, indicating the amorphous nature of our fit. Finally, the CN distribution shows the largest discrepancy at $\text{CN}=12$, again due to the amorphous nature of the fit. Overall, the structural metrics beyond the PDF indicate the poor agreement between the final and target structures. A higher simulation temperature, potentially combined with CN or bond length aware potentials (such as DFT or EXAFS derived PESs) may help to resolve this discrepancy.

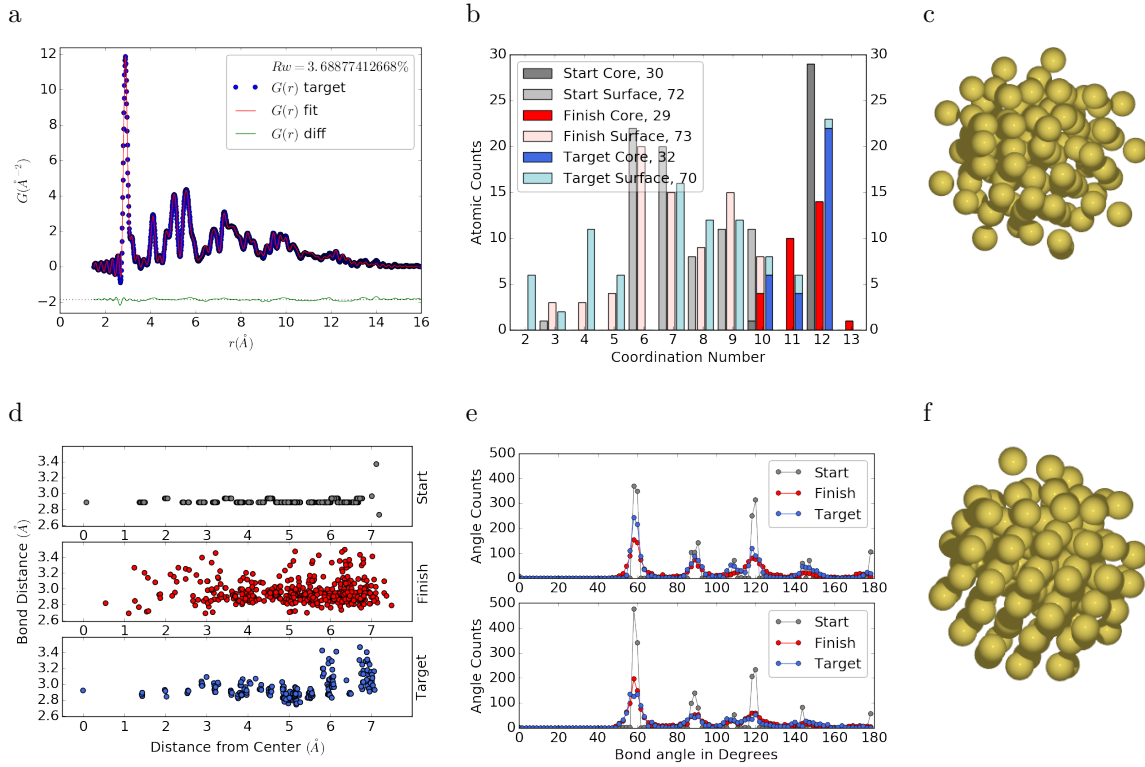


Figure 4.5: Similar to Fig. 4.4 with Marks decahedron as the starting structure.

Starting from Marks Decahedron

The starting structure, a Marks Decahedron, was generated by the ASE Cluster tool with 2 atoms on the [100] face normal to the 5-fold axis, 3 atoms on the [100] plane parallel to the 5-fold axis and, 1 atom deep Marks reentrance. This produced a structure with 101 atoms which was extended by one more Au atom to fill out the Au_{102} structure.

R bounds and Q resolution were the same as the previous case. The simulation ran for approximately 2.5 hours over a total of ~ 90 thousand configurations. The results of the simulation are shown in Fig. 4.5.

The starting structure of Marks decahedron ($R_w=56.6\%$, see Fig. S5) yielded a better structural solution, with a final R_w of 3.3%. However, the discrepancies at high R remains as in the previous case. By examining the final structure, we can see

that these high R errors are due to a lack of the two 20-atom caps and 13 equatorial atoms. Similarly, the radial bond distance distribution displays a diffusive behavior unlike the bond length clustering in the target structure. Compared to the previous case, the agreement in the CN and bond angle distributions are improved, with the latter capturing nearly all peaks in the target structure with the exception of the 110 bond angle. Relatively large discrepancies are found in the CN distribution at the low and high ends.

4.3 DISCUSSION AND CONCLUSION

The challenge of NP structure determination from X-ray Diffraction stems from the absence of long range atomic ordering and the presence of non-trivial disordered structures. PDF data analysis is one of the successful experimental methods for solving NP structures, which has been tested on varieties of NP structures using non-crystallographic large box hybrid methods [46]. In this work, we developed a novel, HMC-based method to solve the structures of NPs from PDFs. We chose monometallic Au clusters as benchmarks and generated synthetic experimental PDF data from DFT-optimized cluster structures. Two cluster sizes (Au_{55} and Au_{102}) and different degree of disorders (crystalline, surface disordered, amorphous, ligand-protected) were considered, which pose further challenges in addition to the lack of long-range order in finite-size systems.

The quality of the PDF fit, as measured by the agreement factor Rw , is expected to provide a basis for the comparison between the fit structure and the target structure. The HMC method is designed to find minima in the Rw PES and therefore the ultimate criterion for its success is the magnitude of the Rw values. This criterion has been met in the cases of surface relaxed $c\text{-Au}_{55}$, surface distorted-Au $_{55}$, and $a\text{-Au}_{55}$ systems, where we obtained an excellent fits with $Rw < 2\%$. With most of the modeling methods a PDF fit with an $Rw < 15\%$ would be considered a solved structure

[46, 1, 35, 51, 45]. However, a low Rw does not necessarily translate into the correct structural solution and the discrepancies may be caused by several different factors. For example, the disordered surfaces associated with NPs produces a fall off in the PDF profile, resulting in underestimated NP sizes in the fitted structures [46]. In addition, as the PDF profile depends on the average core and surface pair distributions, the structural solution may not be unique especially for disordered systems. This is best manifested in the example of amorphous Au_{55} , in which the final structure produces a rather small Rw but has distinctively different structural features and a much higher total energy compared to the target structure. In order to faithfully solve the structures, other fitting metrics, such as the atomic coordination numbers, may need to be considered. For ordered or partially ordered systems, we have demonstrated a reasonable agreement between the final and target CN distributions, whereas the discrepancy increases for disordered structures. A hybrid HMC method combining with other experimental (EXAFS, NMR) or computational (DFT, force field) methods is expected to provide more physical constraints, e.g. CN distribution, in the PDF fitting and result in better structural agreement.

The case of ligand-protected Au_{102} , a crystallographically well solved NP system by X-ray diffraction, provides a unique test for the HMC algorithm due to its multi-symmetry nature and very short range ordering. The structure of Au_{102} was solved using two different starting crystal structures, i.e. fcc and Mark decahedron. The Rw values support the Marks decahedron structure of the cluster core over the fcc one, but discrepancies are found at high R values. This could be explained as limitation of the method while using PDF profile fit for high symmetry local structures such as cap atoms in Au_{102} , which has a C_5 symmetry. This is an intrinsic problem with the PDF, which measures the global inter-atomic distances, thus causing each atom to see itself at the epicenter of the majority symmetry. Use of additional techniques, like EXAFS, which has an emphasis on the local coordination spheres, may help

with finding better minima by breaking the dominant symmetry and providing a low energy path to compartmentalized structures.

In summary, we present the development of a novel Hamiltonian Monte Carlo based method for finding atomic structure solutions to PDFs. We derived the analytical derivatives of Rw , $G(r)$, and $F(Q)$, which were used to guide the Hamiltonian dynamics to follow the gradient of the PES towards minimum energies. The matrix element algebra inherent to the Debye sum and its derivatives lent itself to be written as GPU kernels, allowing for the speedup of the HMC algorithm by massive parallelization. The GPU implementation is 100 to 4x faster than the comparable multi-core CPU enabled code, depending on the size of the NP. The robustness and accuracy of the HMC method was benchmarked against a set of Au cluster structures of different size and degree of disorder. Overall, low Rw values were obtained for all the benchmarks, with most of the structural features reproduced as shown by various structural metrics. The Au_{102} cluster, which contains both high symmetry local structures and disordered surface regions, posed the largest challenge. Although the fitted structure shows some dependence on two starting configurations, neither of them was able to fully solve the target structure. Future work which employs experimentally derived potentials, including EXAFS, or computational potentials that contain chemical bonding information, may help to solve these particularly difficult cases. Work is underway to extend this method to the grand canonical ensemble and parallel tempering, which will allow for solving structures with unknown number of atoms and compositions and provide better stochastic mixing of structures.

CHAPTER 5

X-RAY TOTAL SCATTERING DATA ACQUISITION AND PROCESSING

5.1 INTRODUCTION

X-ray total scattering experiments are generally performed at synchrotron light sources, as only these sources can provide the needed flux, energy, and high momentum transfer vectors needed to obtain reliable PDFs. [9, 16] Despite the need for a dedicated facility to perform the total scattering experiments, the experiments themselves are fairly forgiving, allowing for reactive gaseous environments, experiment temperatures ranging from 2 K to 1800 K, and even electrochemical cycling. [8, 47, 49] The rapid PDF data acquisition associated with 2D area detectors creates a data management problem, as 96 hours of beamtime could result in almost 10,000 images which need to be associated with the experimental conditions and detector metadata. [9] Finally, all this data needs to be processed by masking bad pixels and regions, integrating azimuthally, and converting the scattering data to the PDF. [30, 28, 54, 41, 3]

5.2 DETECTOR Q RESOLUTION

To properly azimuthally integrate the images taken from the detector the Q resolution of the pixels must be calculated. Azimuthal integration is the process of dividing the pixels up into “bins”. Each bin has a set width, usually in Q , which describes which pixels can go into the bin. During the integration process each pixel is placed into its corresponding bin. Finally a statistical measurement of the average of all the

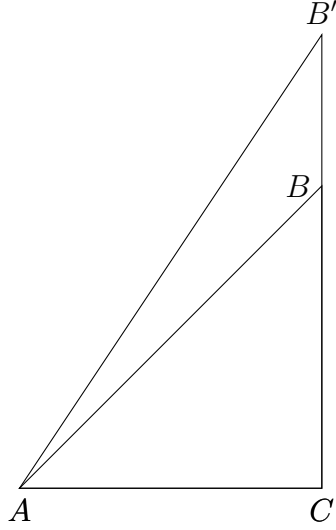


Figure 5.1: Scattering onto a flat detector

pixels in each bin is taken to produce the $I(Q)$ data. Although commonly performed, integrating using evenly spaced bins will cause pixels which are not on the same ring to be binned together, causing the incorrect value of $I(Q)$ to be obtained and a larger standard deviation in the integrated data. To properly calculate the Q resolution the resolution of each of the pixels in 2θ must be calculated. Figure 5.1 shows the scattering of x-rays onto a flat image plate detector. In this diagram the bottom of the n th pixel is B while the top is B' . The resolution of this pixel in 2θ is $\angle BAC - \angle B'AC$. Thus the resolution, calculated from the distances is

$$\Delta 2\theta = \arctan \frac{b}{d} - \arctan \frac{t}{d} \quad (5.1)$$

where d is the sample to detector distance (AC in figure 5.1), b is the distance to the bottom of a pixel (CB in figure 5.1)), and t is the distance to the top of that pixel (CB' in figure 5.1)). Note that these distances need to have been corrected for detector tilt and rotation. Thus the resolution of a pixel in Q is

$$\Delta Q = \frac{4\pi(\sin \arctan \frac{b}{d} - \sin \arctan \frac{t}{d})}{\lambda} \quad (5.2)$$

where λ is the x-ray wavelength.

This effect is analogous to looking at windows on a very tall building. The windows are all the same size, but due to the nature of the perspective, the windows seem to shrink as one looks higher up the building.

For a Perkin Elmer image plate, like the one used at the NSLS-II's XPD and the APS's 11-ID-B, the resolution function is shown in 5.2. For the same detector the number of pixels per Q is shown in 5.3

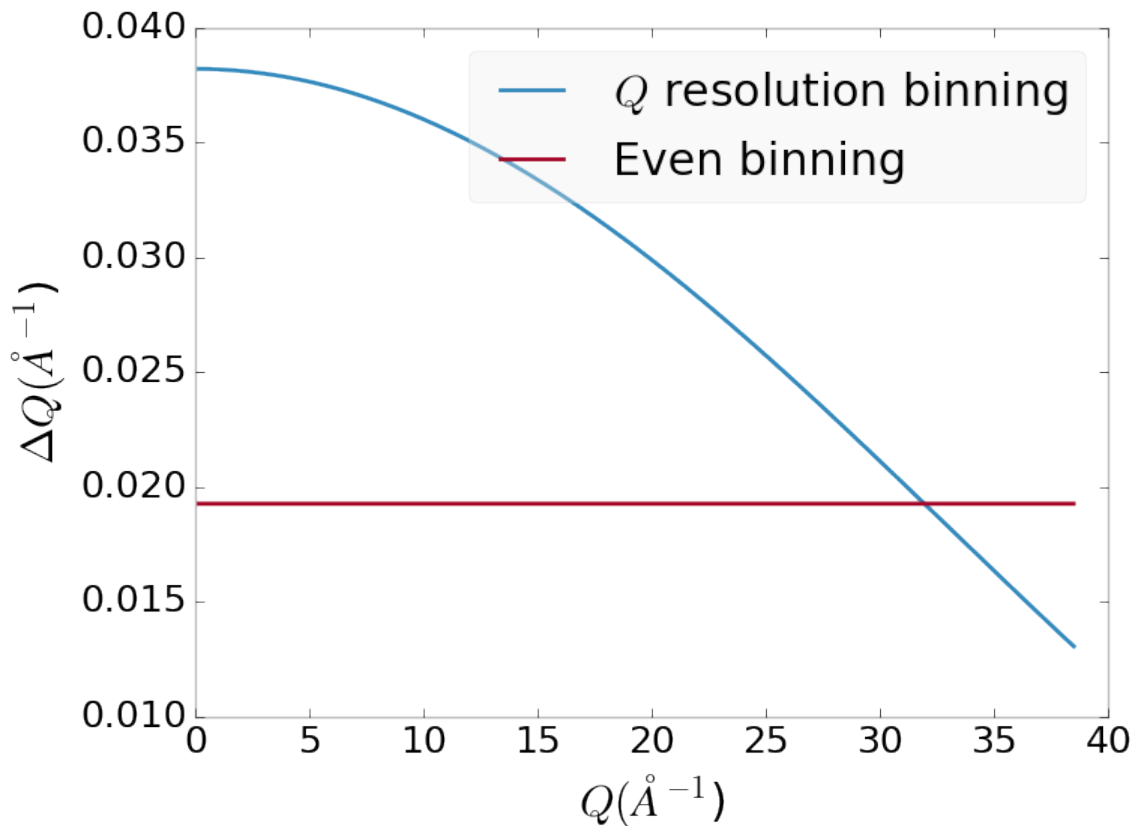


Figure 5.2: Q resolution as a function of Q .

5.3 AUTOMATED MASK GENERATION

Introduction

Detector masking is an important part of any x-ray scattering workflow as dead/hot pixels, streak errors, and beamstop associated features can be averaged into the data

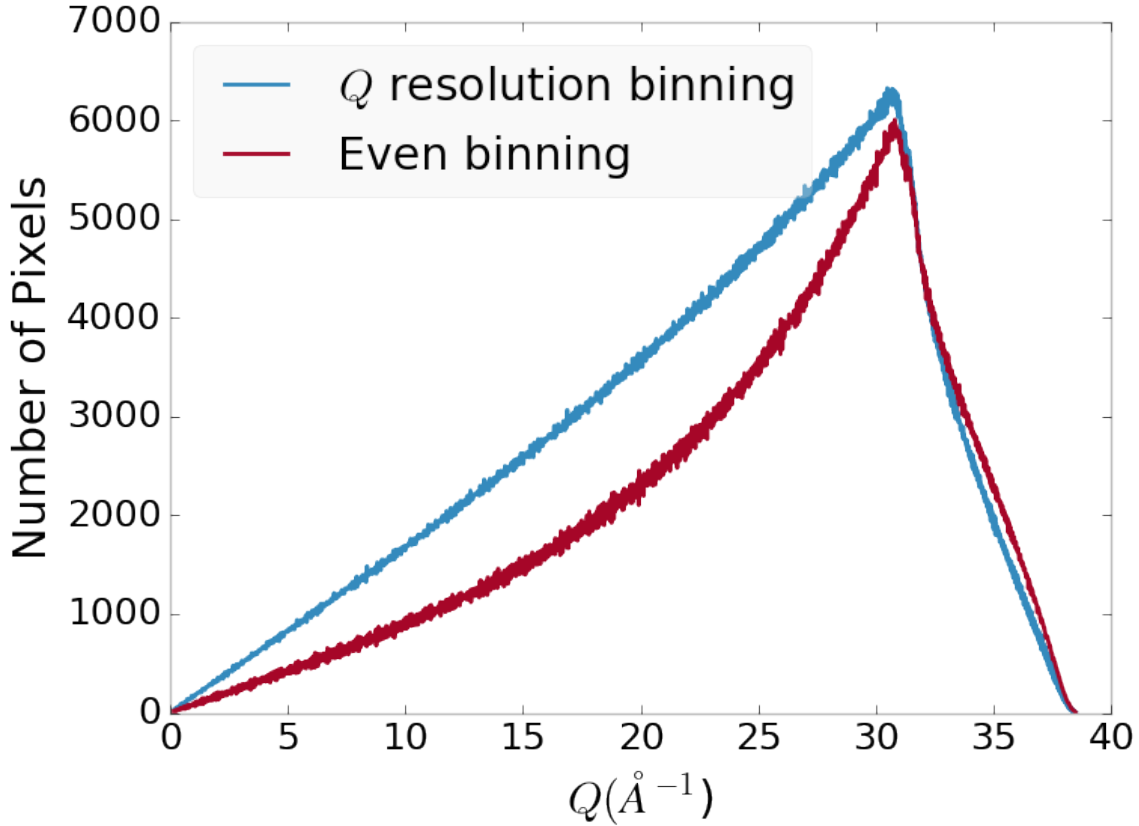


Figure 5.3: Number of pixels as a function of Q , binned at the Q resolution of the detector.

changing the signal and its statistical significance. While some features, like the beamstop holder, can be easily observed and masked by hand other are much more difficult to observe even on large computer monitors. Additionally, while dead/hot pixels and streaks are usually static the hot pixels associated with textured or single crystal scattering or cosmic rays are not. Thus, coming up with an automated method for finding such erroneous pixels is important, especially as high flux diffraction beamlines can generate data very quickly.

While this problem can be quite complex in the most general case, we can use the annular symmetry of the powder scattering pattern to our advantage, by comparing a pixel against pixels in the same ring. Since non-textured powder scattering should produce the same pixel intensity for a given ring we can mask any pixels which are α

standard deviations away from the mean. This method relies on the aforementioned pixel binning algorithm, as using miss sized bins will cause some pixels which should be in separate rings to be put together, and others which should be in the same ring to be separated. In that case the masking algorithm will overestimate the number of pixels to be masked due to the additional statistical variation in the sample.

Algorithm Design

The masking algorithm procedure takes in the image and a description of the pixel positions in either distance from the point of incidence or in Q . The image is then integrated twice, producing both the mean $I(Q)$ and the standard deviation of each $I(Q)$ ring. The mask is created by comparing the pixel values against each ring's standard deviation and threshold α . Note that the threshold can be a function of distance from the point of incidence or Q .

Test Cases

To study the effectiveness of the masking we ran the algorithm against both simulated and experimental data. In the case of the simulated data four systems were created: 1) dead/hot pixels with varying numbers of defective pixels, 2) beamstop holder with varying beamstop holder transmittance, 3) rotated beamstop holder with varying beamstop holder transmittance, and 4) beamstop holder with dead/hot pixels. The base scattering was produced by

$$I = 100 \cos(50r)^2 + 150 \quad (5.3)$$

where r is a pixel's distance from the beam point of incidence. The positions of the dead/hot pixels were chosen at random as was the dead or hot nature of the defect. Dead pixels had values from 0 to 10, while hot pixels had values from 200 to 255. The beamstop was positioned at the vertical center of the detector with an

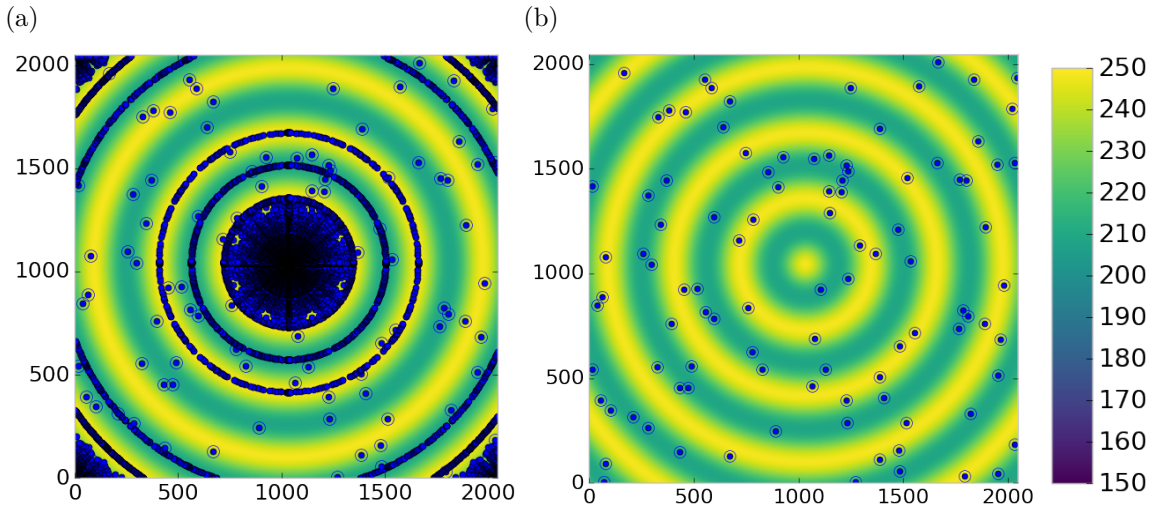


Figure 5.4: Generated dead/hot pixel masks for a detector with 100 bad pixels. a) the standard even bin mask and b) the Q resolution binned mask. The bad pixels are noted with open circles, masked pixels are noted with solid circles.

initial width of 60 pixels and final width of 120 pixels. The height of the beamstop was 1024 pixels. The beamstop was calculated to attenuate the x-ray scattering signal at various transmittance, as various beamstop holder materials have different transmittance. Two version of the masking algorithm were run for each test case, one using the standard even bin sizes for the integration step, and one where the bin sizes are tuned to the pixel Q resolution as discussed in 5.2.

Results and Discussion

Three main studies were run each examining a different aspect of the simulated or experimental studies. These included, masking bad pixels, masking a beamstop holder, and masking experimental data. Figures 5.4-5.11 show the results of the masking algorithm on simulated images. The dead/hot pixel masking shows the importance of using the Q resolution based bin sizes as the even bin based mask have a tendency to over mask the image, removing pixels which contain valuable signal. This over-masking is caused by pixels being improperly associated with one another by the

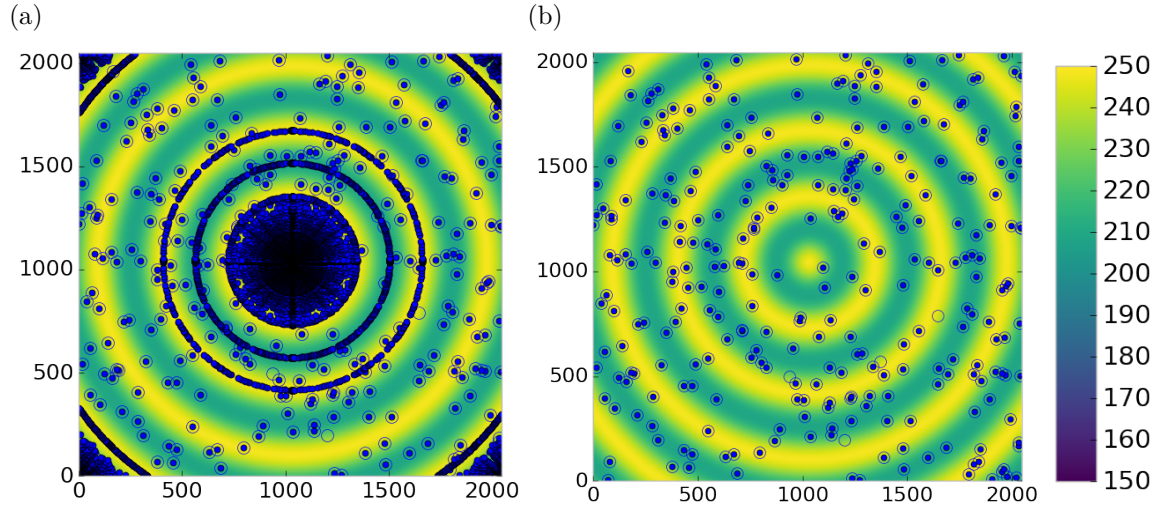


Figure 5.5: Generated dead/hot pixel masks for a detector with 300 bad pixels. a) the standard even bin mask and b) the Q resolution binned mask. The bad pixels are noted with open circles, masked pixels are noted with solid circles.

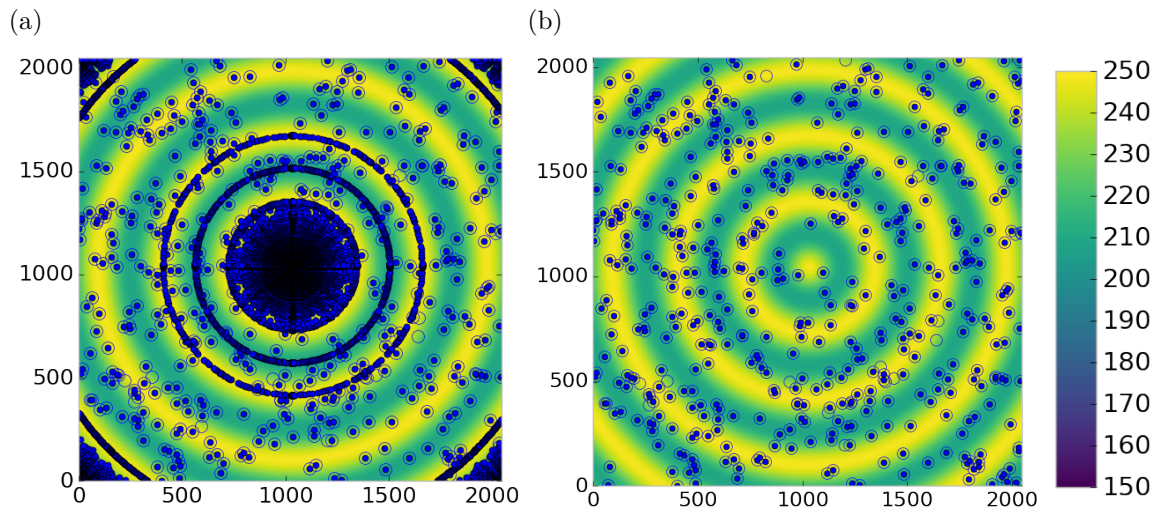


Figure 5.6: Generated dead/hot pixel masks for a detector with 500 bad pixels. a) the standard even bin mask and b) the Q resolution binned mask. The bad pixels are noted with open circles, masked pixels are noted with solid circles.

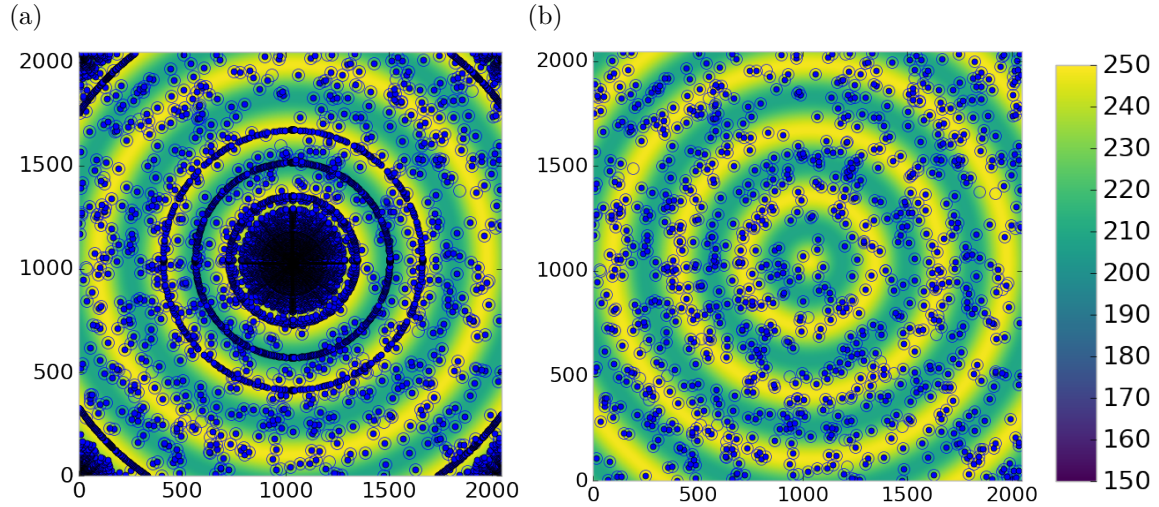


Figure 5.7: Generated dead/hot pixel masks for a detector with 1000 bad pixels. a) the standard even bin mask and b) the Q resolution binned mask. The bad pixels are noted with open circles, masked pixels are noted with solid circles.

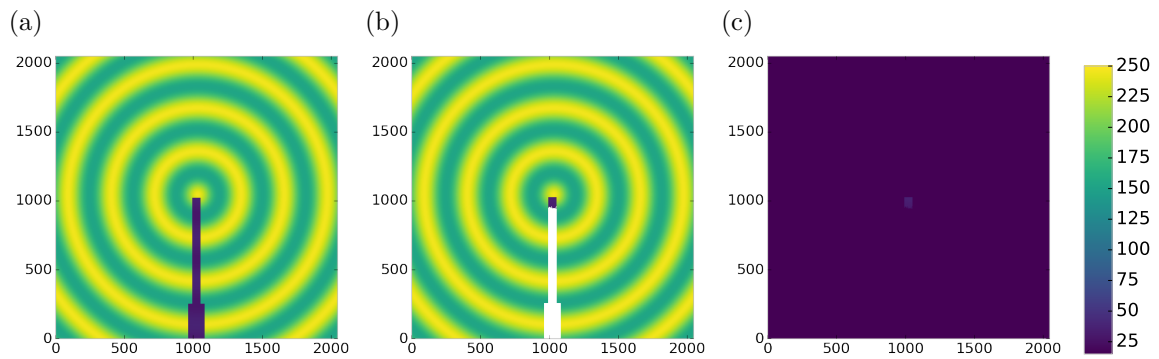


Figure 5.8: Generated beamstop holder masks for a beamstop holder with 10% transmittance. a) the raw image, b) the masked image, c) and the missed pixels. Note that the masked pixels in b) are white.

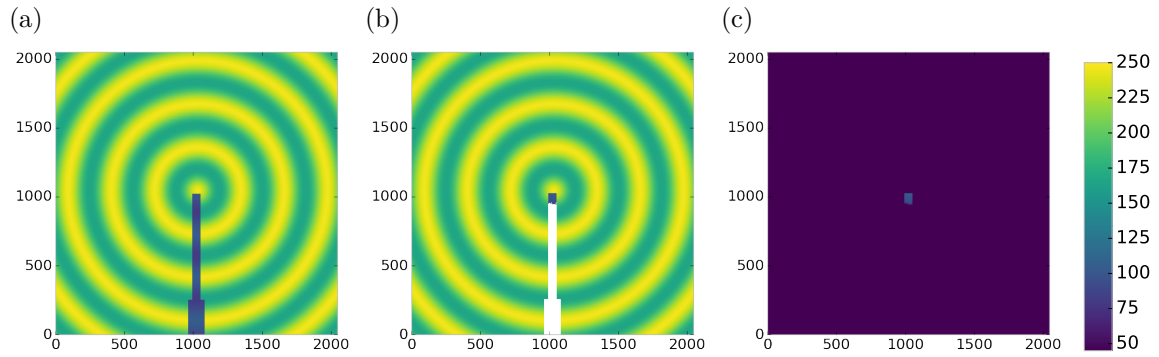


Figure 5.9: Generated beamstop holder masks for a beamstop holder with 30% transmittance. a) the raw image, b) the masked image, c) and the missed pixels. Note that the masked pixels in b) are white.

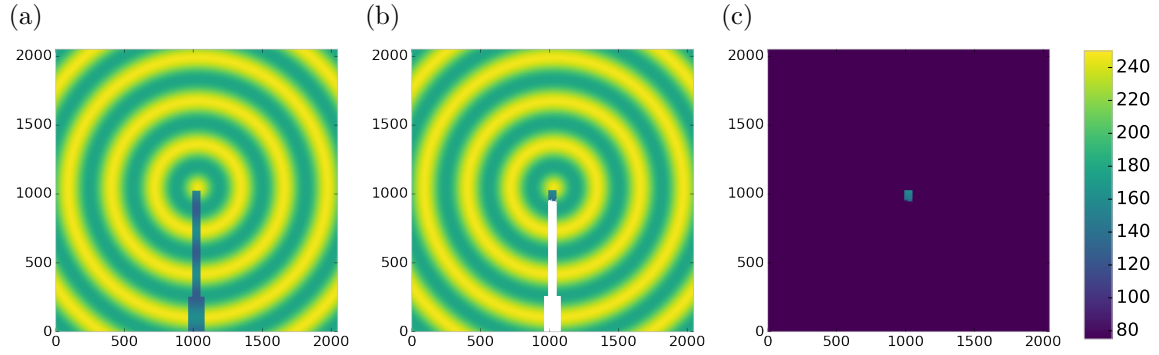


Figure 5.10: Generated beamstop holder masks for a beamstop holder with 50% transmittance. a) the raw image, b) the masked image, c) and the missed pixels. Note that the masked pixels in b) are white.

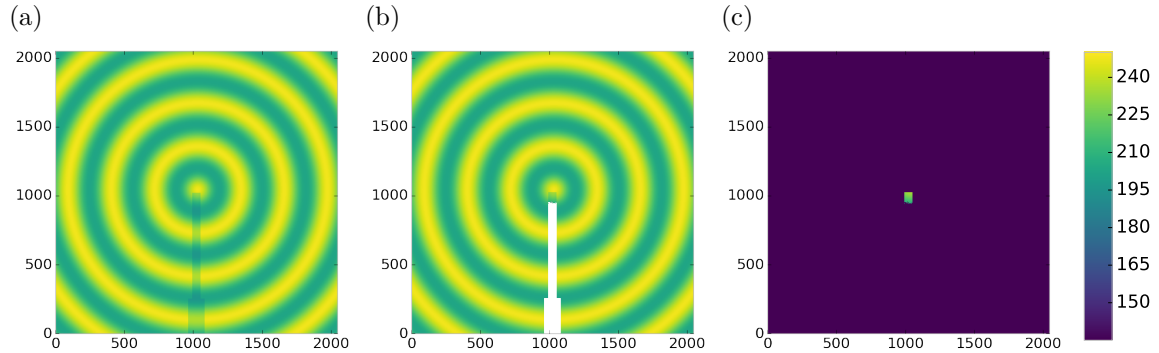


Figure 5.11: Generated beamstop holder masks for a beamstop holder with 90% transmittance. a) the raw image, b) the masked image, c) and the missed pixels. Note that the masked pixels in b) are white.

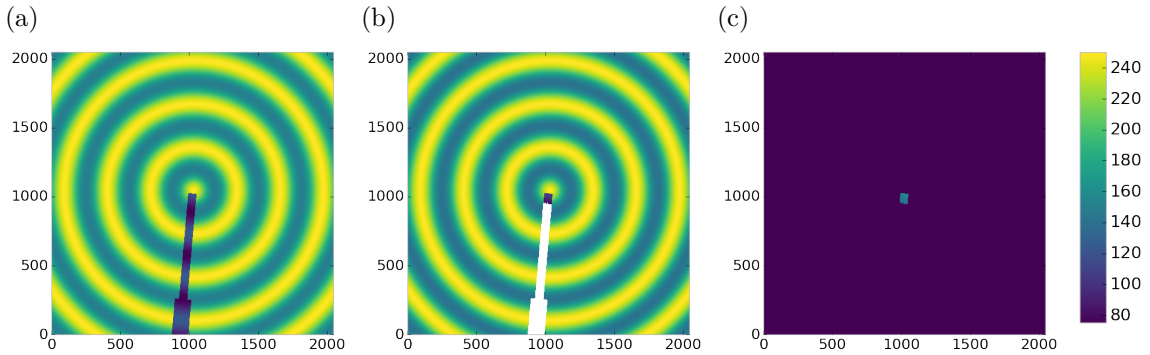


Figure 5.12: Generated beamstop holder masks which is rotated away from vertical. Note that the masked pixels in b) are white.

even bins. Figure 5.4 indicates that the masking algorithm, with the proper binning, masks the image perfectly, with no missed bad pixels or good pixels masked. This is not the case in figures 5.5 - 5.7 as we can see pixels which should have been masked but were not. Despite these missed pixels no pixels were improperly masked in any of the well binned images. These test cases are actually more difficult than experimental data, as the dynamic range of most detector causes the dead/hot pixels and single crystal/texture peaks to be orders of magnitude away from the desired signal.

The beamstop holder masks shown in figures 5.8 - 5.11, which were all run with the Q resolution binning show similar results across the transmittance range, missing only a small part of the beamstop holder near the point of incidence. Near this point the beamstop holder becomes a statistically significant part of the total number of pixels in a given ring, thus it can not be masked out using a statistical search of the rings. For most PDF and XRD studies this small area can be masked automatically by masking all the pixels who's distance from the point of incidence is smaller than a given radius r , or can be neglected outright as the area is not used in the analysis or refinement. Similar results were produced for beamstop holders which were rotated away from the vertical position, as shown in figure 5.12

Working with actual experimental data, obtained at the Advanced Photon Source beamline 11-ID-B, shows the difficulty of masking images which have low photon

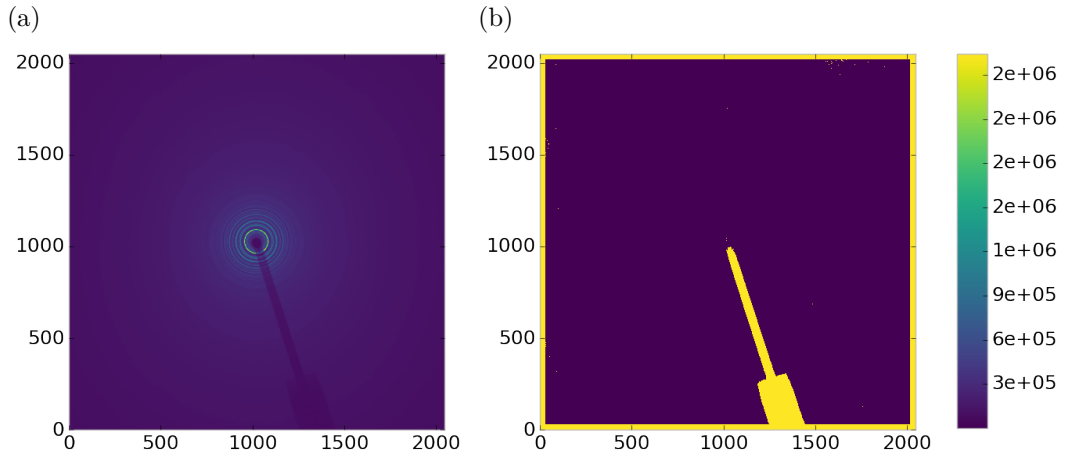


Figure 5.13: Masked experimental data. a) the raw image, b) the mask.

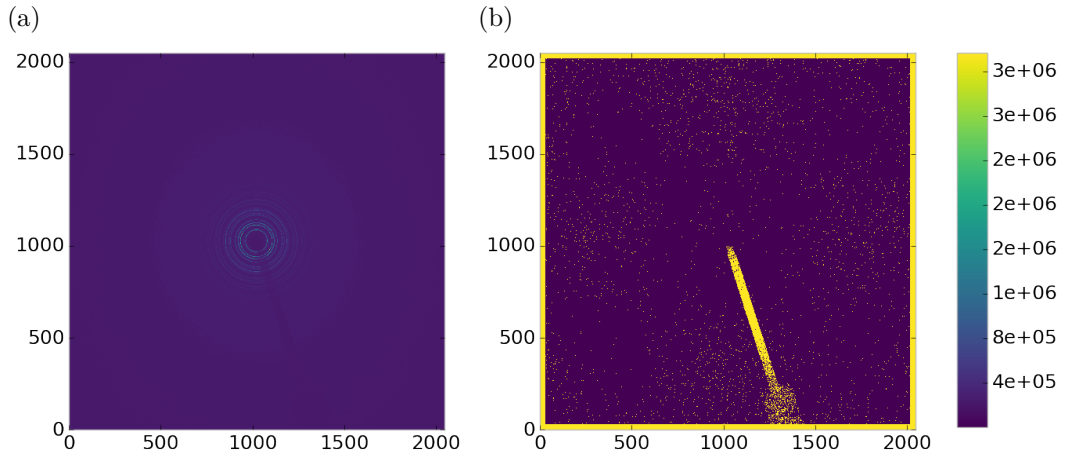


Figure 5.14: Masked experimental data with Pt single crystal signal. a) the raw image, b) the mask.

counts. While the masking of experimental data taken with longer exposures, consisting of 250 .2 second shots, shown in figure 5.13 provides very sharp edges to the beamstop holder, and very little extra masking beyond the occasional dead pixel, this is not the case for the single crystal data. The single crystal data is more problematic because of its short exposure time and low flux, with 500 frame at a .1 second exposure and having shrunk the beam size. The low flux is to prevent the very strong single crystal peaks from damaging the detector. However, this causes the image to be less statistically viable then ideal, causing problems with the mask as seen in

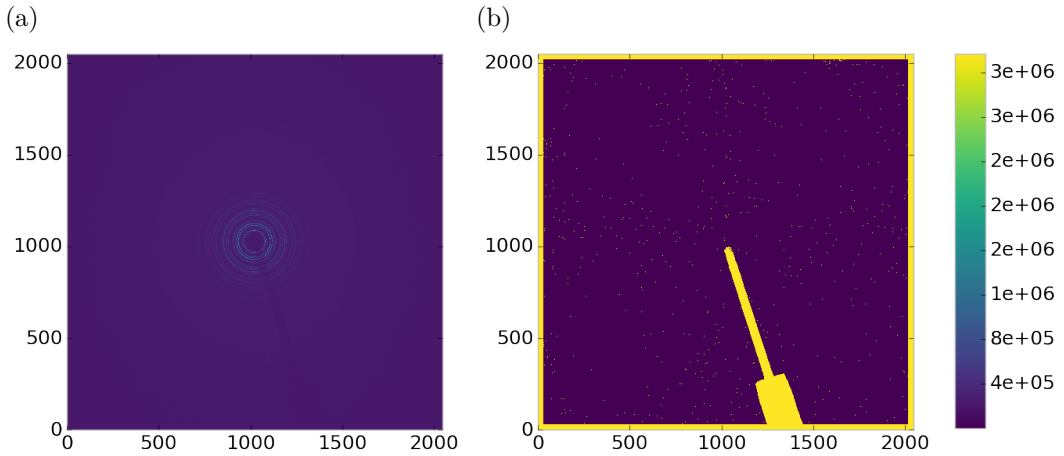


Figure 5.15: Masked experimental data with Pt single crystal signal using figure's 5.13 mask as a starting mask. a) the raw image, b) the mask.

figure 5.14. This can be alleviated to some degree by using the previously generated mask as a starting mask for the single crystal image, as shown in 5.15. While the masking algorithm still produces many diffuse masked pixels, they are far fewer, this may be due to the removal of the beamstop which could have contributed to the large standard deviation in figure 5.14.

Conclusions

In this section the masking algorithm, which relies on both Q resolution based binning and a statistical approach to azimuthal symmetry, was developed. The focus of this algorithm was to remove many unwanted detector features associated with pixel defect, beamstop holder associated scattering attenuation, and single crystal/texture peaks. Simulated data was used to evaluate the beamstop holder and dead/hot pixel masking capacity, while experimental data was used to check for single crystal and texture based masking. Q resolution based binning was shown to be very important to avoid over-masking. The ability of the mask writer to mask images is somewhat limited by the overall statistical image quality, although some deficiencies can be obtained by using previously generated masks as starting points. This masking algo-

rithm is now in use in the data processing workflow and will be available in scikit-beam soon.

5.4 AUTOMATED IMAGE AZIMUTHAL INTEGRATION

Using the Q resolution binning and masking developed in sections 5.2 and 5.3 the images can be properly integrated. Generally, images are integrated by taking the mean value of the pixels in a ring. However, other statistical measures of the average value can be used, like the median. Note that all the integrations done here use the pixels as they are, without pixel splitting, minimizing the covariance of the resulting $I(Q)$.[54]

Figures 5.16-5.18 show the importance of masking and the choice of average function. All the figures were produced using the same dataset, 50 °C Pr_2NiO_4 taken at the APS’s 11-ID-B on a Perkin Elmer area detector. The automatic masking alpha was 3 standard deviations from the mean. While it is difficult to observe the changes the mask causes in the full $I(Q)$ plot (subfigures a) and b)), the standard deviation plots show the effect of bad pixels on the data (subfigure c)). Subfigure c) for figures 5.16-5.18 shows that removal of the beamstop holder lowers the low Q standard deviation from around .1 to almost .01 out to 15 \AA^{-1} . The high Q subfigures d) and f) in figures 5.16-5.18 show the “kink” effect of the detector edge and beamstop holder, where there is a dip in the $I(Q)$ scattering when the rings include the edge of the detector. This effect seems to be due to both errors in the edge pixel intensity and the beamstop holder as masking of the edges only seems to provide only partial removal of the issue. It is important to note that while integration using the mean of the ring has issues with only the edge mask, as evidenced by the change in slope in 5.17 d) around 29.5 \AA^{-1} , the median integration does not include this error. Ideally the detector would have a normal distribution of pixel intensity for a given ring, which would imply an equivalency between the mean and median $I(Q)$ values. Despite the

closeness of the mean and median once the final mask has been created, it seems that the median is more reliable, as it was less effected by the beamstop holder in figure 5.17. Thus, for subsequent integrations discussed in this work the median is used to avoid any defective features that the masking algorithm may have missed.

5.5 CONCLUSIONS

This chapter developed and analyzed the proper data processing and reduction methodology for producing reliable $F(Q)$ data from x-ray total scattering measurements. Binning at the Q resolution of the detector was found to be key to the data processing. The primary outcome of using the Q resolution binning was an enhancement in effectiveness for the masking algorithm, producing much fewer false positives for dead/hot pixels. This masking approach was then applied to the integration of experimental data taken at the APD’s 11-ID-B beamline. The automatically generated masks, when combined with edge masks, were found to greatly reduce the overall standard deviation of the pixel intensity and produce a smoother $F(Q)$ at high Q , enabling the use of much higher Q data in the PDF. Different statistical measures used in the azimuthal integration was also compared. This comparison showed that the median was a more reliable statistic for integration with data which had more detector defects. However, upon properly masking it was shown that these metrics were almost identical. The masking induced similarity between the mean and median shows that the rings, when integrated, may form a Gaussian distribution. The distribution of the pixel intensities for strongly and weakly scattering samples may be investigated in future work.

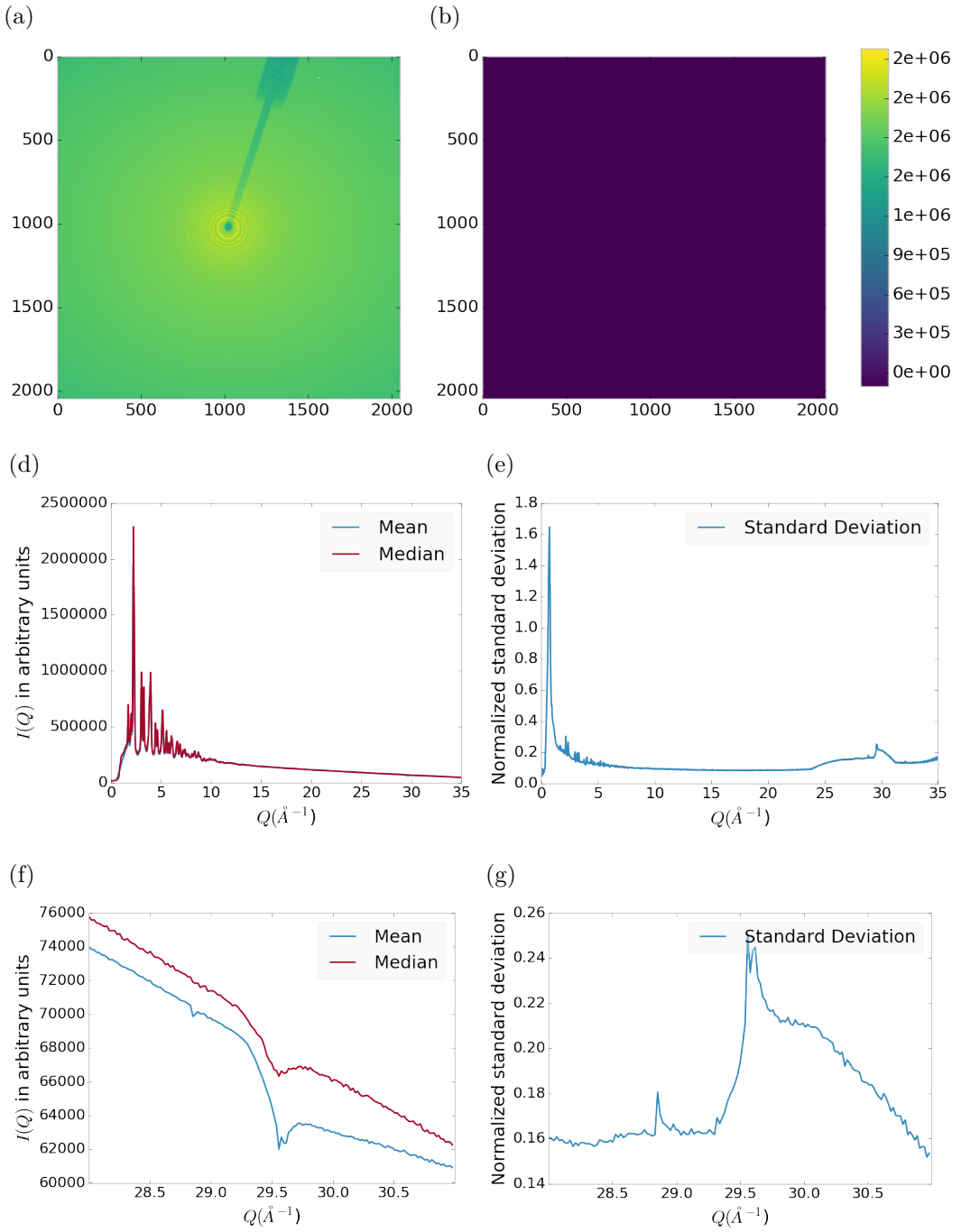


Figure 5.16: Masking, average, and standard deviation of an example x-ray total scattering measurement. This image was produced with no mask. a) the image, b) the mask, c) the mean and median values, d) the standard deviation (normalized to the median), e) a closeup of the 28\AA^{-1} to 31\AA^{-1} Q range for the mean and median, f) 28\AA^{-1} to 31\AA^{-1} Q range for the standard deviation

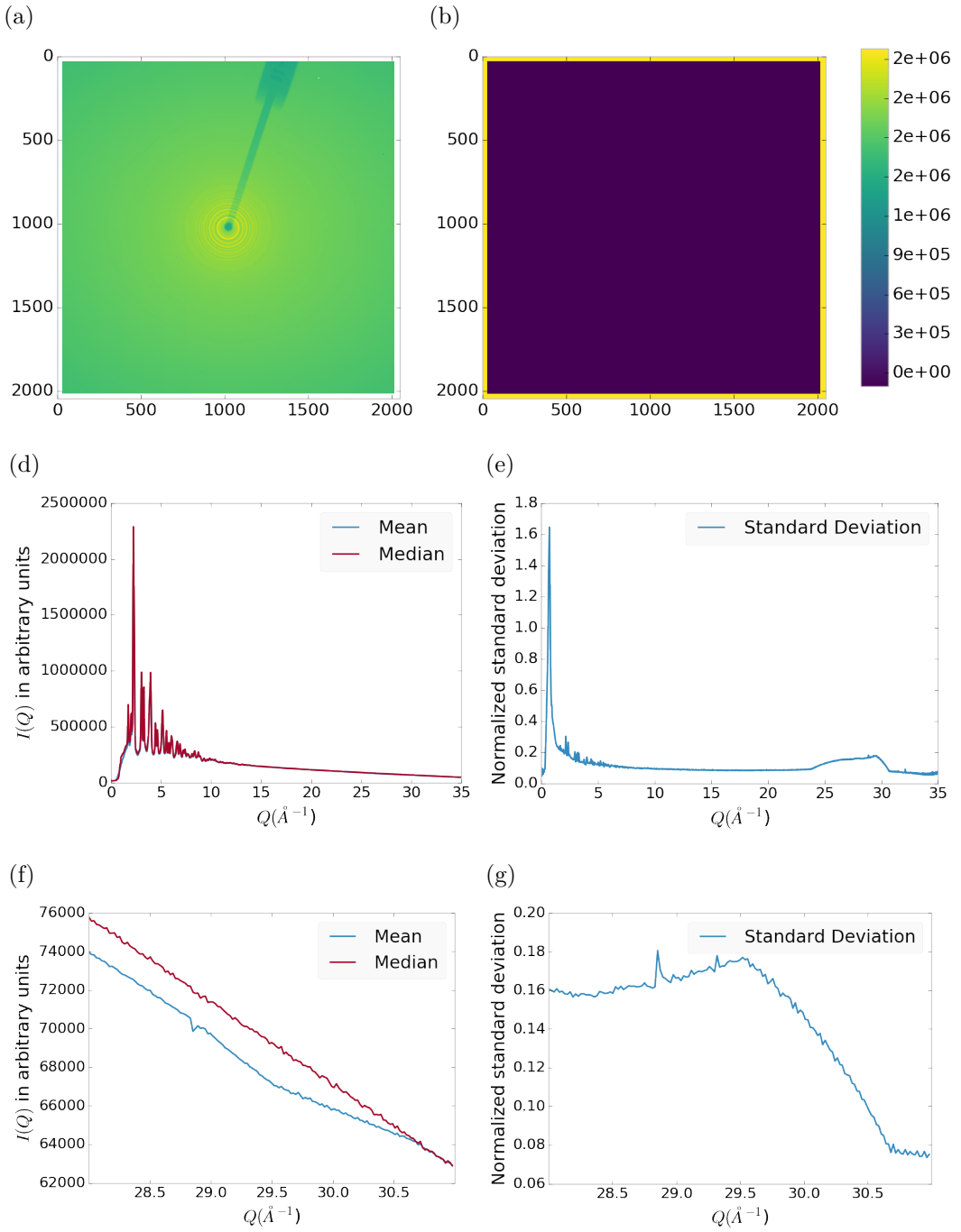


Figure 5.17: Masking, average, and standard deviation of an example x-ray total scattering measurement. This image was produced with only an edge mask. a) the image, b) the mask, c) the mean and median values, d) the standard deviation (normalized to the median), e) a closeup of the 28\AA^{-1} to 31\AA^{-1} Q range for the mean and median, f) 28\AA^{-1} to 31\AA^{-1} Q range for the standard deviation

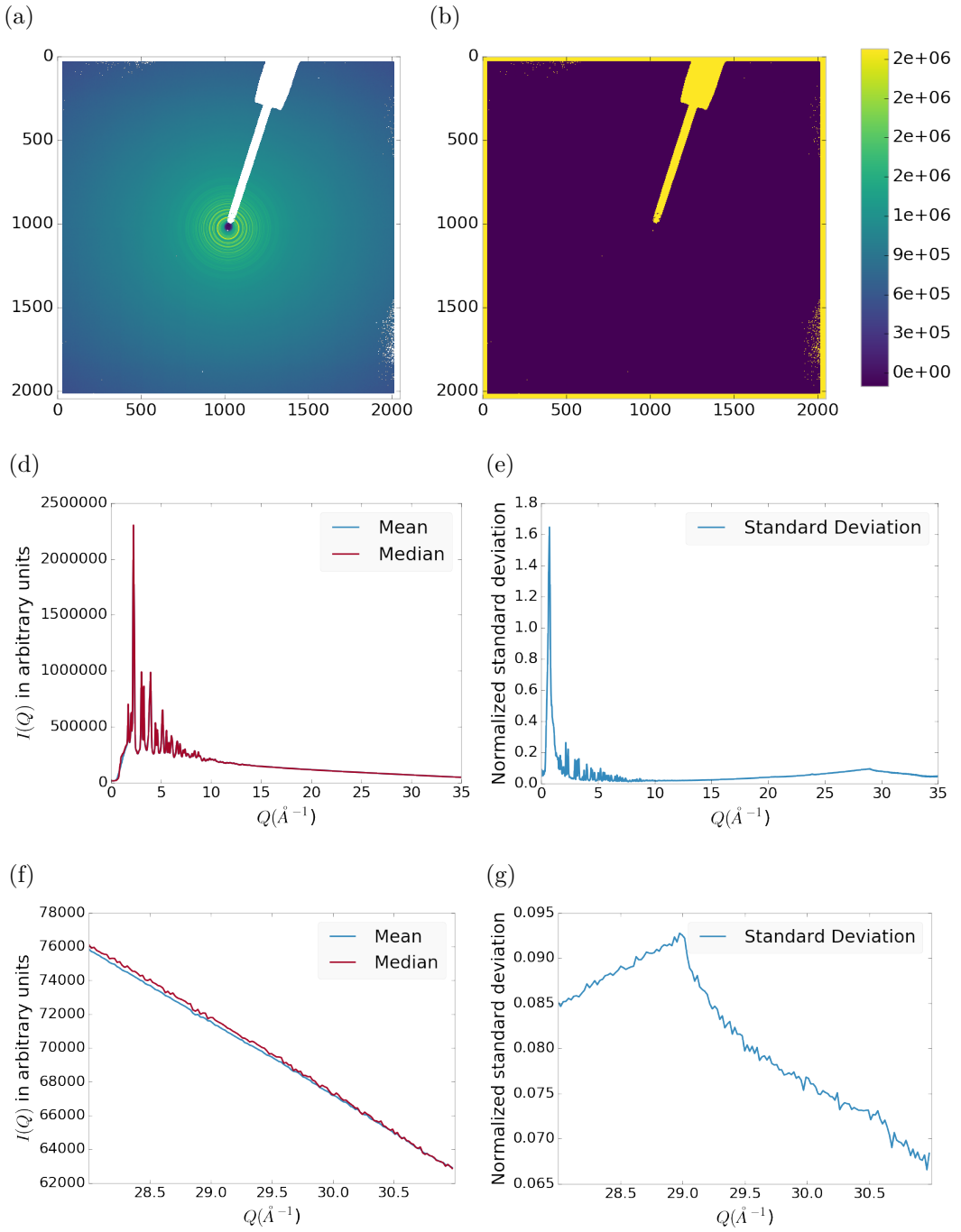


Figure 5.18: Masking, average, and standard deviation of an example x-ray total scattering measurement. This image was produced combining an edge mask and the automatically generated mask. a) the image, b) the mask, c) the mean and median values, d) the standard deviation (normalized to the median), e) a closeup of the 28 \AA^{-1} to 31 \AA^{-1} Q range for the mean and median, f) 28 \AA^{-1} to 31 \AA^{-1} Q range for the standard deviation

CHAPTER 6

PHASE CHANGES AND ANNEALING DYNAMICS OF Pr_2NiO_4 AND ITS DERIVATIVES

6.1 INTRODUCTION

Pr_2NiO_4 (PNO) electrodes provide higher power density than $\text{La}_{0.8}\text{Sr}_{0.2}\text{MnO}_3$ (LSM), and is more stable than $(\text{La}_{0.60}\text{Sr}_{0.40})_{0.95}(\text{Co}_{0.20}\text{Fe}_{.80})\text{O}_{3-\text{x}}$ (LSCF), which is known to rapidly degrade in performance. [57] PNO's high performance between 600-900 °C is associated with its high activity towards the oxygen reduction reaction (ORR), which stems from PNO's high oxygen diffusion and surface exchange coefficients, substantial oxygen over-stoichiometry, and large oxygen ion conduction paths through the unit cell. [55] Despite these advantages, PNO's tendency to partially decompose into PrO_x and other phases is particularly challenging. [14] Full cell operation after 500 hours at 750 °C and 0.8 V shows major decomposition of the parent PNO phase, while the performance degrades by only 4%. Such significant changes in phase and relatively small changes in performance further assure the necessity for understanding the phase evolution in nickelate cathodes during operation. To address these disparity in performance and phase degradation PDF and XRD analysis may be able to examine these issues from both long and short range ordering perspectives.

6.2 EXPERIMENTS

Pr₂NiO₄ Synthesis

Pr₂NiO₄ was synthesized using the standard approach, as detailed in the work by Dogdibegovic et al. [14] The nickelate powder was initially prepared via the glycine-nitrate process. This was followed by thermal annealing at 1080 °C for 10 hours in air.

X-ray Measurements

X-ray total scattering and x-ray powder diffraction experiments were performed at the APS's 11-ID-B beamline. An x-ray energy of 86.7 keV, .145 Å was provided by the beamline monochromator. The detector was moved between a 20cm and a 95 cm sample to detector distance to measure the x-ray total scattering and x-ray diffraction patterns. Various PNO samples were annealed on the beamline during x-ray measurement.

6.3 DATA PROCESSING

The data was calibrated at each of the detector positions using a CeO₂ standard via pyFAI. [30] The images were corrected for a .95 x-ray polarization. Masks were produced for both the foreground and background images. The foreground masks were produced using both a 30 pixel edge mask and a 2.5σ automatic mask as discussed in chapter 5. The background masks were produced by using the foreground mask as a starting mask with a 2.5σ automatic mask.

The foreground and background images were then integrated using the Q resolution binning discussed in chapter 5. The resulting $I(Q)$ data were corrected for their number of frames and I_{00} . Finally the corrected background $I(Q)$ was subtracted from the foreground $I(Q)$.

Each PDF was generated with a Q_{min} of 1.5, Q_{max} of 29., R_{poly} of .9, R_{max} of 40. Descriptions of these parameters can be found in the work by Juhas et. al. [28]

6.4 DATA ANALYSIS

Intra Sample Comparison

PDF

As figures 6.1 and 6.2 show the as synthesized PNO undergoes very little change in structure according to the PDF. The PDF does show some broadening at around 3.5 and 8.5 Å, but the peak shifts themselves are fairly limited. This implies that the as synthesized PNO structure is stable at least for the 1 hour that the sample was held at 750 °C.

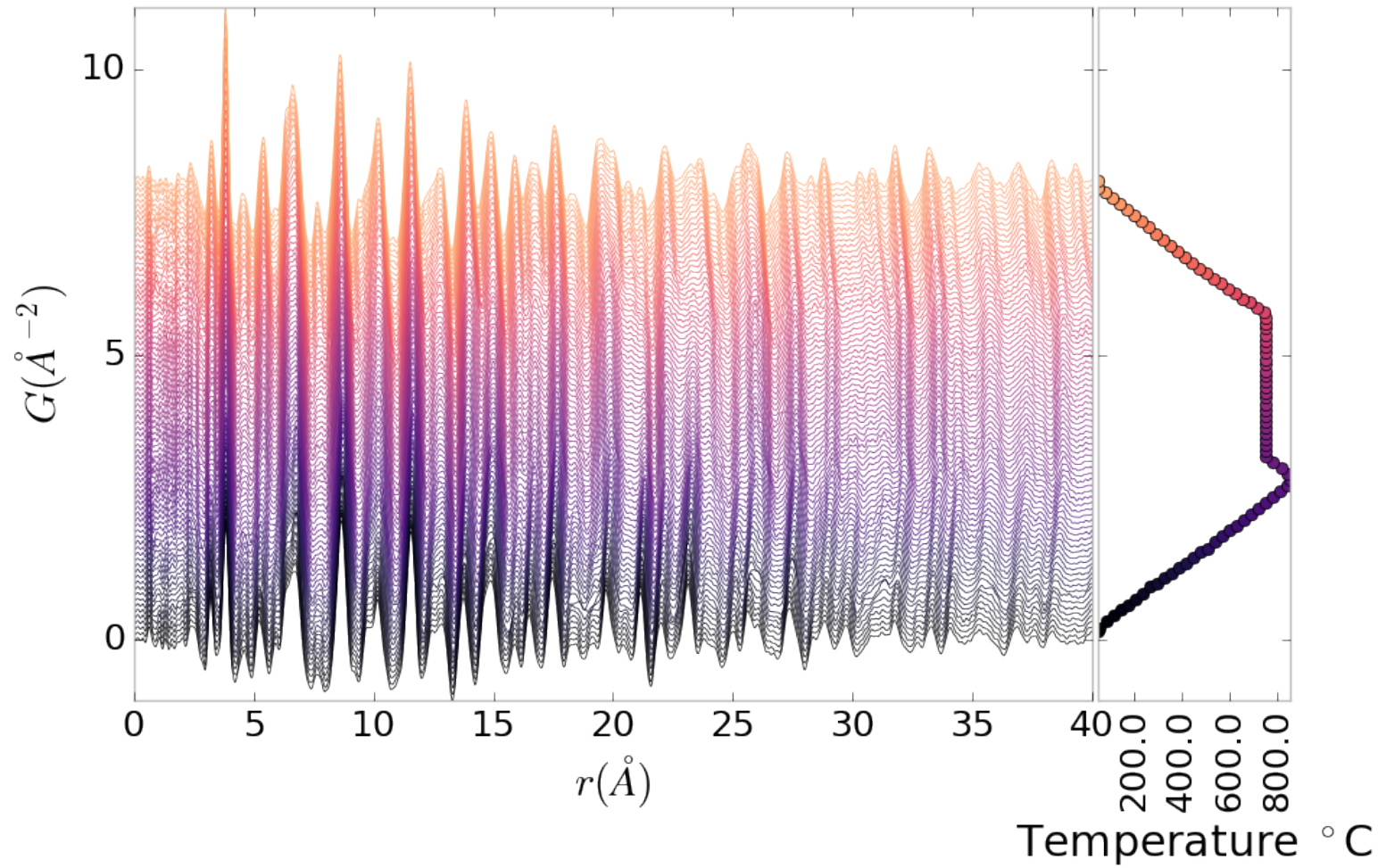


Figure 6.1: PDF as a function of temperature for as synthesized PNO showing the full PDF

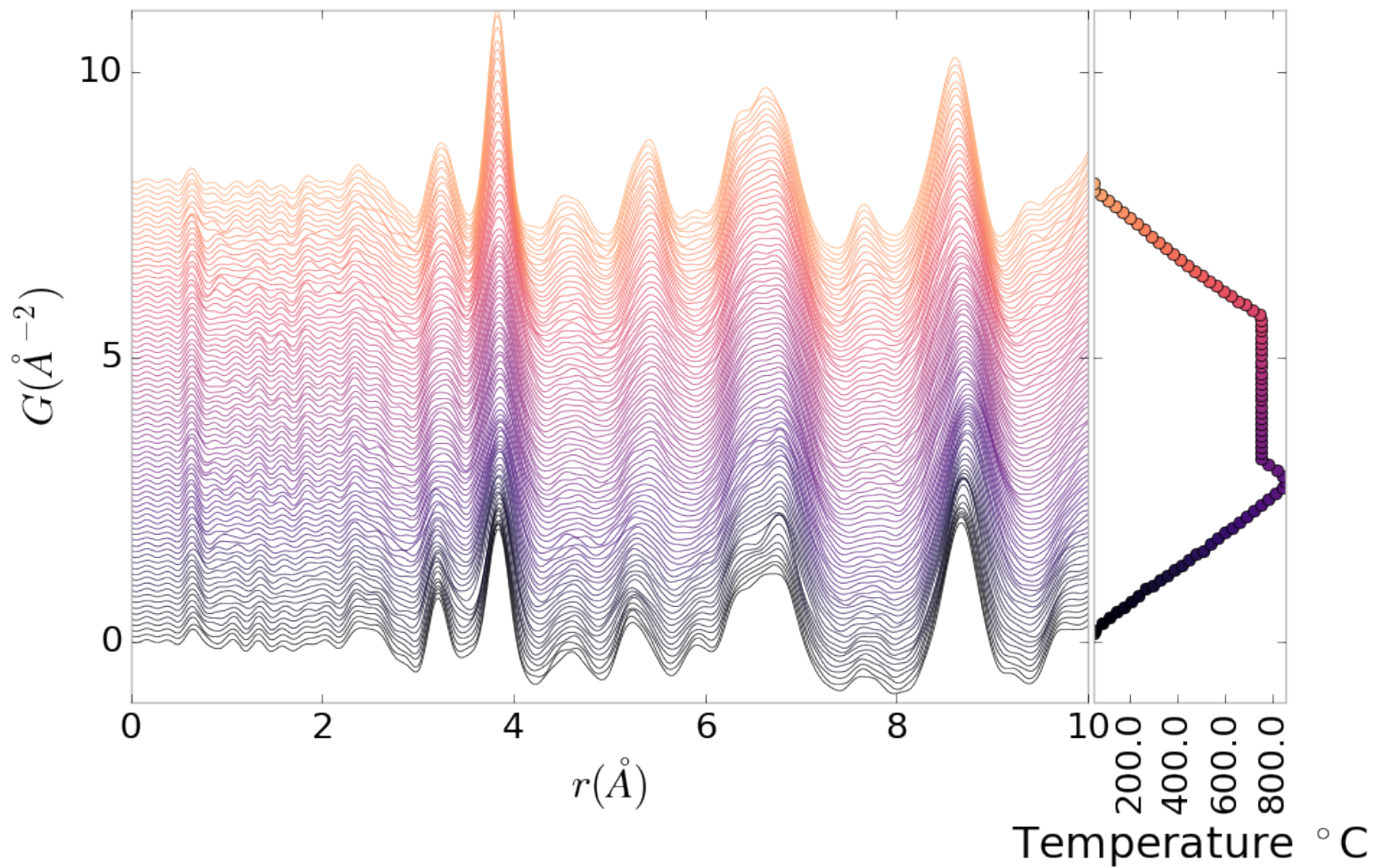


Figure 6.2: PDF as a function of temperature for as synthesized PNO showing a close up on the short range section

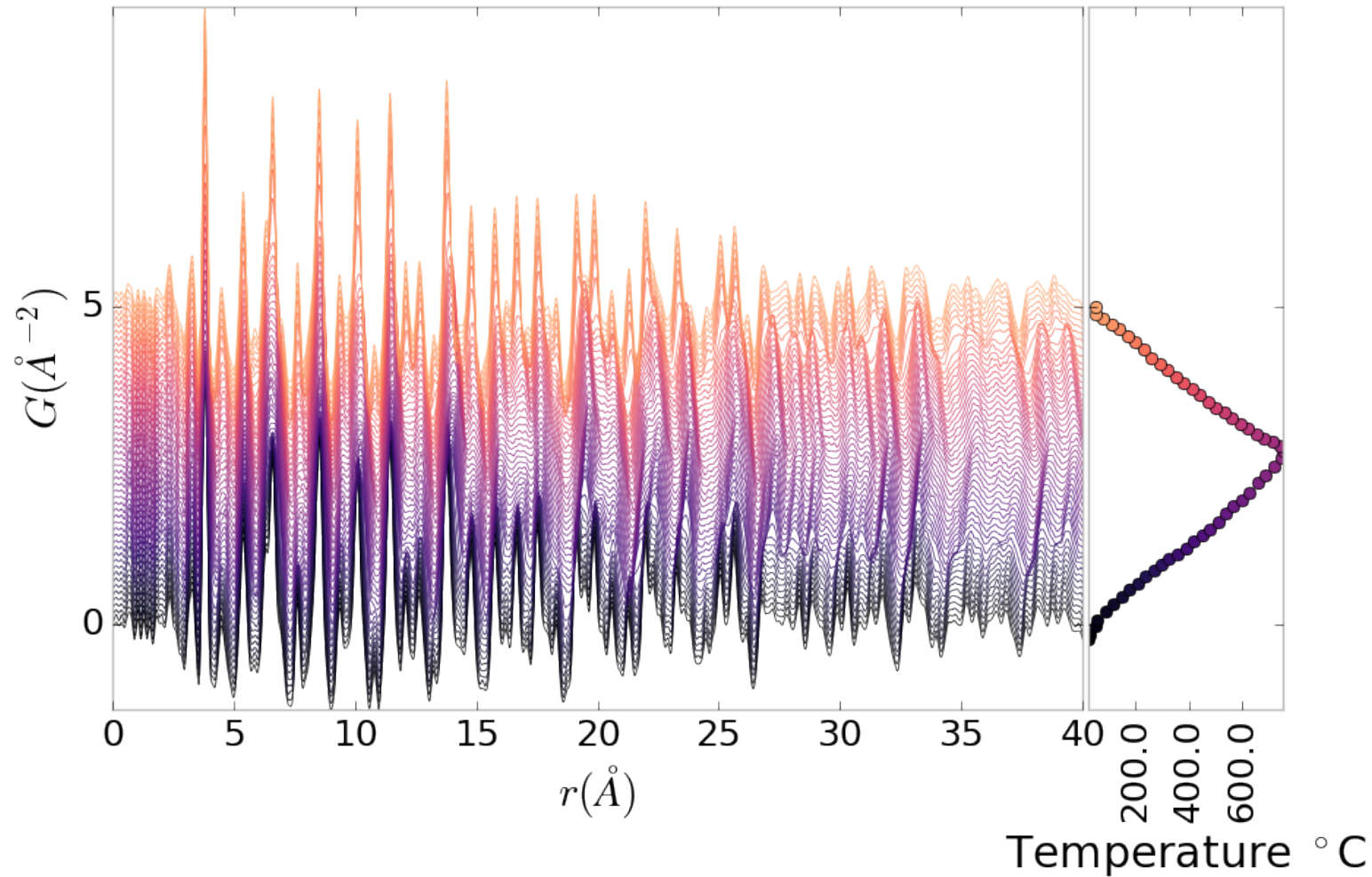


Figure 6.3: PDF as a function of temperature for PNO annealed at 750 °C for 25 hours showing the full PDF

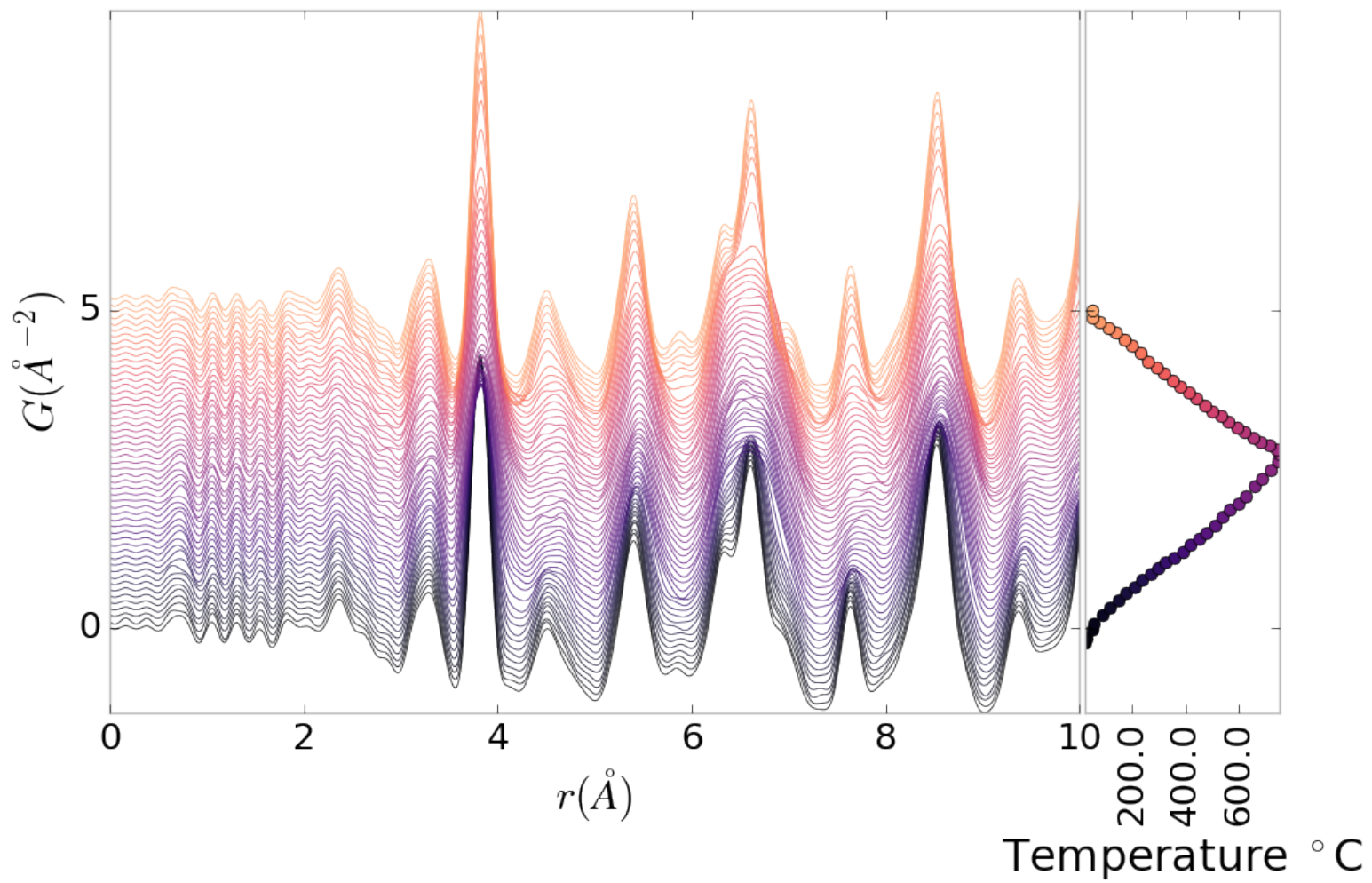


Figure 6.4: PDF as a function of temperature for PNO annealed at $750 \text{ }^{\circ}\text{C}$ for 25 hours showing a close up on the short range section

$I(Q)$

The annealed samples figures, 6.3 and 6.4, tell a rather different story. In this case the PDF shows significant peak shifts and broadening, especially at higher interatomic distances. Some peaks completely disappear, like the peak at 12 Å. Similar results were also observed for samples with longer annealing times, as shown in the appendix.

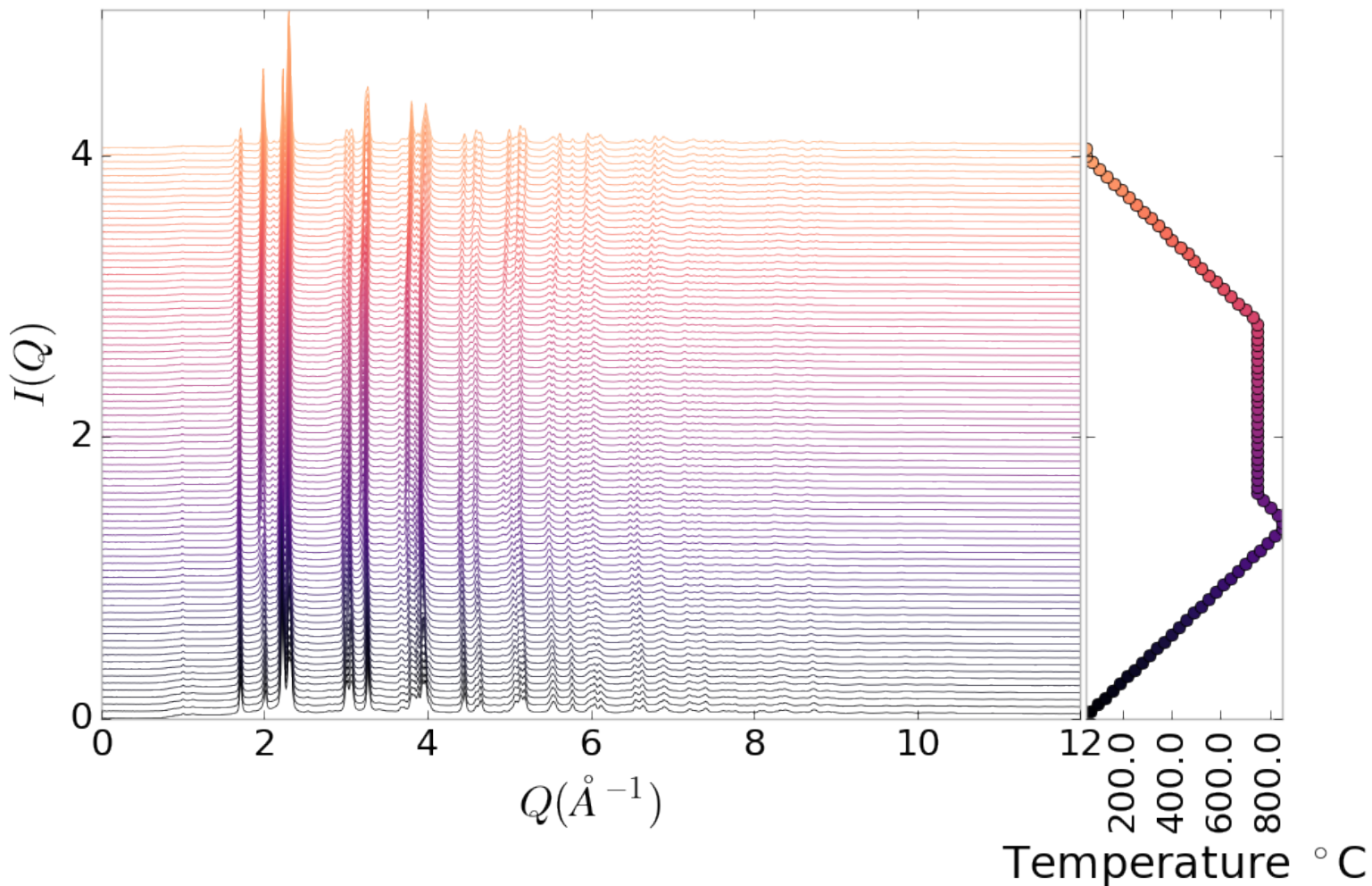


Figure 6.5: $I(Q)$ as a function of temperature for as synthesized PNO showing the full XRD

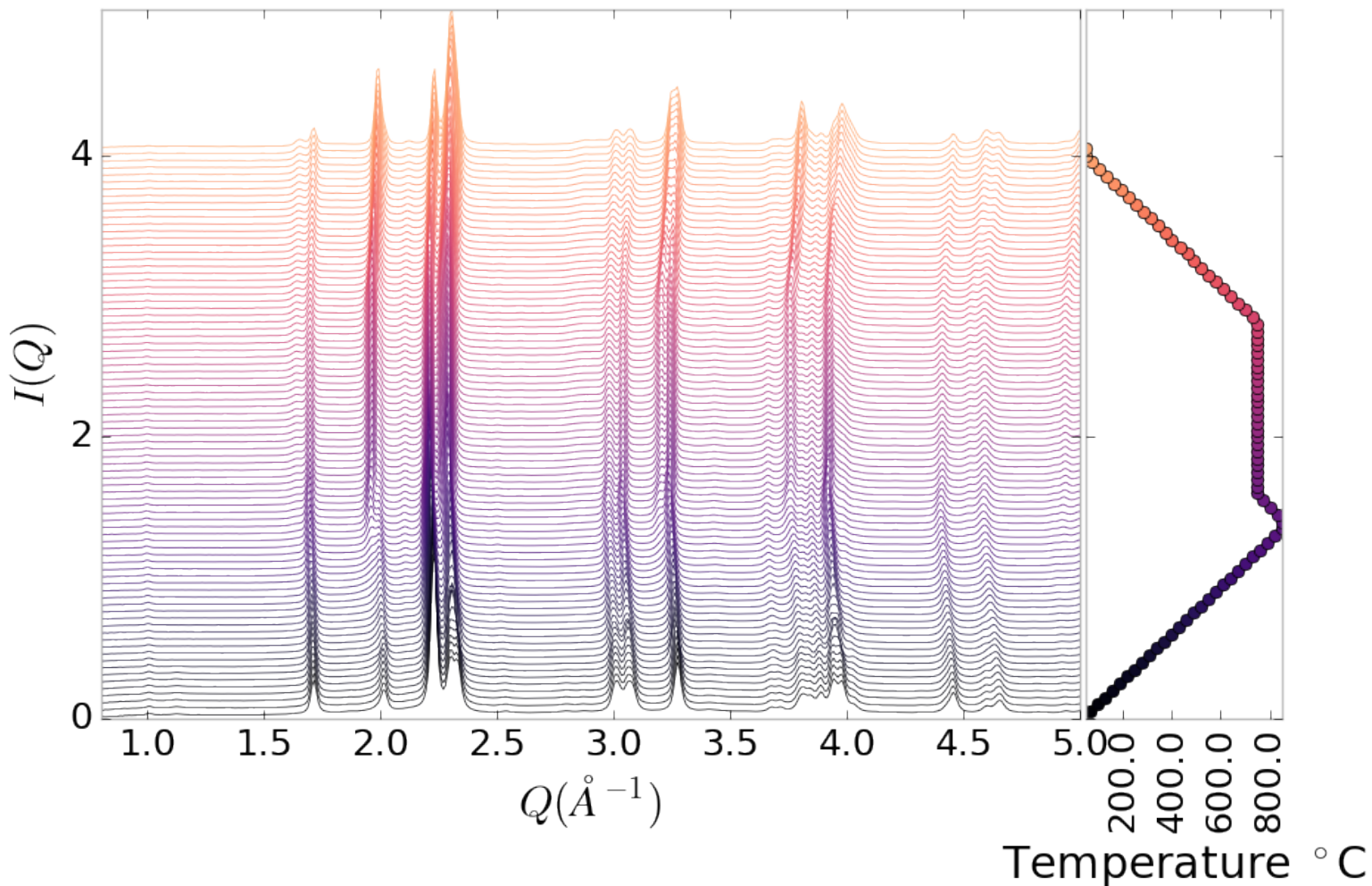


Figure 6.6: $I(Q)$ as a function of temperature for as synthesized PNO showing a close up on the low Q section

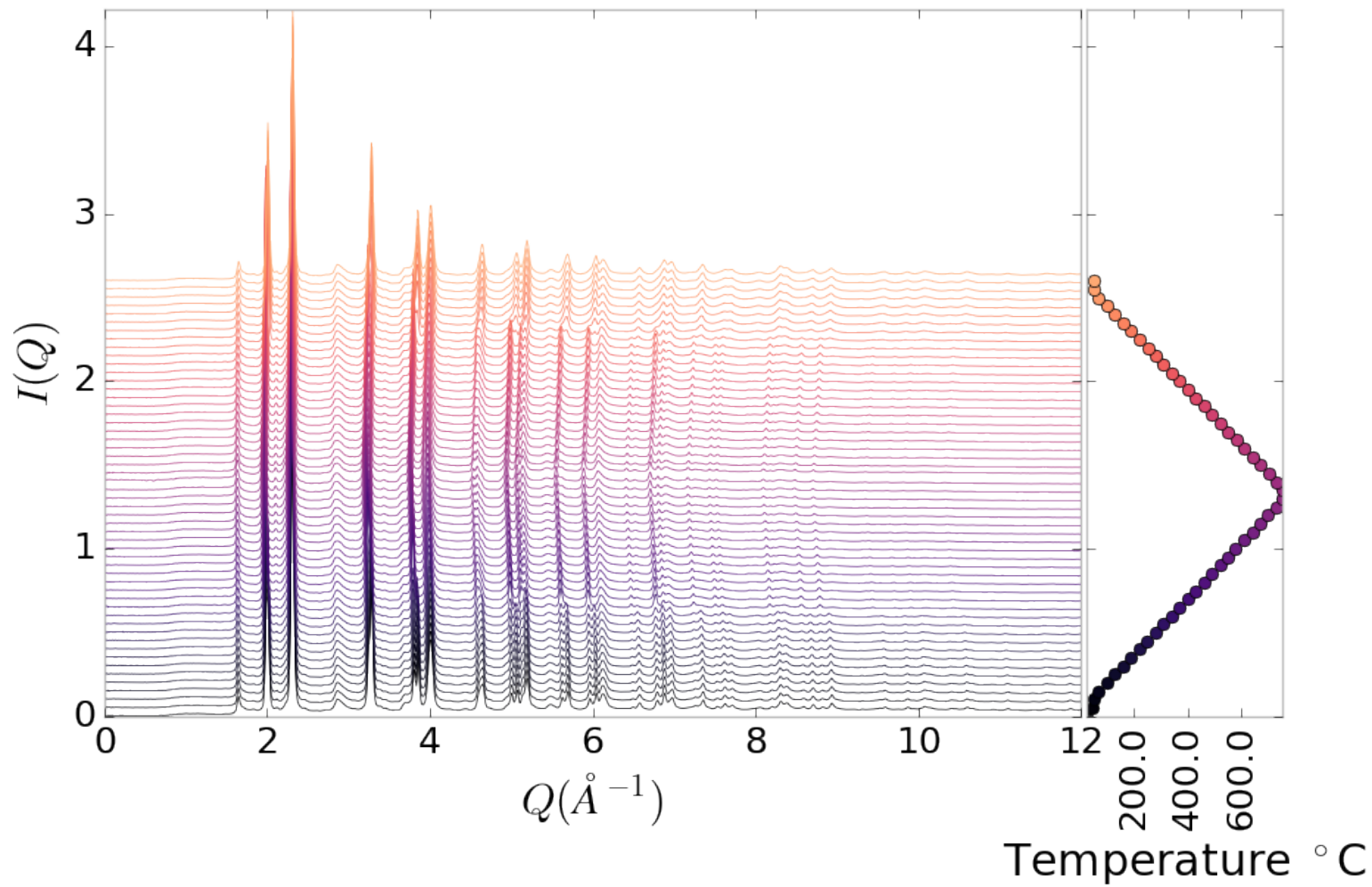


Figure 6.7: $I(Q)$ as a function of temperature for PNO annealed at 750 $^{\circ}\text{C}$ for 25 hours showing the full XRD

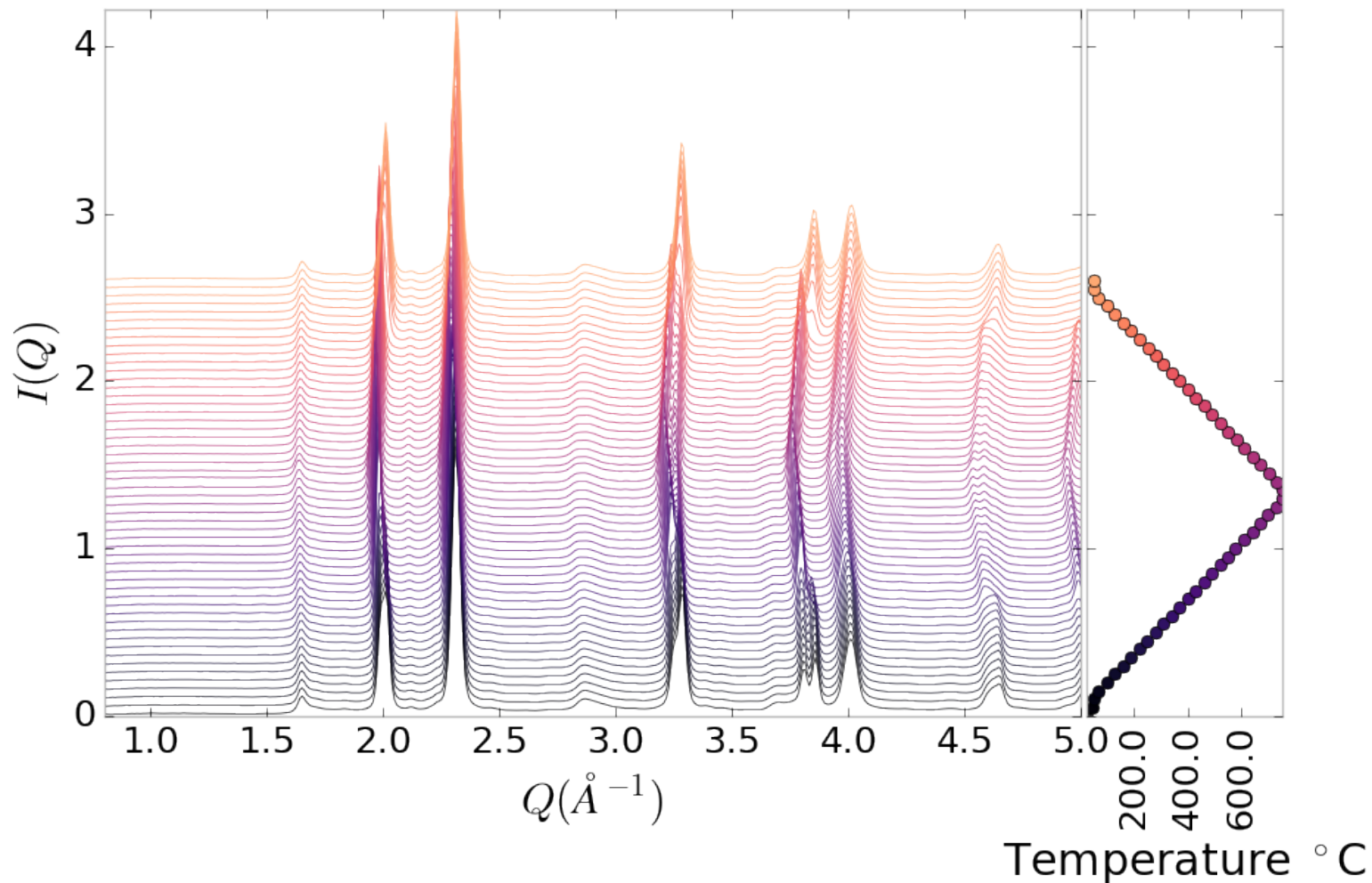


Figure 6.8: $I(Q)$ as a function of temperature for PNO annealed at 750 $^{\circ}\text{C}$ for 25 hours showing a close up on the low Q section

Inter Sample Comparison

Figures A.26 and A.20 show a very interesting contrast. Figure A.26 show significant differences in the $I(Q)$ between the as-synthesized and annealed PNO, which could be associated with the more degradation present in the annealed samples. However, figure A.20 shows very little difference in the PDF between the various annealing times. This discrepancy seems to point to some kind of disorder which changes the interatomic distances very little but changes the symmetry enough to change the Bragg reflections.

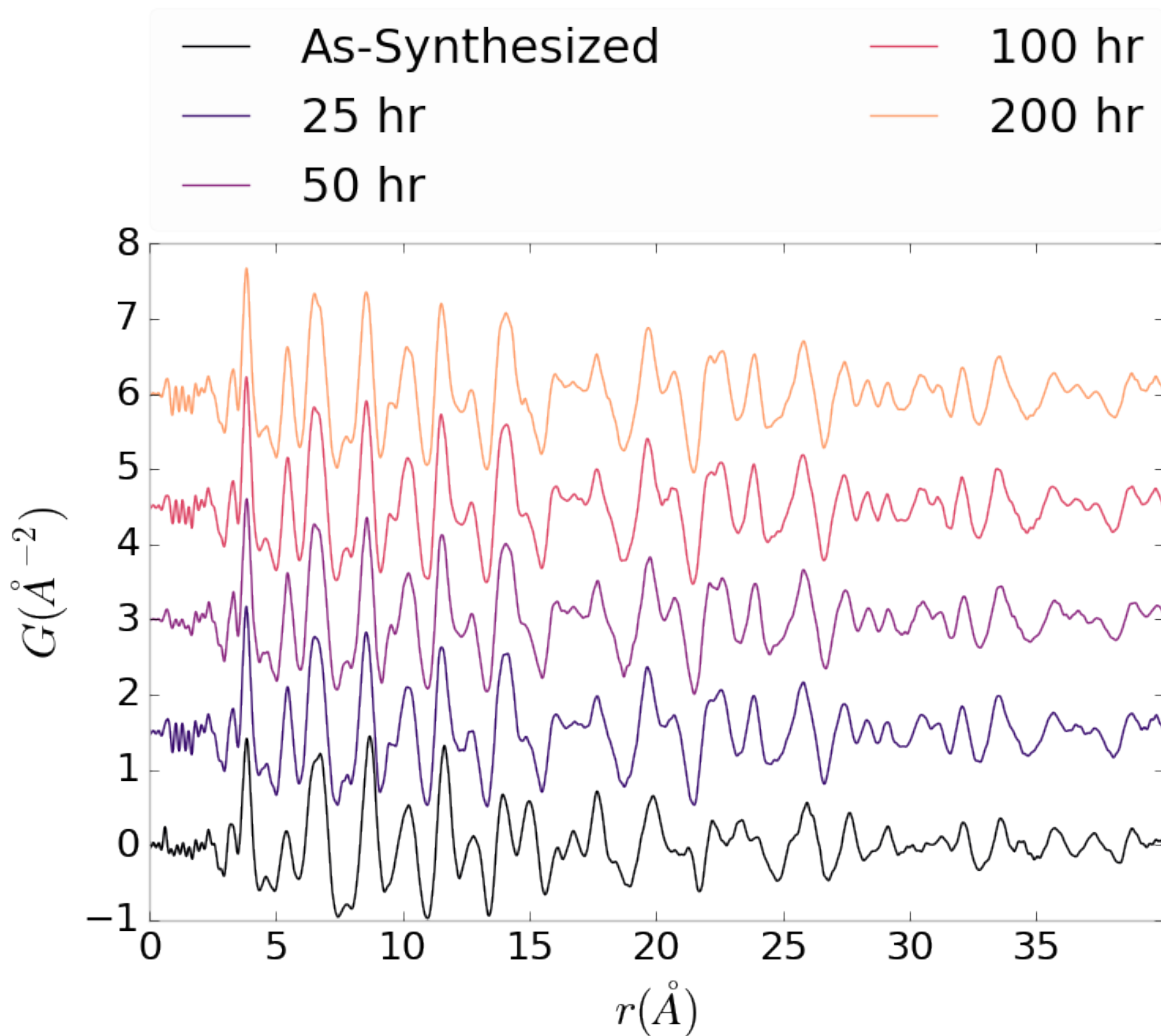


Figure 6.9: Comparison of PNO sample PDFs as a function of annealing time high-temp

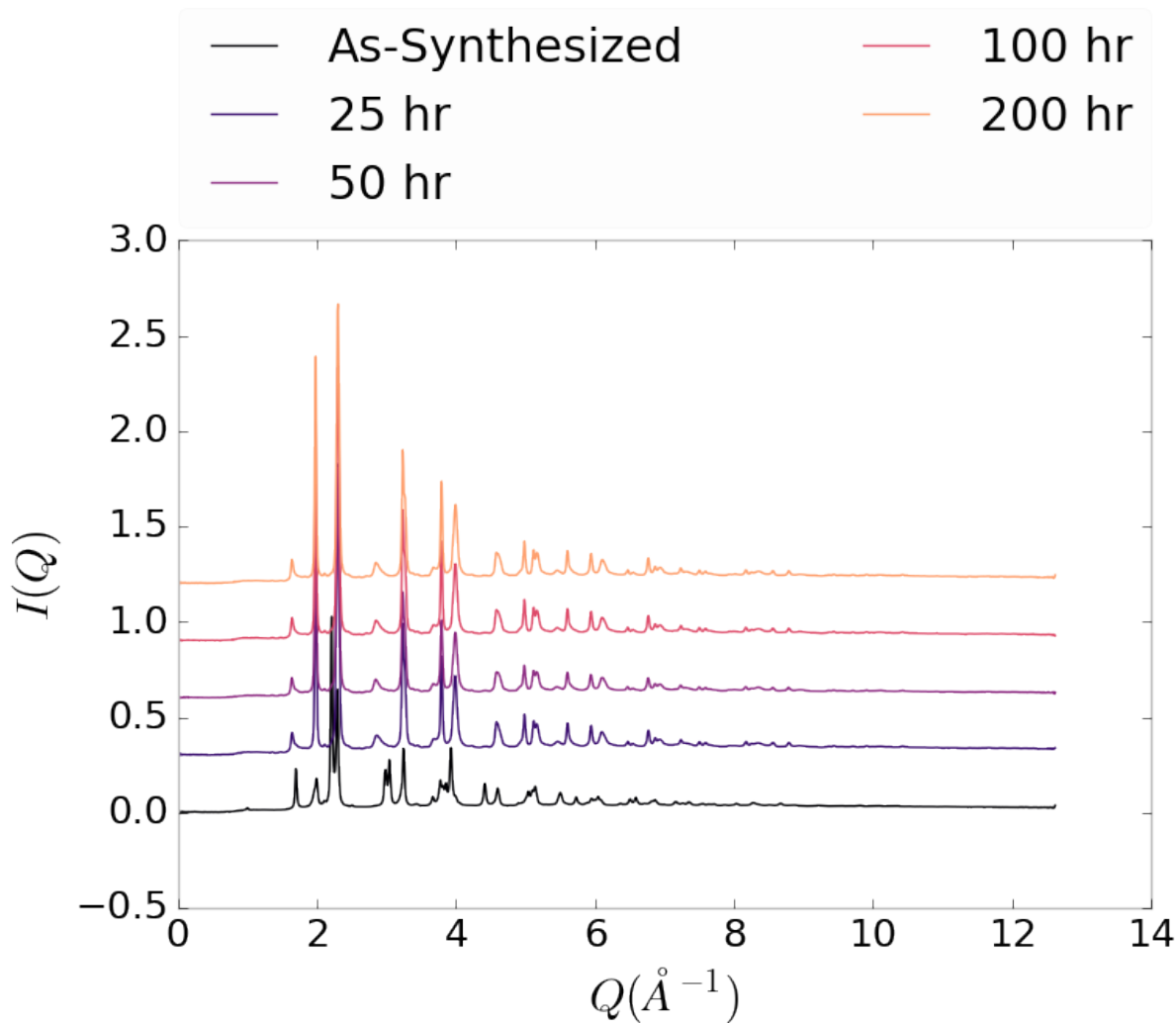


Figure 6.10: Comparison of PNO sample $I(Q)$ as a function of annealing time high-temp

6.5 SIMULATION

Simulations have not been run yet on these PNO samples. Solving the structures of these samples is expected to be more difficult than the NP benchmarks previously solved. The difficulty of these simulations is due to:

1. The PDF's insensitivity to the oxygen positions, due to the poor x-ray scattering off the very electron poor oxygen.
2. The large difference in mass between the oxygen and other atoms, causing the dynamics of the simulation to be governed by oxygen motion, necessitating long simulation times to obtain movement of the other atoms.
3. The large parameter space caused by potential defects and degradation products. Without knowing that the starting phase is pure, it is difficult to even produce starting structures, since the simulation will need to explore all the potential defect/degenerated structures.

6.6 CONCLUSIONS

X-ray total scattering and x-ray powder diffraction data was obtained on Pr_2NiO_4 powder samples annealed for various lengths of time. In-situ studies on the beamline were performed to understand how the structure of each of these powders changes at operating temperatures. The data was processed with the previously discussed Q binning, masking, and integration methodology. The PDF results show very little change in the structure for the as synthesized sample. However, the PDFs show a large change in the previously annealed samples. These changes seem to produce PDFs similar to the as-synthesized PNO at operating temperatures. This would seem to imply that the source of the anomalous PNO phase/power density relationship may be due to the adoption of an active structure upon heating which is universal despite

the amount of thermal degradation observed at room temperature. In contrast to the PDF results, the XRD results seem to show significant changes in the PNO structure, both with ex-situ and in-situ annealing. The XRDs show the degradation of the PNO into various phases, potentially including Pr_2O_{11} , and higher ordered Pr based phases. The discrepancy between these two results is quite interesting as it seems that the XRD and PDF results are contradictory. Turbostratic displacements between the layers may be a cause of the PDF/XRD disagreement, as these changes would cause very little change in the local structure observed in the PDF, while causing large changes in the XRD.

CHAPTER 7

CONCLUSION

This work presents one of the most complete end to end approaches to processing, analyzing, and simulating atomic pair distribution function data. The goals of this work were to build a modular, quick, and robust method for handling experimental PDF data and solving atomic structures.

The statistical mechanical PES solvers were designed to robustly find atomic solutions which are global minima of the PES. This was accomplished by using some of the most advanced Monte Carlo algorithms and samplers. The analytical equations for the PES and its gradients were derived to provide the quickest searches.

The PDF gradients were derived and implemented as GPU kernels to further speed up the PES search. The inclusion of the GPUs, combined with the atom pair mapping, were found to provide a 10x to 100x speedup over a multiprocessor based CPU methodology.

The extensive benchmarking of the NUTS-HMC system presented in chapters 2 and 3 showcased the system's robustness, speed, and effectiveness. Interestingly it seems the the simulations also helped to elucidate the relationship between Rw and the resulting fit of the secondary metrics, including radial bond distribution. This is particularly important as it begins to establish Rw goals and a relationship between Rw and the confidence that features from the underlying structure that the PDF represents are reproduced by the structural model which is produced my Monte Carlo modeling. It seems that the threshold for acceptable Rw in Monte Carlo modeling needs to be quite lower than the current literature standards to properly reproduce

the structure.

A novel data processing workflow was also developed which focused on using Q resolution binning to create masks automatically and azimuthally integrate. The Q resolution binning provided a significant improvement in the automated masking robustness, leading to much fewer false positives, as shown by a series of masks generated on simulated and experimental data. The effect of these masks on the median and mean azimuthal integration was also discussed, establishing masks as very important to the removal of the high Q “kink” seen in 2D area detector data. Furthermore, a comparison was drawn between the median and mean integration, showing the median to be more reliable than the mean when working with data that could have residual detector defects. Overall the masking scheme was shown to reduce the standard deviation of the data significantly.

Finally, preliminary results of x-ray total scattering measurements on Pr_2NiO_4 were presented. Interestingly, these results show a strong discrepancy between the PDF and $I(Q)$ data. Where the PDF shows a very static as synthesized structure, despite annealing, the associated $I(Q)$ data shows peak movement and formation. For the pre-annealed samples both the $I(Q)$ and PDF data show peak changes. Interestingly, the PDFs of the as synthesized and pre-annealed samples show very similar local structure at operating temperatures.

Despite all the work presented here there is, of course, more to be done. Implementing new ensembles, like Parallel Tempering, and faster Grand Canonical Monte Carlo, may help to find solutions faster and with less user based parameter tuning. Building the mathematics and software to quickly compute the data from other atomistic experiments including, EXAFS, STEM, and neutron scattering, could help to produce structures which more fully describe the available experimental data. Implementing the existing codebase in a more general High Performance Computing context would allow for the solution of much larger particles and extended solids.

Further benchmarking will help to probe the robustness of the algorithm with other systems, including systems with periodic boundary conditions. Faster scattering data processing will enable a quicker total turn around time from taking experimental images to producing atomic structures.

It is expected that this work will become a standard method for solving atomic structures from x-ray total scattering experiments, having presented one of the most complete x-ray processing and analysis systems.

BIBLIOGRAPHY

- [1] Milinda Abeykoon, Christos D. Malliakas, Pavol Juhás, Emil S. Božin, Mercouri G Kanatzidis, and Simon J L Billinge, *Quantitative nanostructure characterization using atomic pair distribution functions obtained from laboratory electron microscopes*, Zeitschrift fur Kristallographie **227** (2012), no. 5, 248–256.
- [2] Alexandre A. Arnold, Victor Terskikh, Qian Ying Li, Rafik Naccache, Isabelle Marcotte, and John A. Capobianco, *Structure of NaYF₄ upconverting nanoparticles: A multinuclear solid-state NMR and DFT computational study*, Journal of Physical Chemistry C **117** (2013), no. 48, 25733–25741.
- [3] Simon J L Billinge and Takeshi Egami, *Underneath the Bragg Peaks: Structural Analysis of complex Materials*, vol. Volume 16, Pergamon, 2012.
- [4] Simon J L Billinge and Igor Levin, *The problem with determining atomic structure at the nanoscale.*, Science (New York, N.Y.) **316** (2007), no. 5824, 561–565.
- [5] P. E. Blöchl, *Projector augmented-wave method*, Physical Review B **50** (1994), no. 24, 17953–17979.
- [6] Gary K. Chen and Yunfei Guo, *Discovering epistasis in large scale genetic association studies by exploiting graphics cards*, Frontiers in Genetics **4** (2013), no. DEC, 1–12.
- [7] Joshua J Choi, Xiaohao Yang, Zachariah M Norman, Simon J L Billinge, and Jonathan S Owen, *Structure of methylammonium lead iodide within mesoporous titanium dioxide: Active material in high-performance perovskite solar cells*, Nano Letters **14** (2014), no. 1, 127–133.
- [8] Peter J. Chupas, Karena W. Chapman, Charles Kurtz, Jonathan C. Hanson, Peter L. Lee, and Clare P. Grey, *A versatile sample-environment cell for non-ambient X-ray scattering experiments*, Journal of Applied Crystallography **41** (2008), no. 4, 822–824.
- [9] PJ Chupas, X Qiu, JC Hanson, PL Lee, CP Grey, and SJL Billinge, *Rapid-*

- acquisition pair distribution function (RA-PDF) analysis*, Journal of Applied Crystallography **36** (2003), 1342–1347.
- [10] Matthew J. Cliffe, Martin T. Dove, D. A. Drabold, and Andrew L. Goodwin, *Structure determination of disordered materials from diffraction data*, Physical Review Letters **104** (2010), no. 12, 1–4.
 - [11] Matthew J Cliffe and Andrew L Goodwin, *Nanostructure determination from the pair distribution function: a parametric study of the INVERT approach.*, Journal of physics. Condensed matter : an Institute of Physics journal **25** (2013), no. 45, 454218.
 - [12] Chunhua Cui, Lin Gan, Marc Heggen, Stefan Rudi, and Peter Strasser, *Compositional segregation in shaped Pt alloy nanoparticles and their structural behaviour during electrocatalysis.*, Nature materials **12** (2013), no. 12, 765–771.
 - [13] Juarez L F Da Silva, Hyoung Gyu Kim, Maurício J. Piotrowski, Maurício J. Prieto, and Germano Tremiliosi-Filho, *Reconstruction of core and surface nanoparticles: The example of Pt55 and Au55*, Physical Review B - Condensed Matter and Materials Physics **82** (2010), no. 20, 1–6.
 - [14] Emir Dogdibegovic, Christopher J. Wright, and Xiao-Dong Zhou, *Stability and Activity of $(Pr_{1-x}Nd_x)_2NiO_4$ as Cathodes for Solid Oxide Fuel Cells: I. Quantification of Phase Evolution in Pr_2NiO_4* , Journal of the American Ceramic Society **5** (2016), 1–5.
 - [15] Simon Duane, A. D. Kennedy, Brian J. Pendleton, and Duncan Roweth, *Hybrid Monte Carlo*, Physics Letters B **195** (1987), no. 2, 216–22.
 - [16] Timur Dykhne, Ryan Taylor, Alastair Florence, and Simon J L Billinge, *Data requirements for the reliable use of atomic pair distribution functions in amorphous pharmaceutical fingerprinting.*, Pharmaceutical research **28** (2011), no. 5, 1041–8.
 - [17] C L Farrow, P Juhas, J W Liu, D Bryndin, E S Božin, J Bloch, Th Proffen, and S J L Billinge, *PDFfit2 and PDFgui: computer programs for studying nanostructure in crystals.*, Journal of Physics. Condensed Matter : an Institute of Physics journal **19** (2007), no. 33, 335219.
 - [18] Christopher L Farrow and Simon J L Billinge, *Relationship between the atomic pair distribution function and small-angle scattering: implications for modeling*

of nanoparticles., Acta Crystallographica Section A Foundations of Crystallography **65** (2009), no. Pt 3, 232–9 (en).

- [19] Riccardo Ferrando, Julius Jellinek, and Roy L Johnston, *Nanoalloys: From Theory to Applications of Alloy Clusters and Nanoparticles*, Chemical Reviews **108** (2008), no. 3, 846–904.
- [20] Anatoly Frenkel, *Solving the 3D structure of metal nanoparticles*, Zeitschrift für Kristallographie **222** (2007), no. 11, 605–611.
- [21] Carmelo Giacovazzo, Hugo Luis Monaco, Gilberto Artioli, Davide Viterbo, Marco Milanesio, Gastone Gilli, Paola Gilli, Giuseppe Zanotti, Giovanni Ferraris, and Michele Catti, *Fundamentals of Crystallography*, Oxford University Press, 1992.
- [22] Benjamin Gilbert, Jasmine J. Erbs, R. Lee Penn, Valeri Petkov, Dino Spagnoli, and Glenn A. Waychunas, *A disordered nanoparticle model for 6-line ferrihydrite*, American Mineralogist **98** (2013), no. 8-9, 1465–1476.
- [23] Benjamin Gilbert, Feng Huang, Hengzhong Zhang, Glenn A. Waychunas, and Jillian F Banfield, *Nanoparticles: strained and stiff.*, Science (New York, N.Y.) **305** (2004), no. 5684, 651–654.
- [24] Md Matthew D. Hoffman and Andrew Gelman, *The No-U-Turn Sampler: Adaptively Setting Path Lengths in Hamiltonian Monte Carlo*, The Journal of Machine Learning Research **15** (2014), no. 2008, 1593–1623.
- [25] W J Huang, R Sun, J Tao, L D Menard, R G Nuzzo, and J M Zuo, *Coordination-dependent surface atomic contraction in nanocrystals revealed by coherent diffraction.*, Nature Materials **7** (2008), no. 4, 308–313.
- [26] Pablo D Jadzinsky, Guillermo Calero, Christopher J Ackerson, David A Bushnell, and Roger D Kornberg, *Structure of a thiol monolayer-protected gold nanoparticle at 1.1 Å resolution.*, Science (New York, N.Y.) **318** (2007), no. 5849, 430–433.
- [27] I. K. Jeong, R. H. Heffner, M. J. Graf, and S. J. L. Billinge, *Lattice dynamics and correlated atomic motion from the atomic pair distribution function*, (2002), 9.
- [28] P. Juhás, T. Davis, C. L. Farrow, and S. J. L. Billinge, *PDFgetX3 : a rapid and highly automatable program for processing powder diffraction data into total*

- scattering pair distribution functions*, Journal of Applied Crystallography **46** (2013), no. 2, 560–566 (en).
- [29] A. Kassiba, M. Makowska-Janusik, J. Bouclé, J. Bardeau, A. Bulou, and N. Herlin-Boime, *Photoluminescence features on the Raman spectra of quasistoechiometric SiC nanoparticles: Experimental and numerical simulations*, Physical Review B **66** (2002), no. 15, 1–7.
 - [30] Jérôme Kieffer and Dimitrios Karkoulis, *PyFAI, a versatile library for azimuthal regrouping*, Journal of Physics: Conference Series **425** (2013), 202012.
 - [31] G. Kresse and O.J. Hafner, *Ab initio molecular-dynamics simulation of the liquid-metal-amorphous-semiconductor transition in germanium*, Physical Review B **49** (1994), no. 20, 14251–14269.
 - [32] G. Kresse and J. Hafner, *Ab initio molecular dynamics for liquid metals*, Physical Review B **47** (1993), no. 1, 558–561.
 - [33] Yan Li, Giulia Galli, and François Gygi, *Electronic structure of thiolate-covered gold nanoparticles: Au₁₀₂(MBA)₄₄*, ACS Nano **2** (2008), no. 9, 1896–1902.
 - [34] L D Marks, *Experimental studies of small particle structures*, Reports on Progress in Physics **57** (1994), no. 6, 603–649 (en).
 - [35] A. S. Masadeh, E. S. Božin, C. L. Farrow, G. Paglia, P. Juhas, S. J. L. Billinge, A. Karkamkar, and M. G. Kanatzidis, *Quantitative size-dependent structure and strain determination of CdSe nanoparticles using atomic pair distribution function analysis*, Physical Review B - Condensed Matter and Materials Physics **76** (2007), no. 11, 115413.
 - [36] R L McGreevy and L Pusztai, *Reverse Monte Carlo Simulation: A New Technique for the Determination of Disordered Structures*, Molecular Simulation **1** (1988), no. 6, 359–367.
 - [37] Donald A. McQuarrie, *Statistical Mechanics*, University Science Books, Sausalito, CA, 2000.
 - [38] Radford M Neal, *Probabilistic Inference Using Markov Chain Monte Carlo Methods*, Intelligence **45** (1993), no. September, 144.

- [39] Radford M. Neal, *MCMC Using Hamiltonian Dynamics*, Handbook of Markov Chain Monte Carlo (Steve Brooks, Andrew Gelman, Galin L. Jones and Xiao-Li Meng, eds.), Chapman and Hall/CRC, 2011, pp. 113–162.
- [40] Katharine Page, Taylor C. Hood, Thomas Proffen, and Reinhard B. Neder, *Building and refining complete nanoparticle structures with total scattering data*, Journal of Applied Crystallography **44** (2011), no. 2, 327–336 (en).
- [41] B R Pauw, *Corrigendum: Everything SAXS: small-angle scattering pattern collection and correction (2013 J. Phys.: Condens. Matter 25 383201)*, Journal of Physics: Condensed Matter **26** (2014), no. 23, 239501.
- [42] Vitalij Pecharsky and Peter Zavalij, *Fundamentals of Powder Diffraction and Structural Characterization of Materials*, Springer Science, 2009.
- [43] John P. Perdew, Kieron Burke, and Matthias Ernzerhof, *Generalized Gradient Approximation Made Simple*, Physical Review Letters **77** (1996), no. 18, 3865–3868.
- [44] Andrew A. Peterson, *Global optimization of adsorbate-surface structures while preserving molecular identity*, Topics in Catalysis **57** (2014), no. 1-4, 40–53.
- [45] Valeri Petkov, Youngmin Lee, Shouheng Sun, and Yang Ren, *Noncrystallographic atomic arrangement driven enhancement of the catalytic activity of Au nanoparticles*, Journal of Physical Chemistry C **116** (2012), no. 50, 26668–26673.
- [46] Valeri Petkov, Binay Prasai, Yang Ren, Shiyao Shan, Jin Luo, Pharrah Joseph, and Chuan-Jian Zhong, *Solving the nanostructure problem: exemplified on metallic alloy nanoparticles*, Nanoscale **6** (2014), no. 17, 1–11.
- [47] Valeri Petkov, Shiyao Shan, Peter Chupas, Jun Yin, Lefu Yang, Jin Luo, and Chuan-Jian Zhong, *Noble-transition metal nanoparticle breathing in a reactive gas atmosphere.*, Nanoscale **5** (2013), no. 16, 7379–87.
- [48] Th. Proffen and R. B. Neder, *DISCUS: a Program for Diffuse Scattering and Defect-Structure Simulation*, Journal of Applied Crystallography **30** (1997), 171–175.
- [49] Erin L. Redmond, Brian P. Setzler, Pavol Juhas, Simon J. L. Billinge, and Thomas F. Fuller, *In-Situ Monitoring of Particle Growth at PEMFC Cathode under Accelerated Cycling Conditions*, Electrochemical and Solid-State Letters **15** (2012), no. 5, B72 (en).

- [50] H. W. Sheng, M. J. Kramer, A. Cadien, T. Fujita, and M. W. Chen, *Highly optimized embedded-atom-method potentials for fourteen FCC metals*, Physical Review B - Condensed Matter and Materials Physics **83** (2011), no. 13, 134118.
- [51] Chenyang Shi, Majid Beidaghi, Michael Naguib, Olha Mashtalir, Yury Gogotsi, and Simon J L Billinge, *Structure of Nanocrystalline Ti₃C₂ MXene Using Atomic Pair Distribution Function.*, Physical Review Letters **112** (2014), no. March, 125501.
- [52] Randall Q. Snurr, Alexis T. Bell, and Doros N. Theodorou, *Prediction of adsorption of aromatic hydrocarbons in silicalite from grand canonical Monte Carlo simulations with biased insertions*, The Journal of Physical Chemistry **97** (1993), no. 51, 13742–13752 (EN).
- [53] Chang Q. Sun, *Size dependence of nanostructures: Impact of bond order deficiency*, Progress in Solid State Chemistry **35** (2007), no. 1, 1–159.
- [54] X. Yang, P. Juhás, and S. J L Billinge, *On the estimation of statistical uncertainties on powder diffraction and small-angle scattering data from two-dimensional X-ray detectors*, Journal of Applied Crystallography **47** (2014), no. 4, 1273–1283.
- [55] Masatomo Yashima, Makiko Enoki, Takahiro Wakita, Roushown Ali, Yoshitaka Matsushita, Fujio Izumi, and Tatsumi Ishihara, *Structural Disorder and Diffusional Pathway of Oxide Ions in a Doped Pr₂NiO₄ -Based Mixed Conductor*, Journal of the American Chemical Society **130** (2008), no. 9, 2762–2763.
- [56] Hengzhong Zhang, Bin Chen, Jillian F. Banfield, and Glenn A. Waychunas, *Atomic structure of nanometer-sized amorphous TiO₂*, Physical Review B **78** (2008), no. 21, 214106.
- [57] X.-D. Zhou, J.W. Templeton, Z. Nie, H. Chen, J.W. Stevenson, and L.R. Pederson, *Electrochemical performance and stability of the cathode for solid oxide fuel cells: V. high performance and stable Pr₂NiO₄ as the cathode for solid oxide fuel cells*, Electrochimica Acta **71** (2012), 44–49.

APPENDIX A

SUPPLEMENTAL INFORMATION: PHASE CHANGES AND
ANNEALING DYNAMICS OF Pr_2NiO_4 AND ITS
DERIVATIVES

Intra Sample Comparison

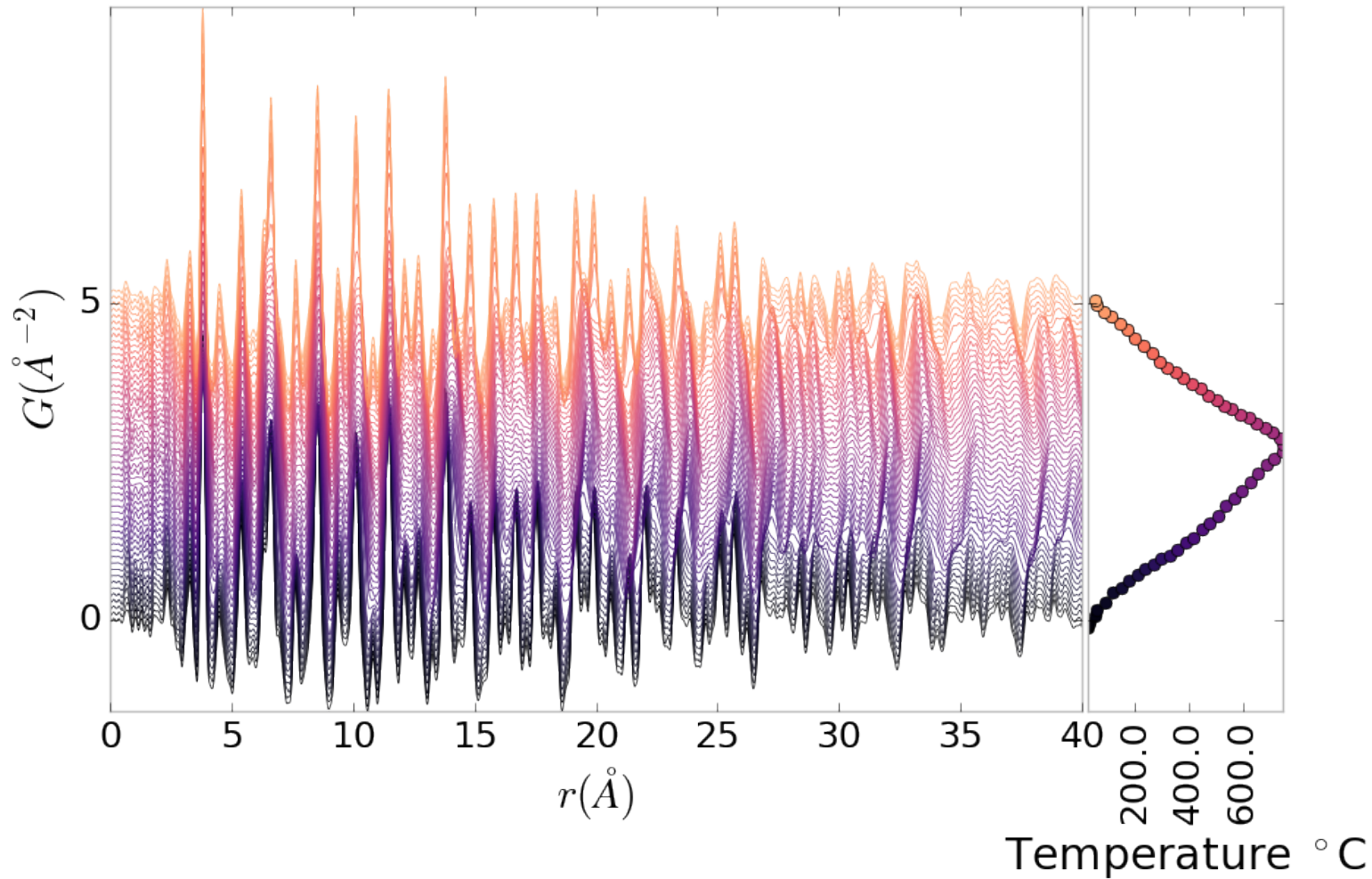


Figure A.1: PDF as a function of temperature for PNO annealed at 750 $^{\circ}\text{C}$ for 50 hours showing the full PDF

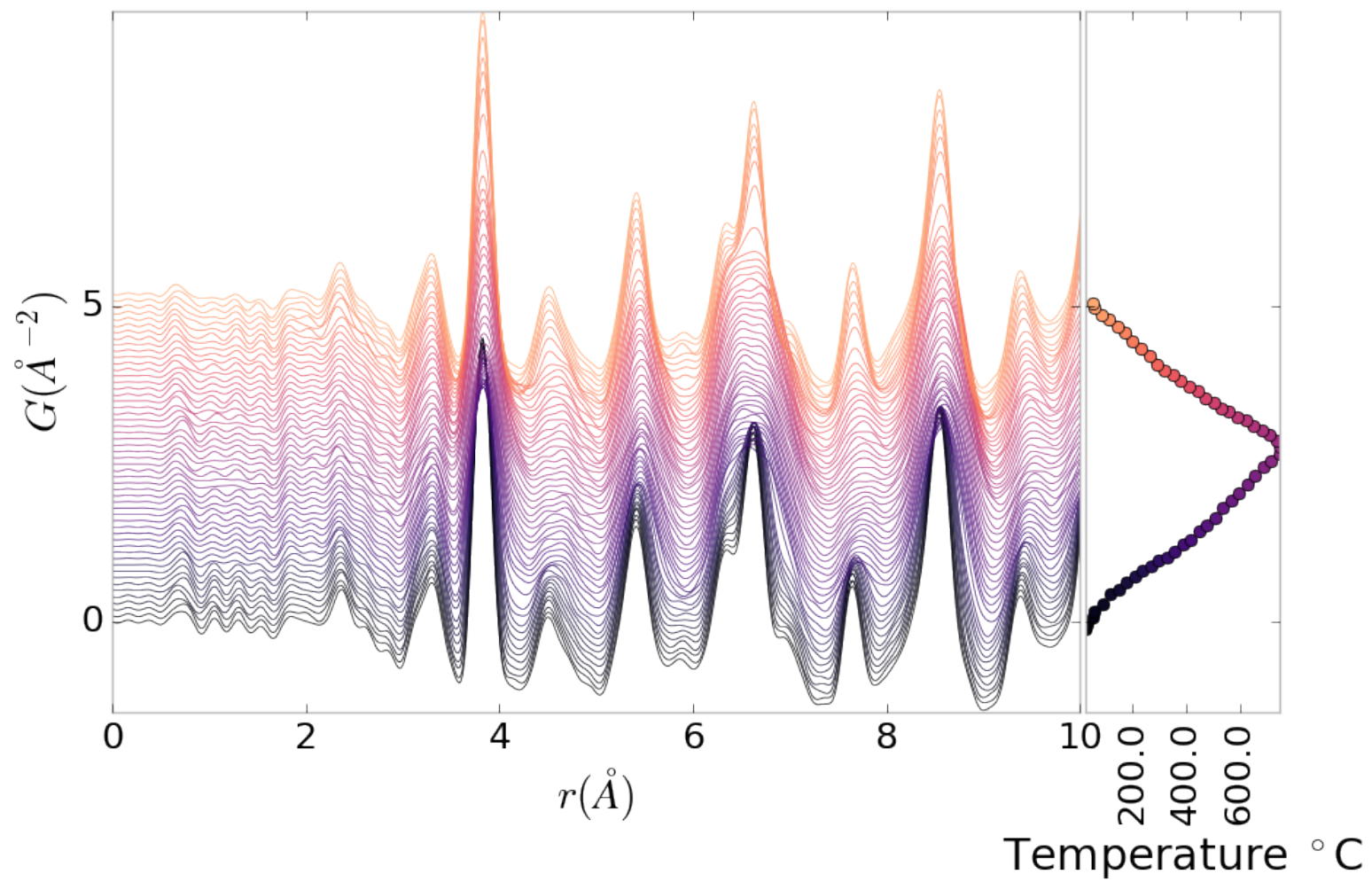


Figure A.2: PDF as a function of temperature for PNO annealed at 750 °C for 50 hours showing a close up on the short range section

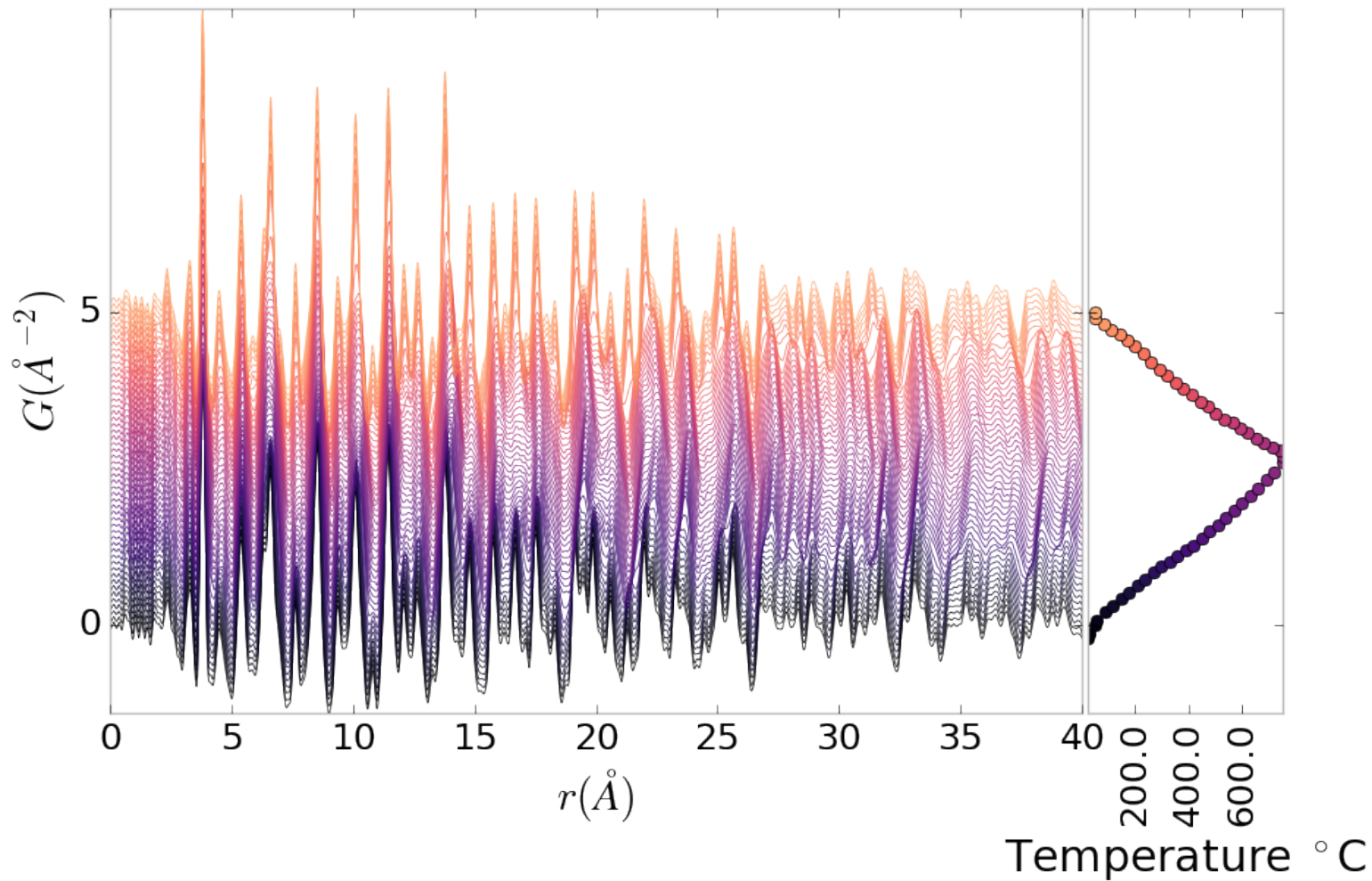


Figure A.3: PDF as a function of temperature for PNO annealed at $750 \text{ } ^{\circ}\text{C}$ for 100 hours showing the full PDF

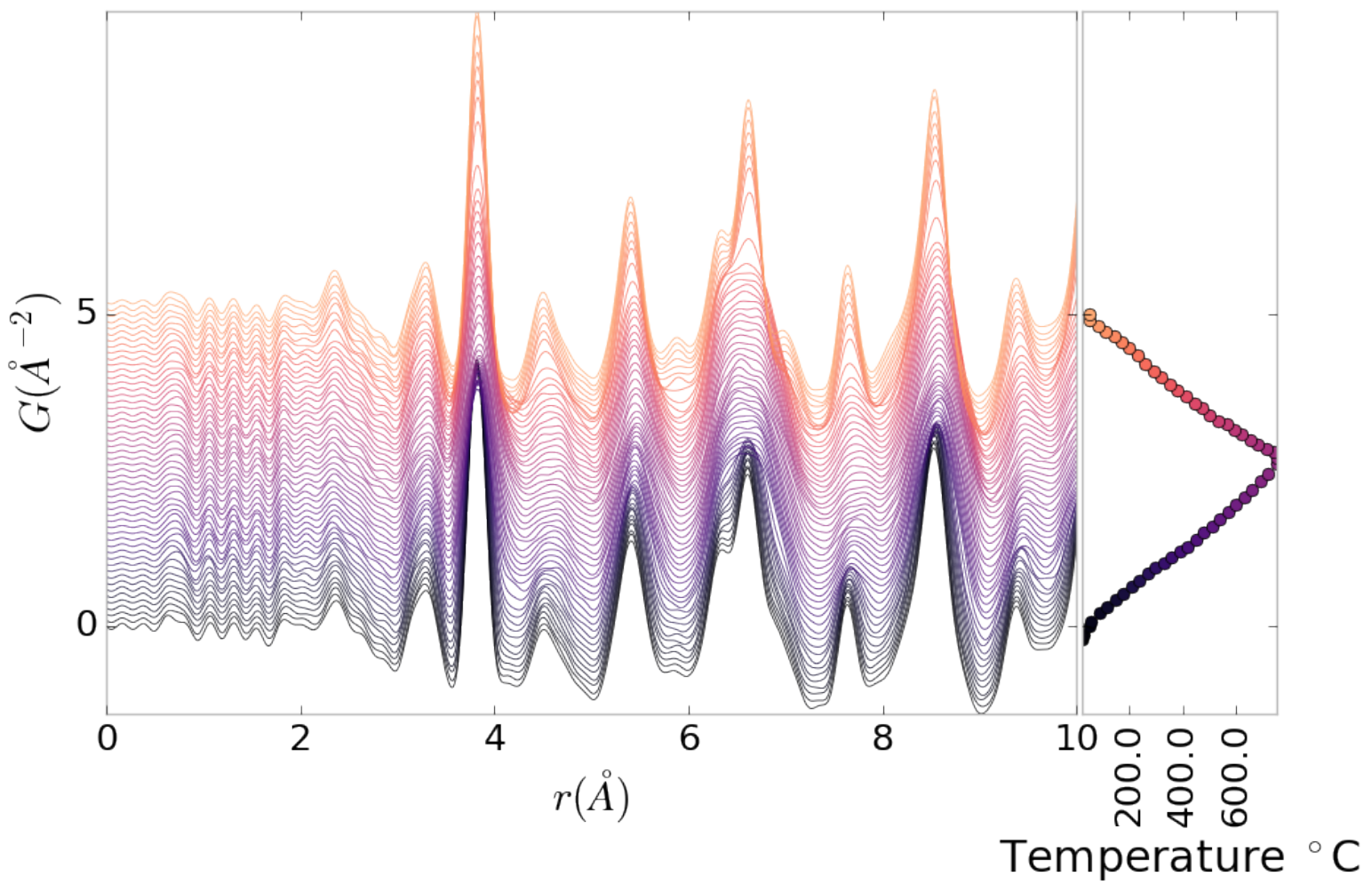


Figure A.4: PDF as a function of temperature for PNO annealed at 750 °C for 100 hours showing a close up on the short range section

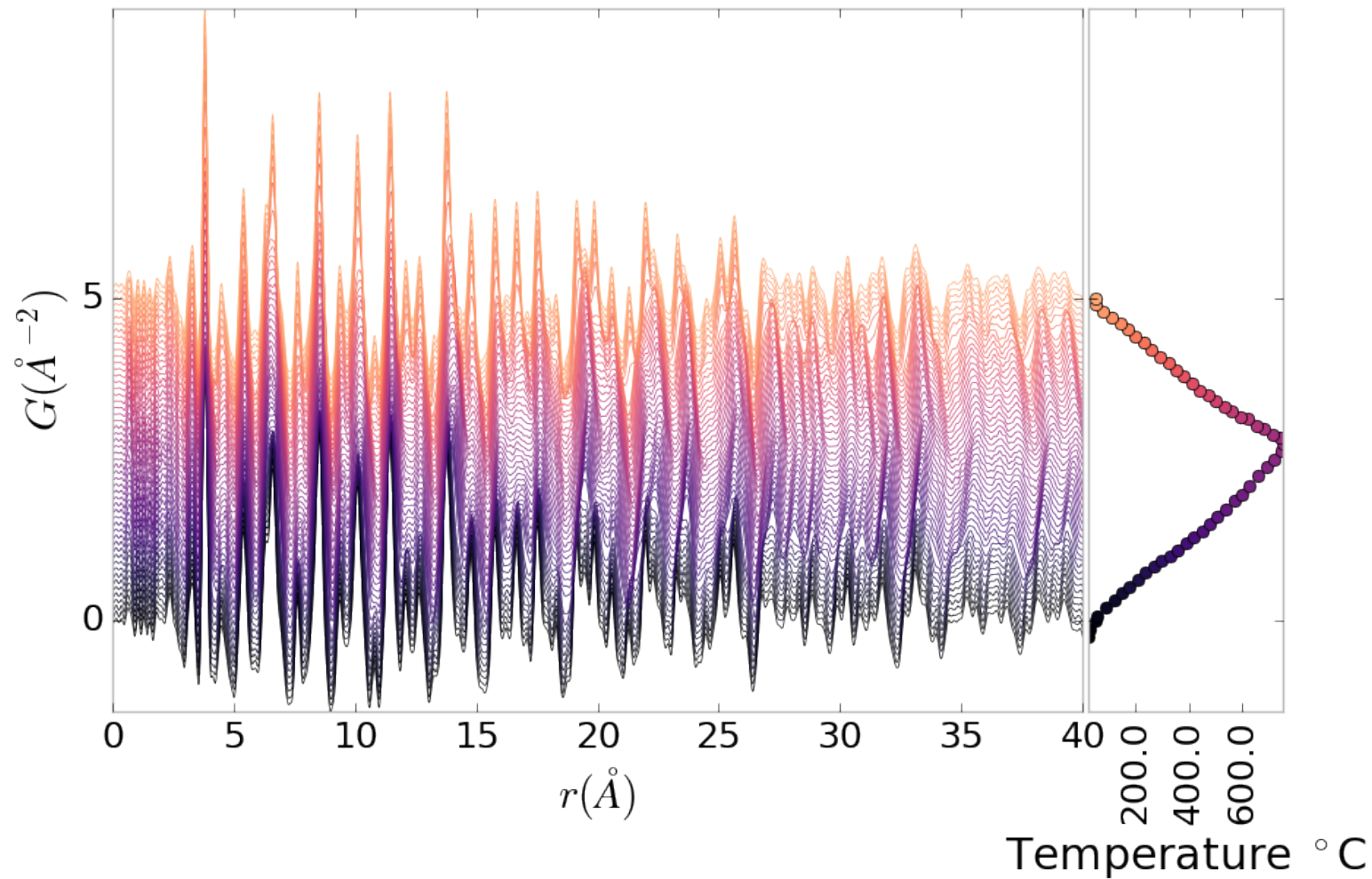


Figure A.5: PDF as a function of temperature for PNO annealed at 750 °C for 200 hours showing the full PDF

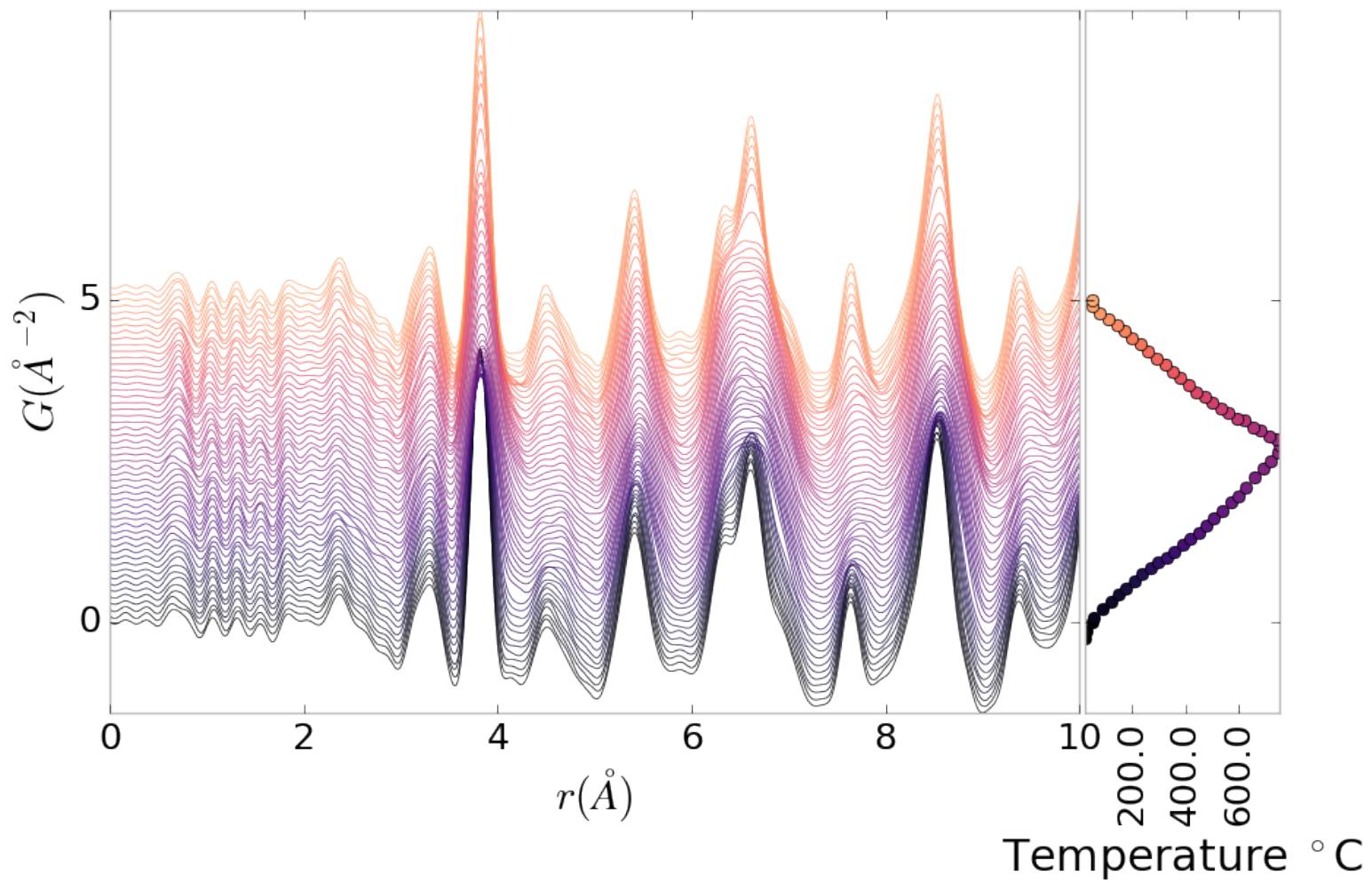


Figure A.6: PDF as a function of temperature for PNO annealed at $750 \text{ } ^{\circ}\text{C}$ for 200 hours showing a close up on the short range section

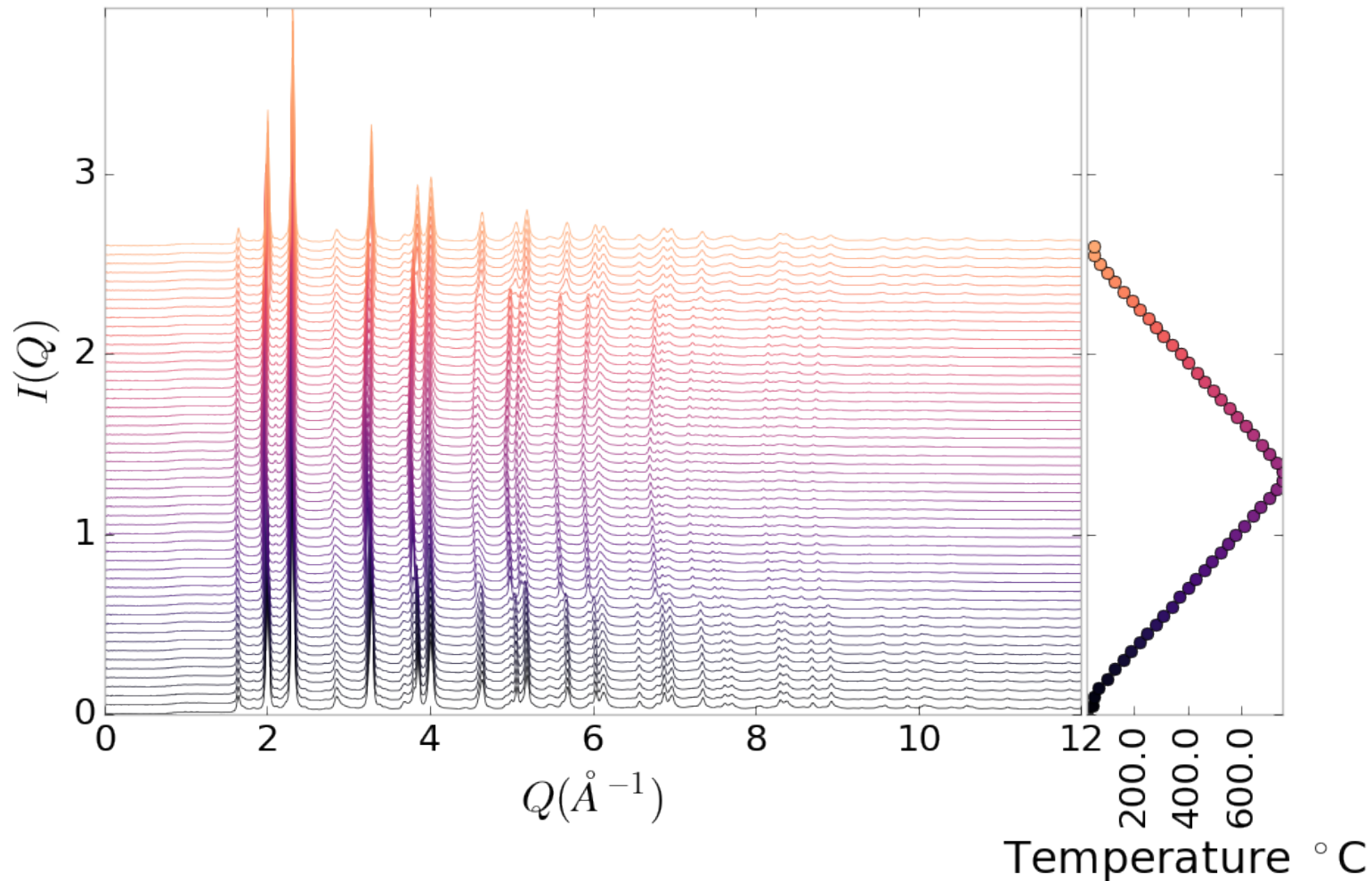


Figure A.7: $I(Q)$ as a function of temperature for PNO annealed at 750 °C for 50 hours showing the full XRD

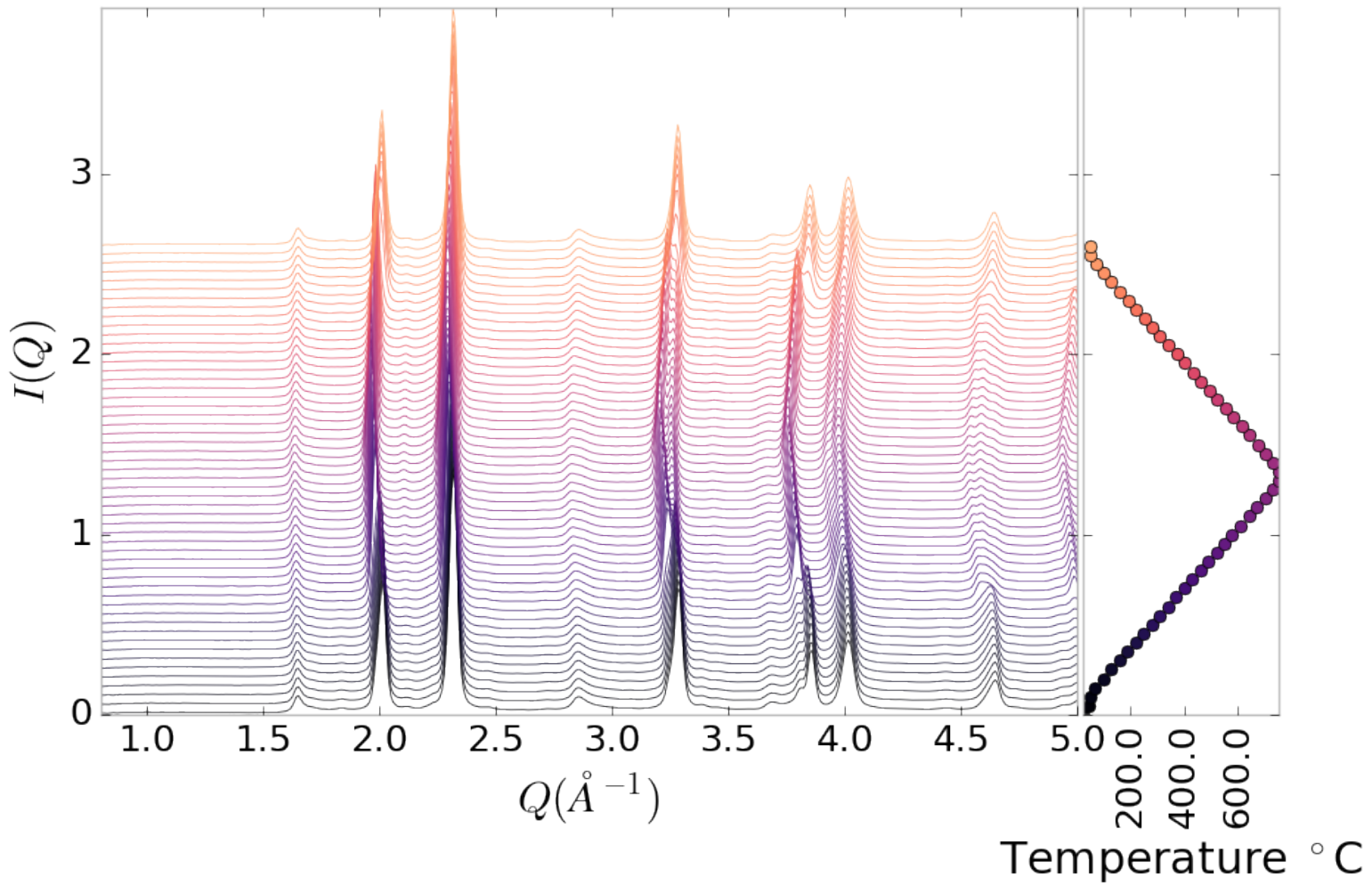


Figure A.8: $I(Q)$ as a function of temperature for PNO annealed at 750 $^{\circ}\text{C}$ for 50 hours showing a close up on the low Q section

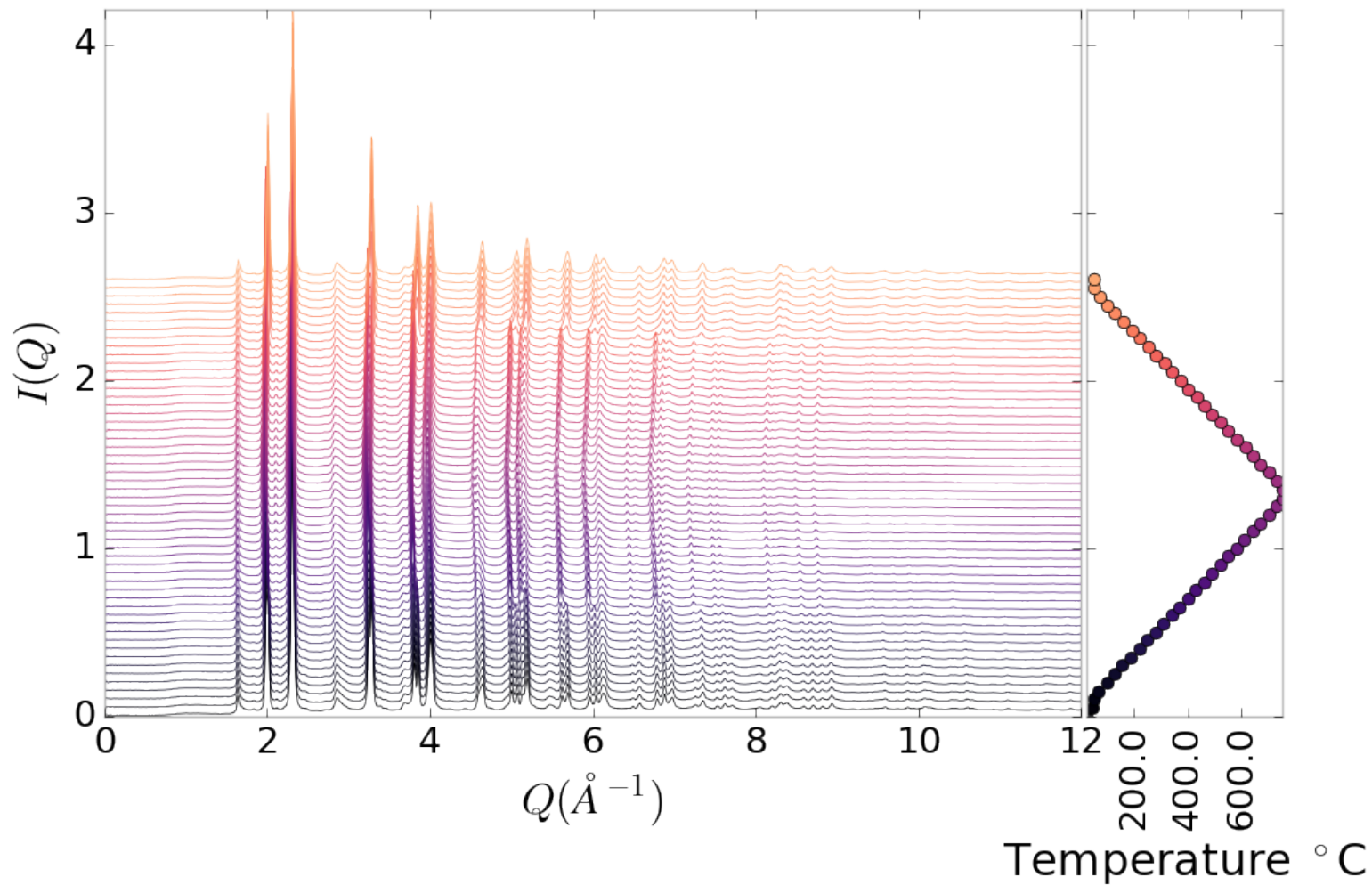


Figure A.9: $I(Q)$ as a function of temperature for PNO annealed at 750 °C for 100 hours showing the full XRD

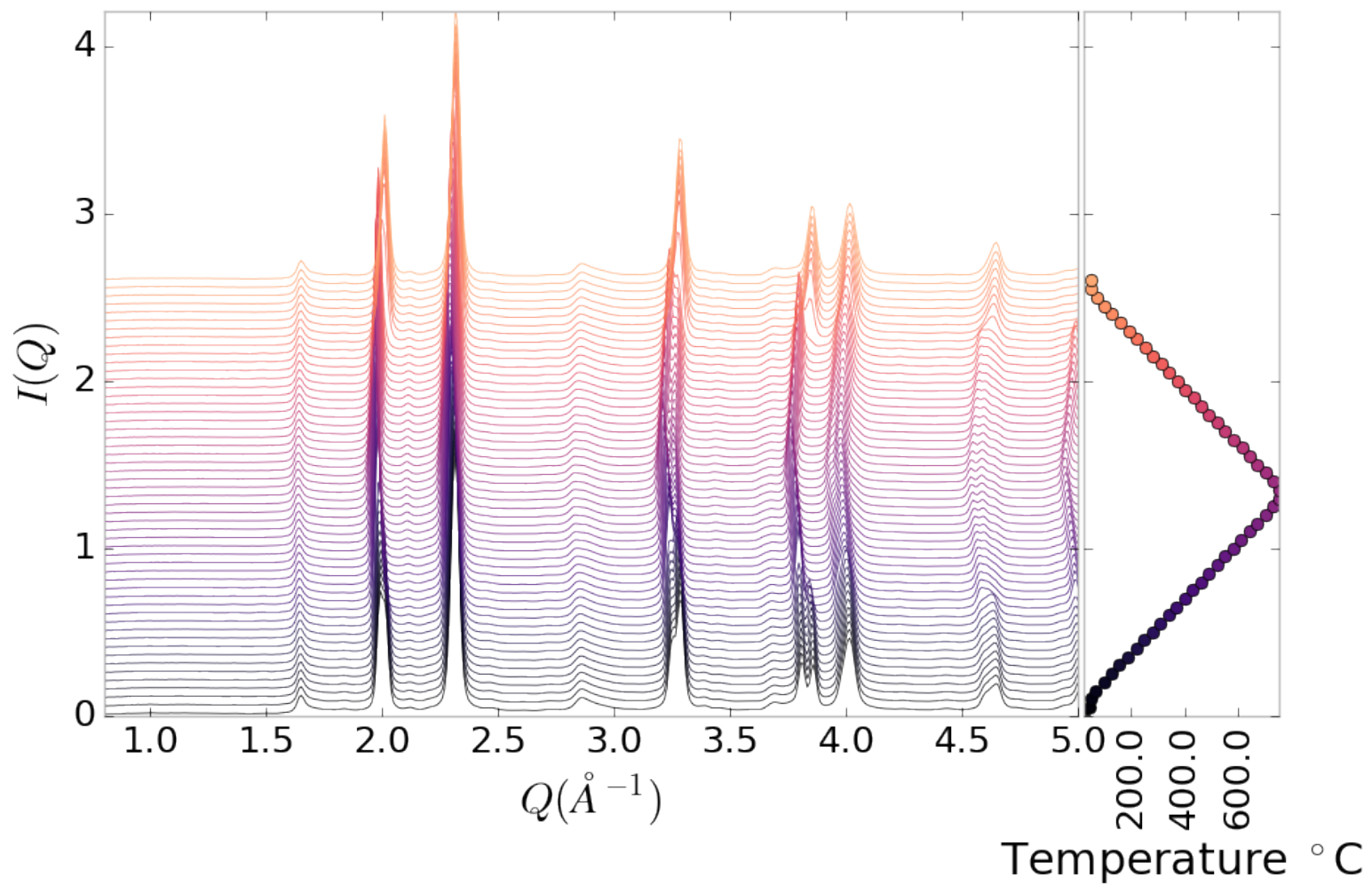


Figure A.10: $I(Q)$ as a function of temperature for PNO annealed at 750 °C for 100 hours showing a close up on the low Q section

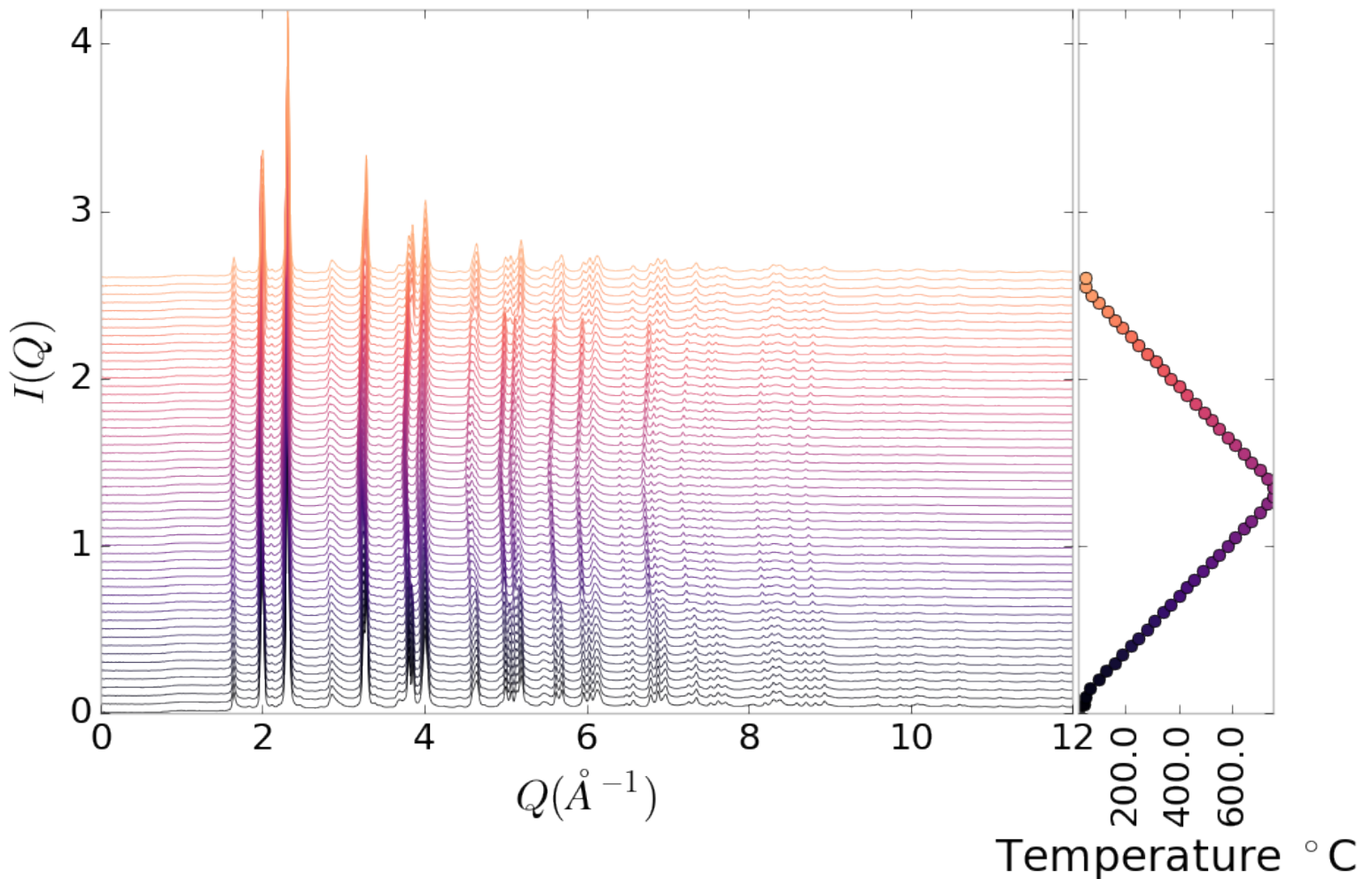


Figure A.11: $I(Q)$ as a function of temperature for PNO annealed at 750 $^{\circ}\text{C}$ for 200 hours showing the full XRD

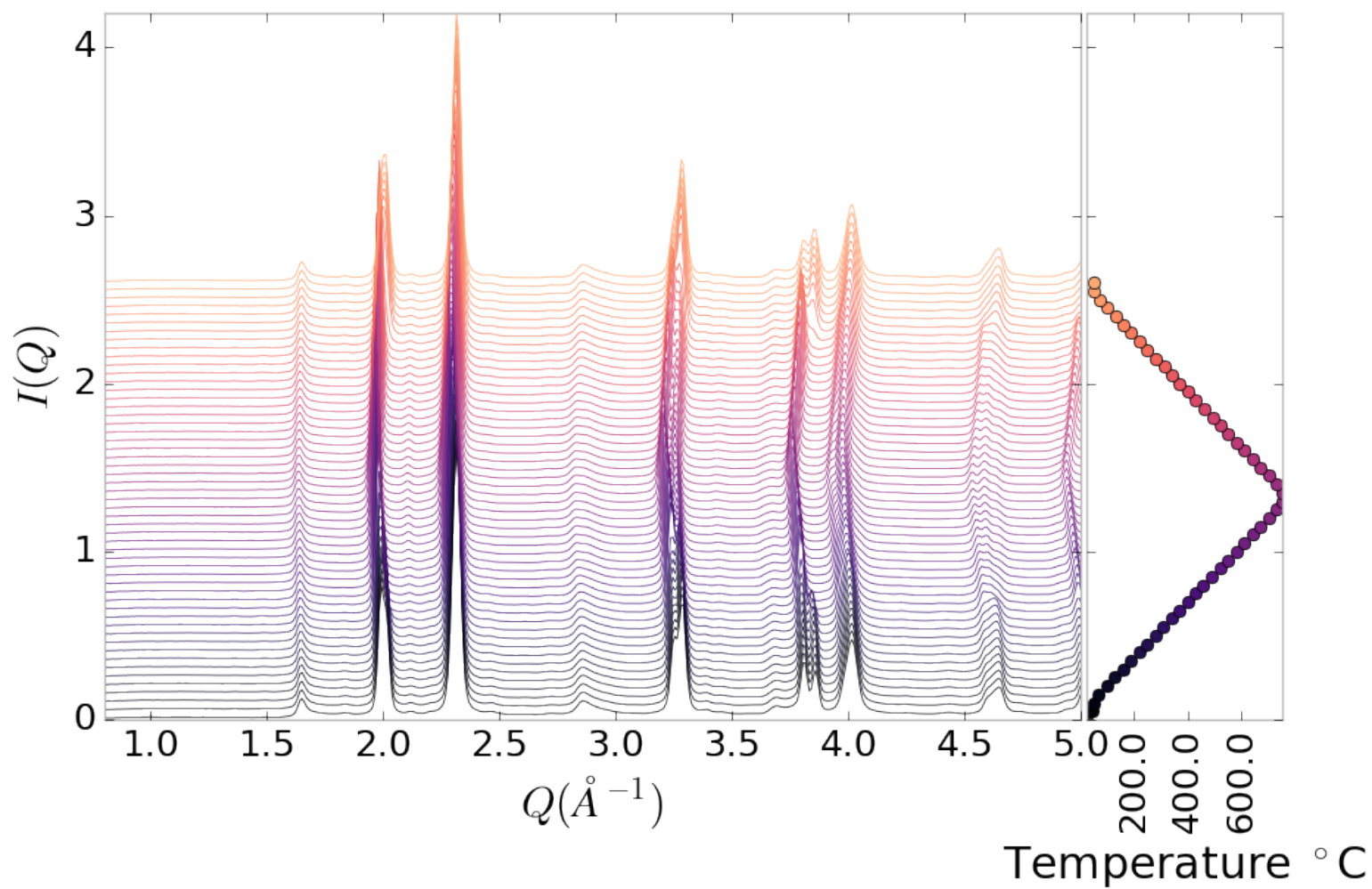


Figure A.12: $I(Q)$ as a function of temperature for PNO annealed at 750 °C for 200 hours showing a close up on the low Q section

Inter Sample Comparison

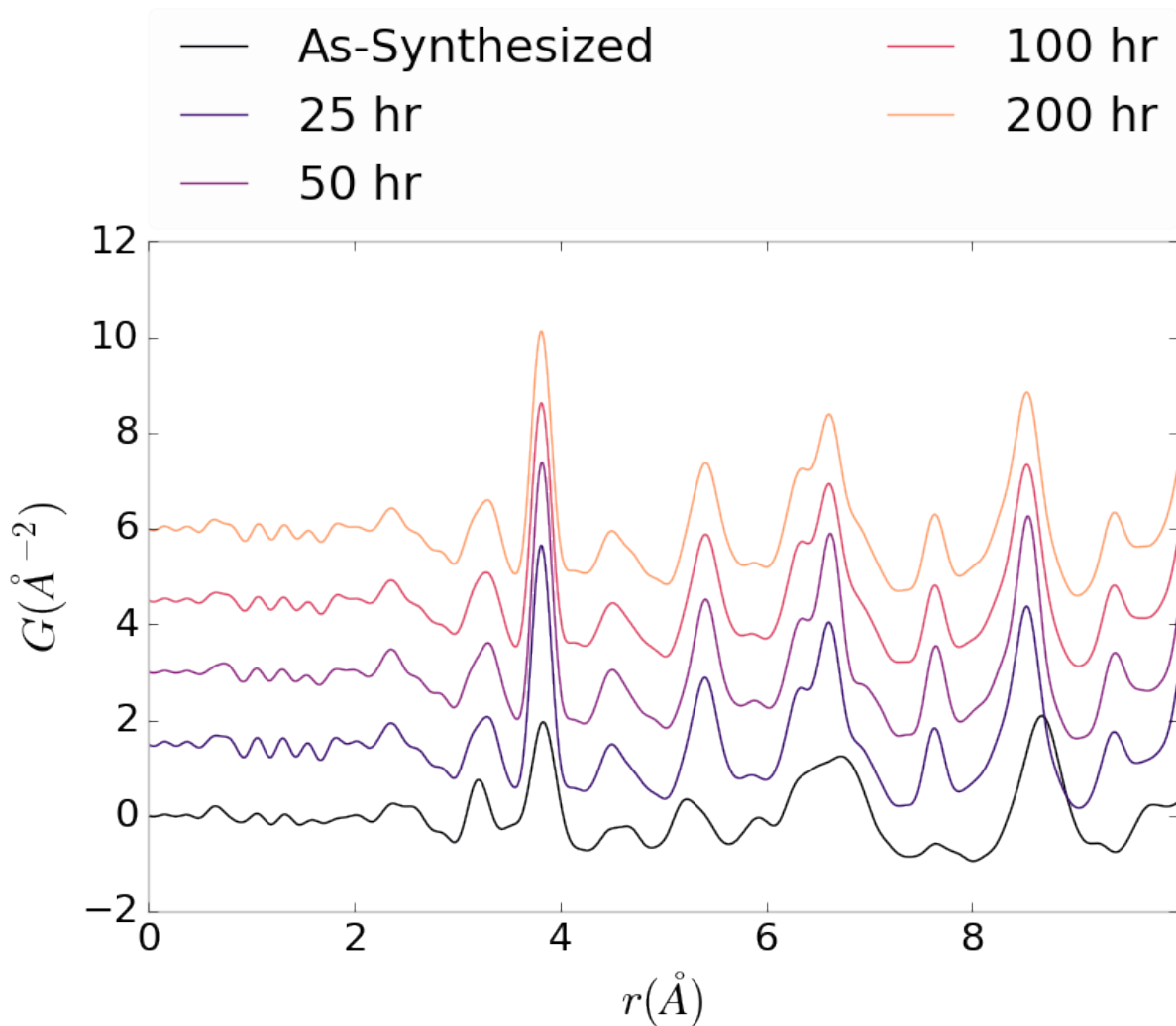


Figure A.13: Comparison of PNO sample PDFs as a function of annealing time at room temperature

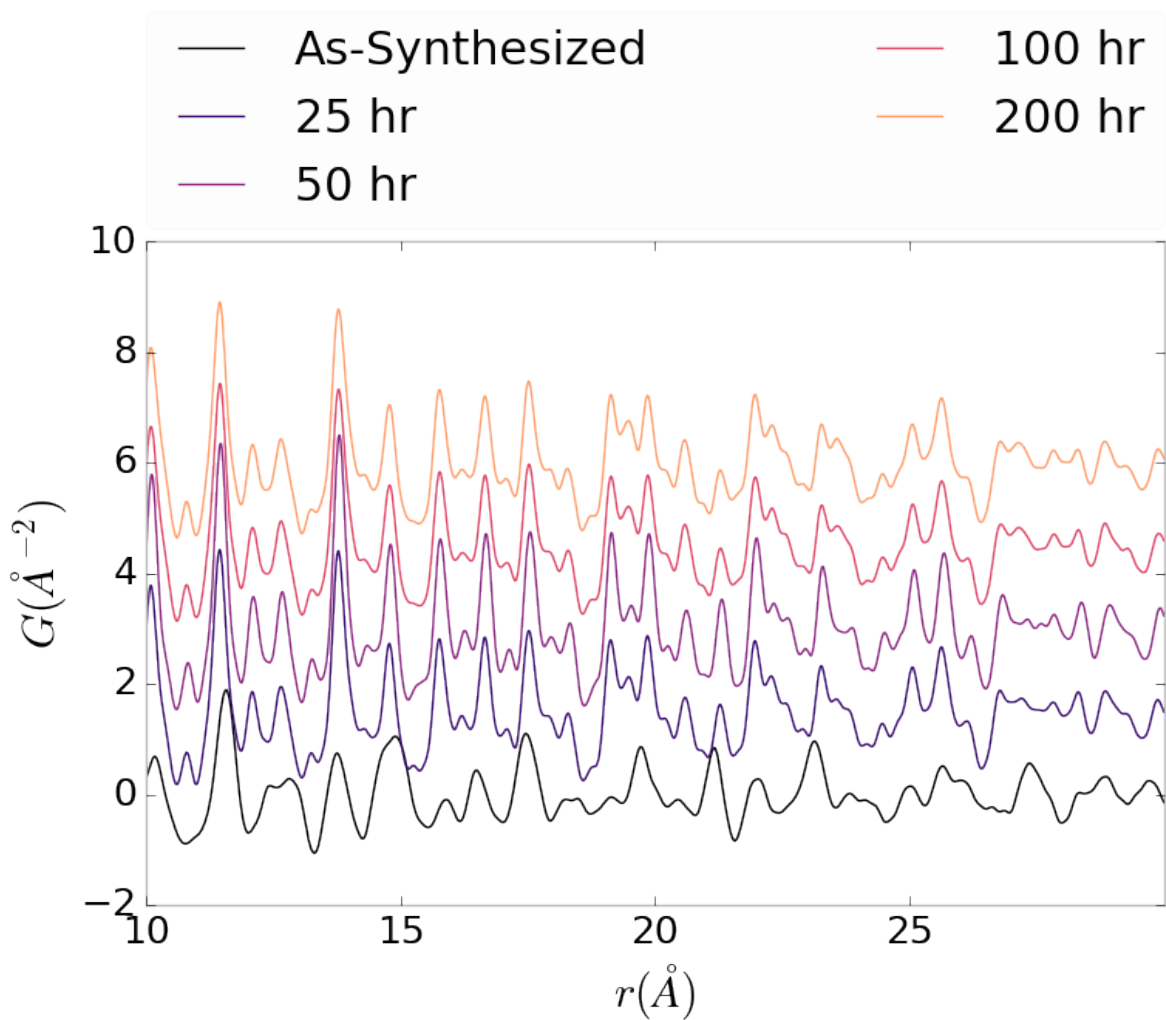


Figure A.14: Comparison of PNO sample PDFs as a function of annealing time at room temperature

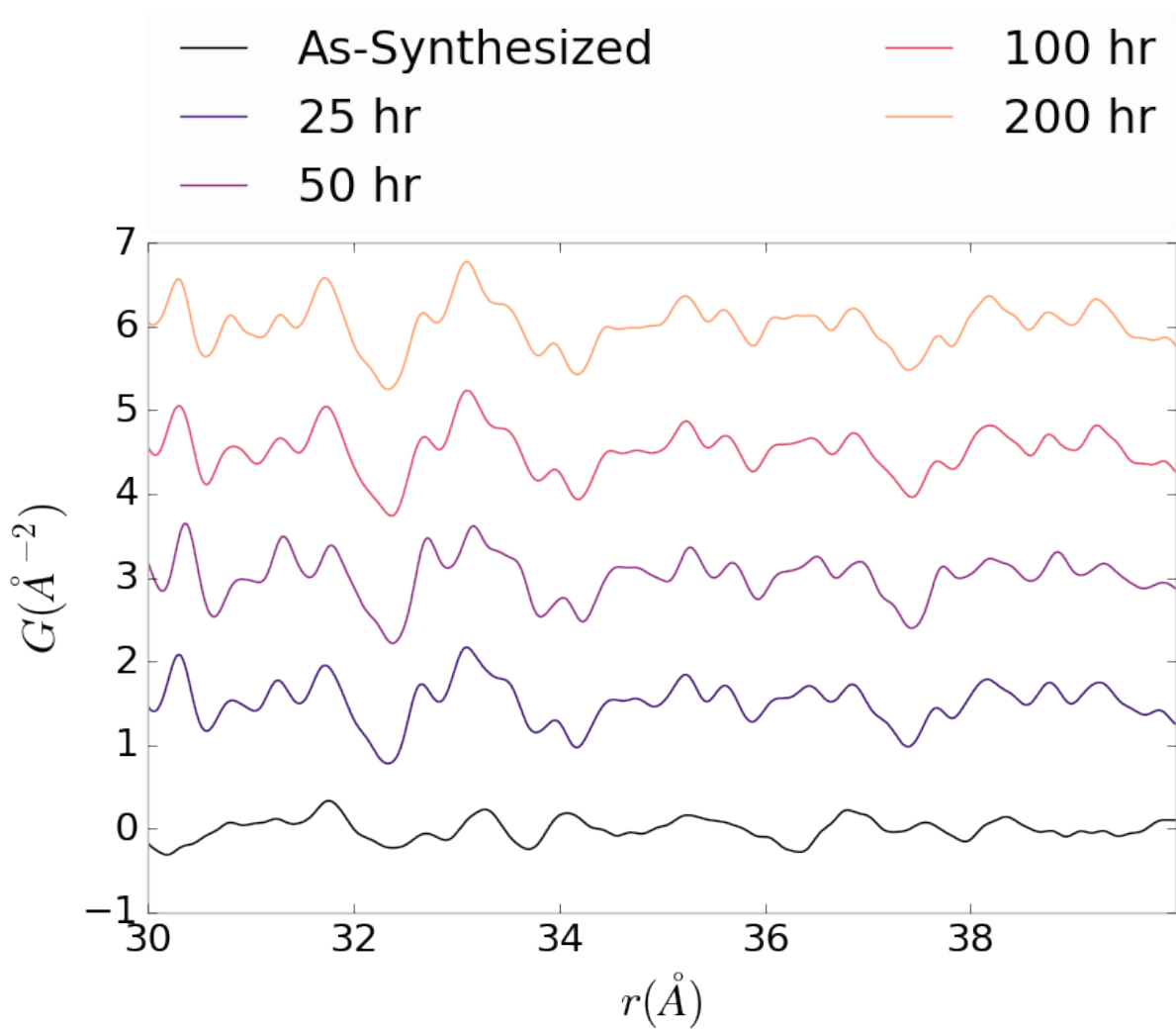


Figure A.15: Comparison of PNO sample PDFs as a function of annealing time at room temperature

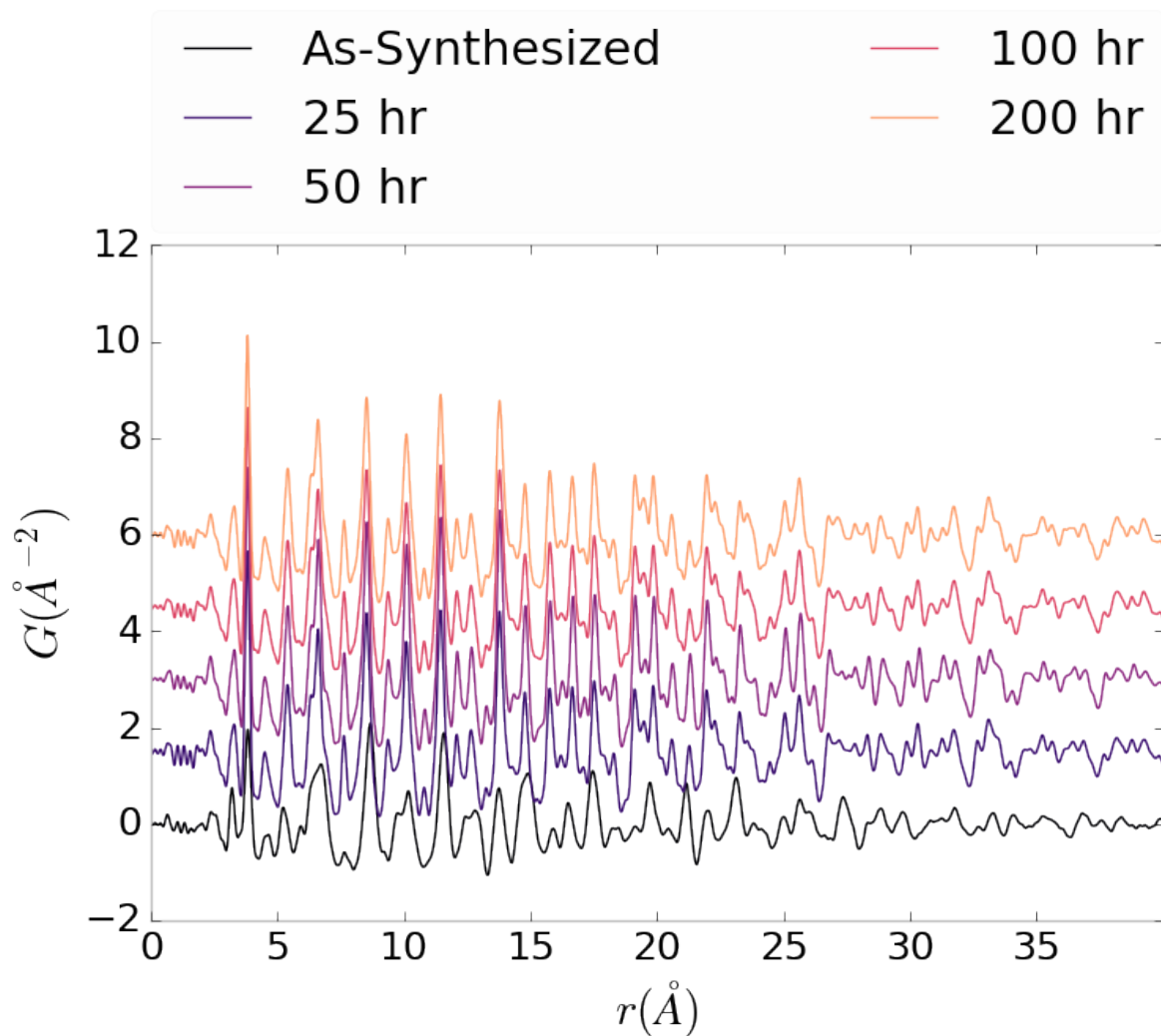


Figure A.16: Comparison of PNO sample PDFs as a function of annealing time at room temperature

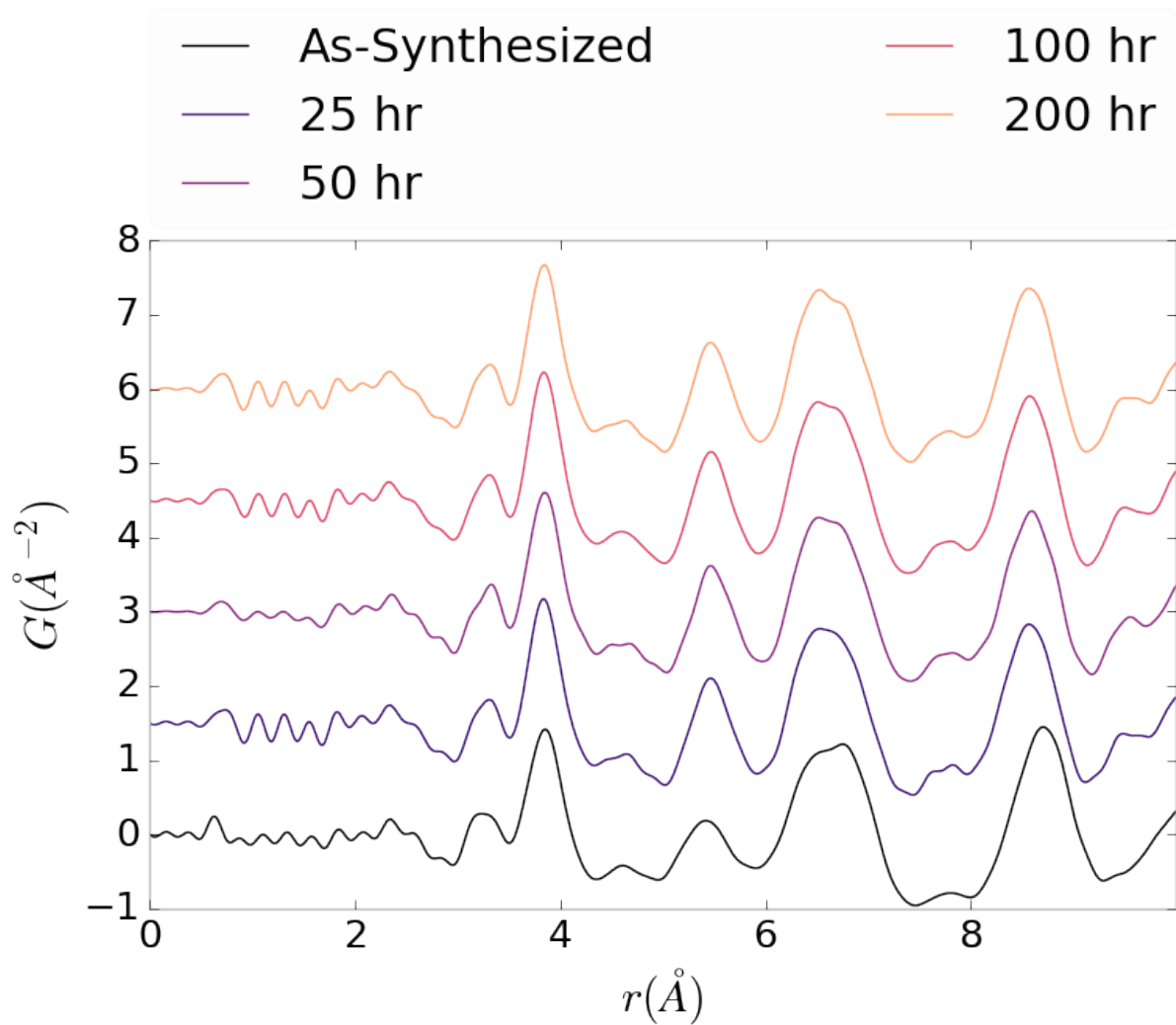


Figure A.17: Comparison of PNO sample PDFs as a function of annealing time at operating temperature

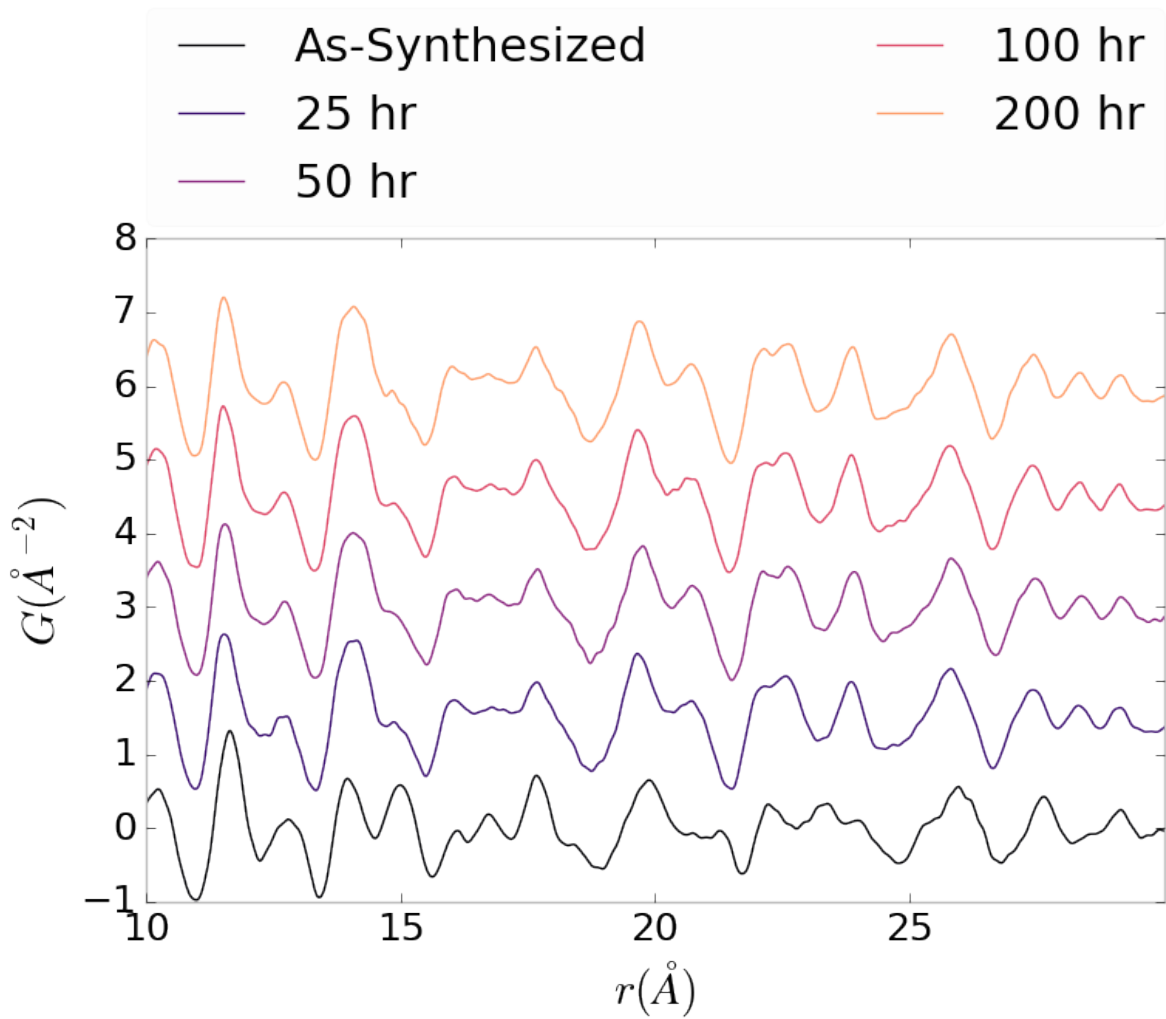


Figure A.18: Comparison of PNO sample PDFs as a function of annealing time at operating temperature

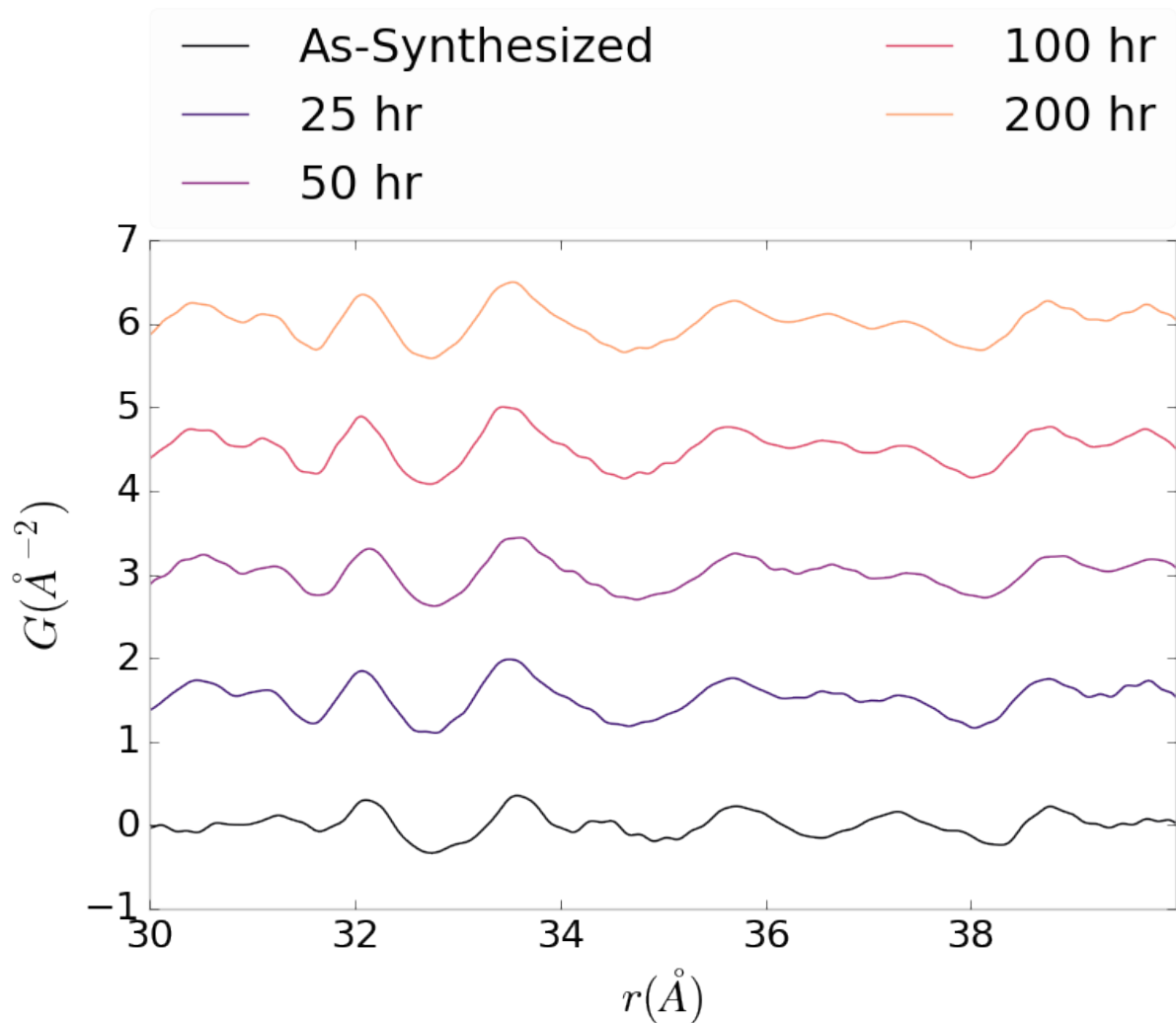


Figure A.19: Comparison of PNO sample PDFs as a function of annealing time at operating temperature

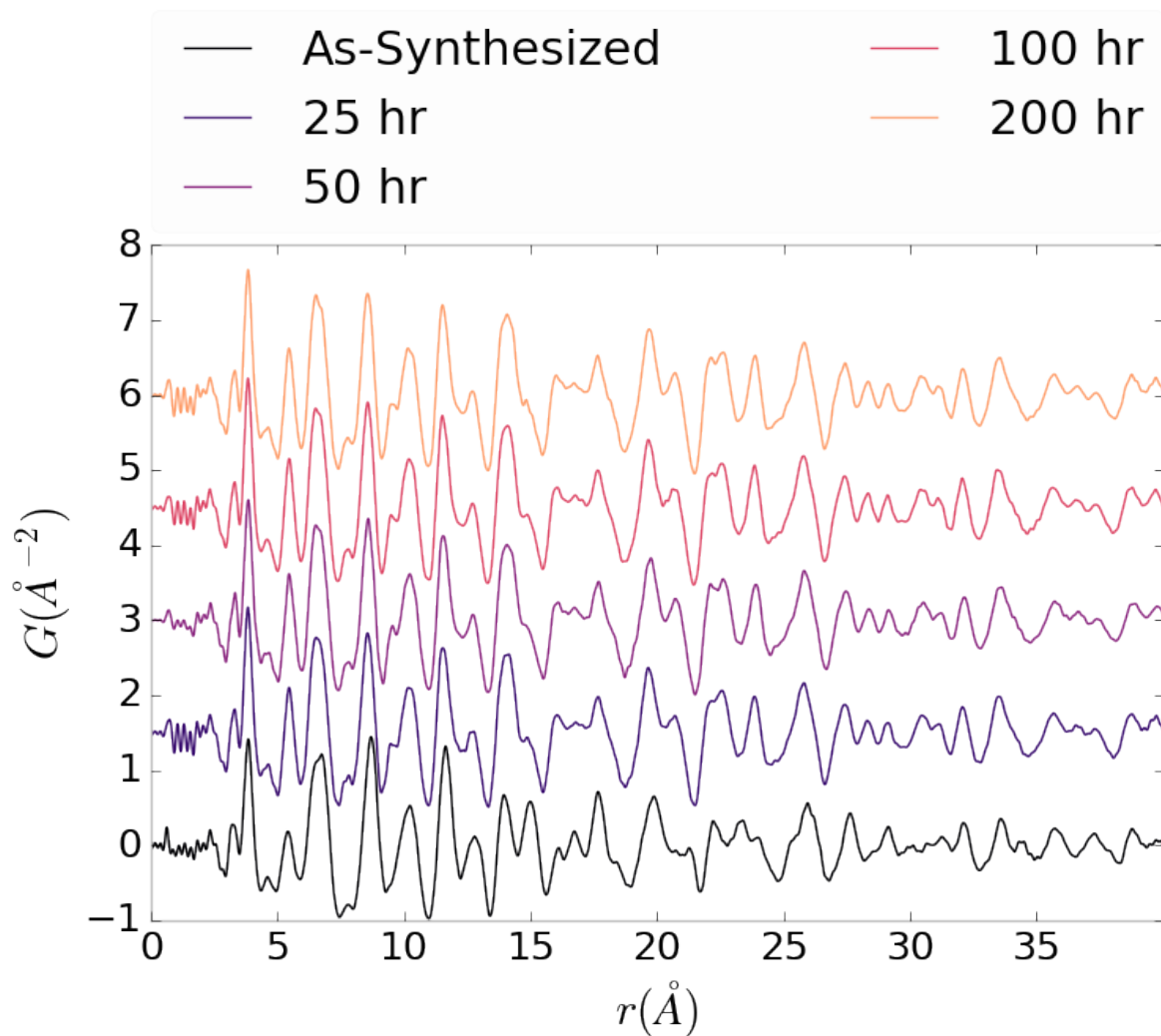


Figure A.20: Comparison of PNO sample PDFs as a function of annealing time at operating temperature

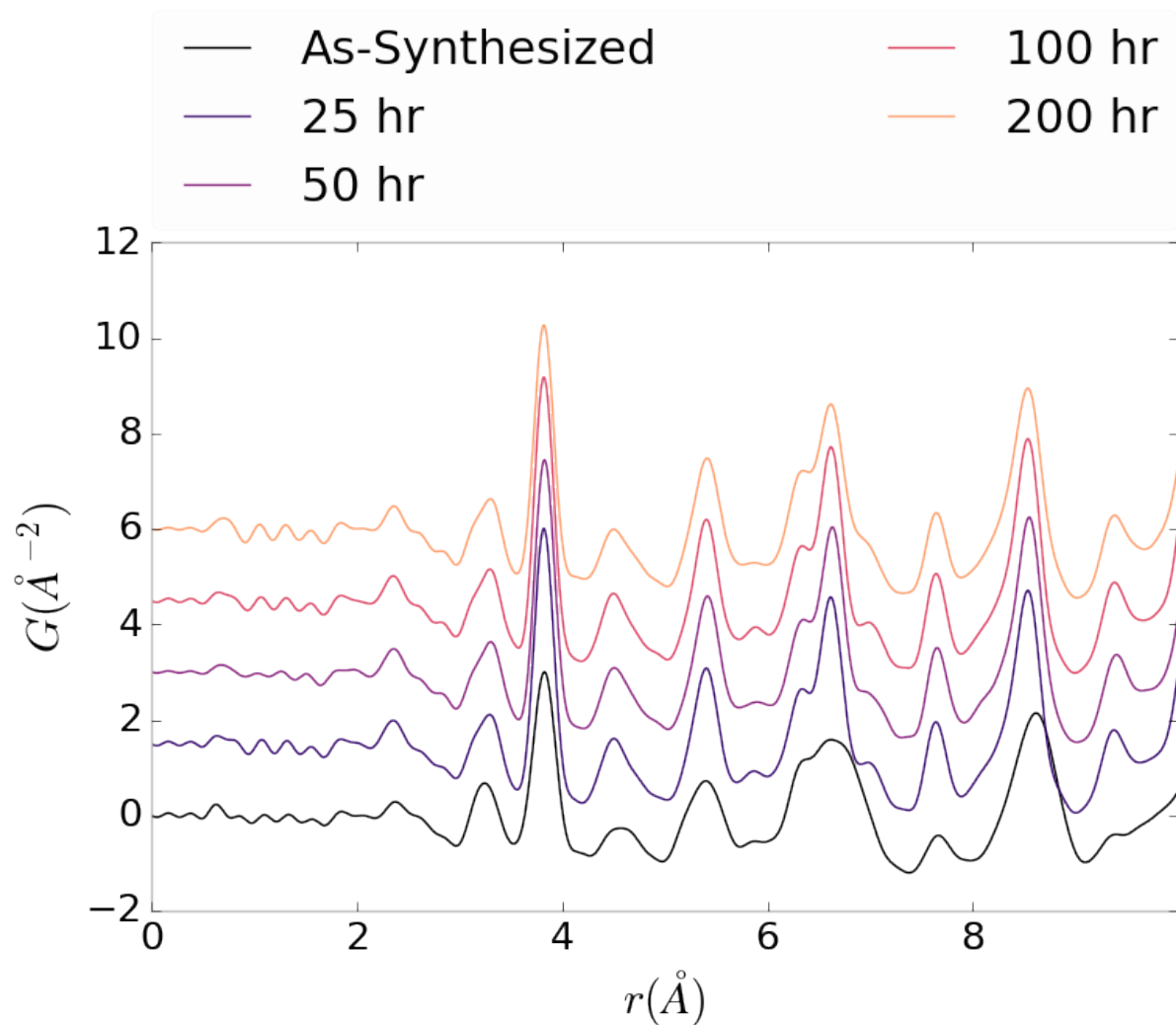


Figure A.21: Comparison of PNO sample PDFs as a function of annealing time cooled back to room temperature

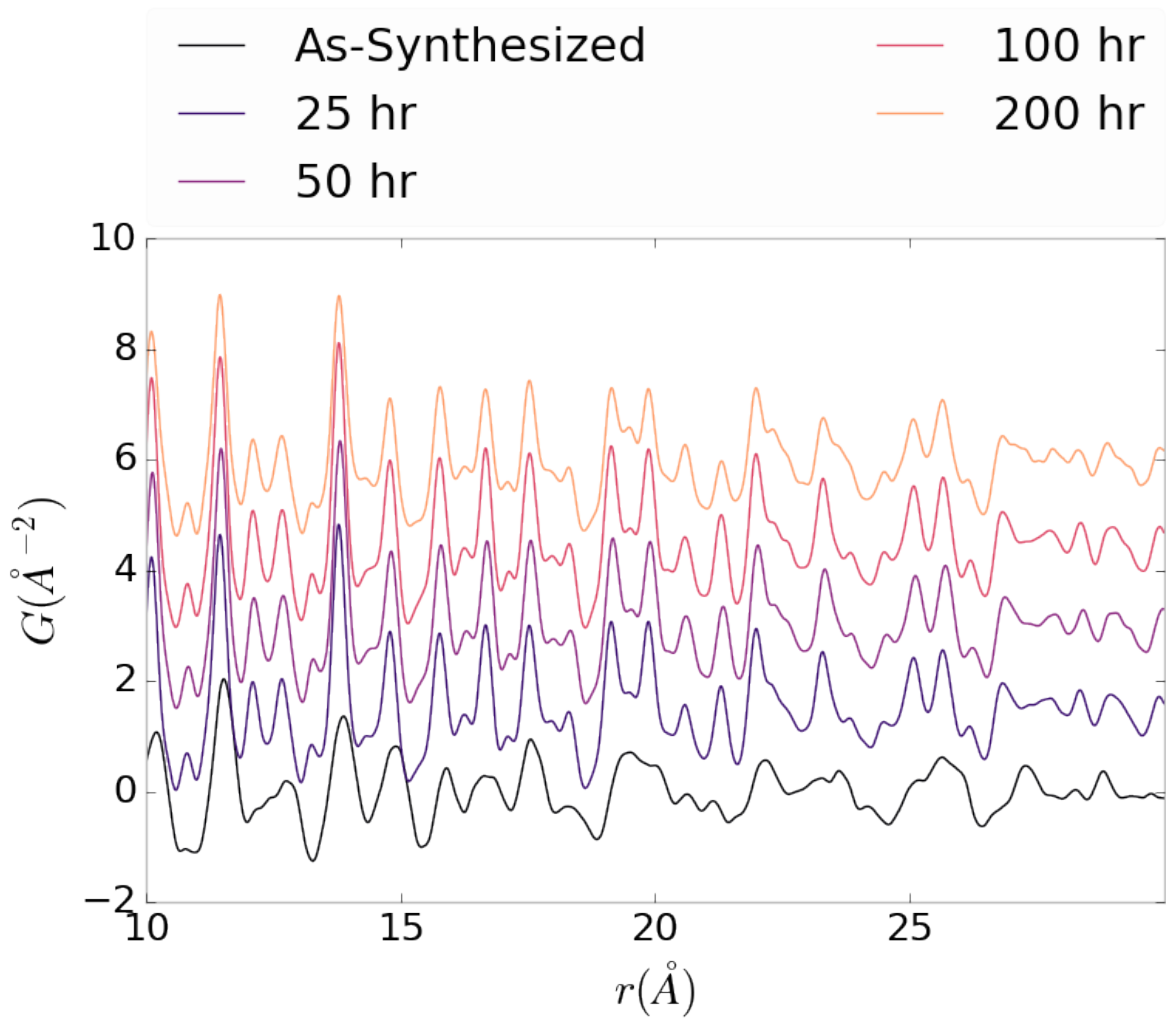


Figure A.22: Comparison of PNO sample PDFs as a function of annealing time cooled back to room temperature

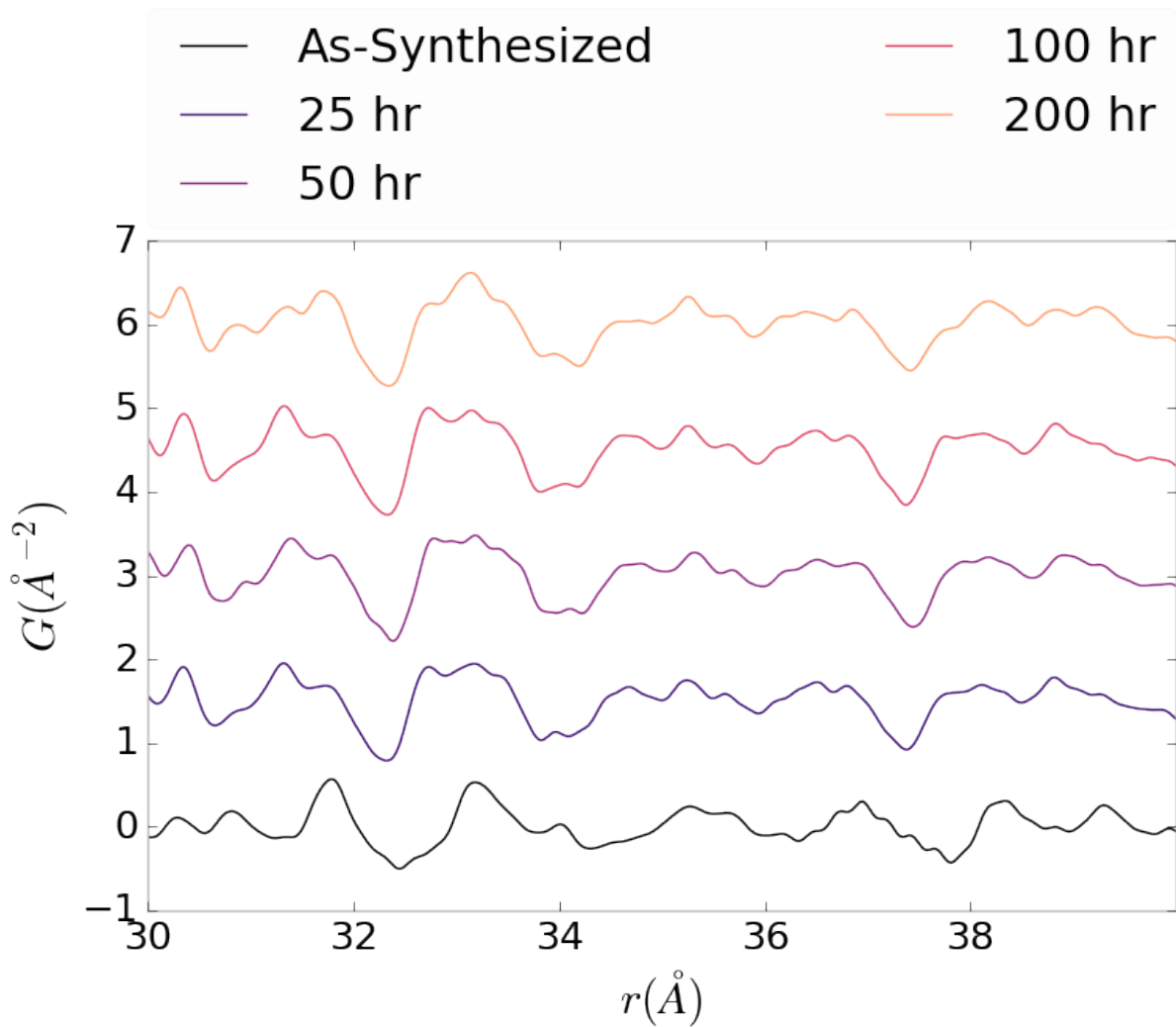


Figure A.23: Comparison of PNO sample PDFs as a function of annealing time cooled back to room temperature

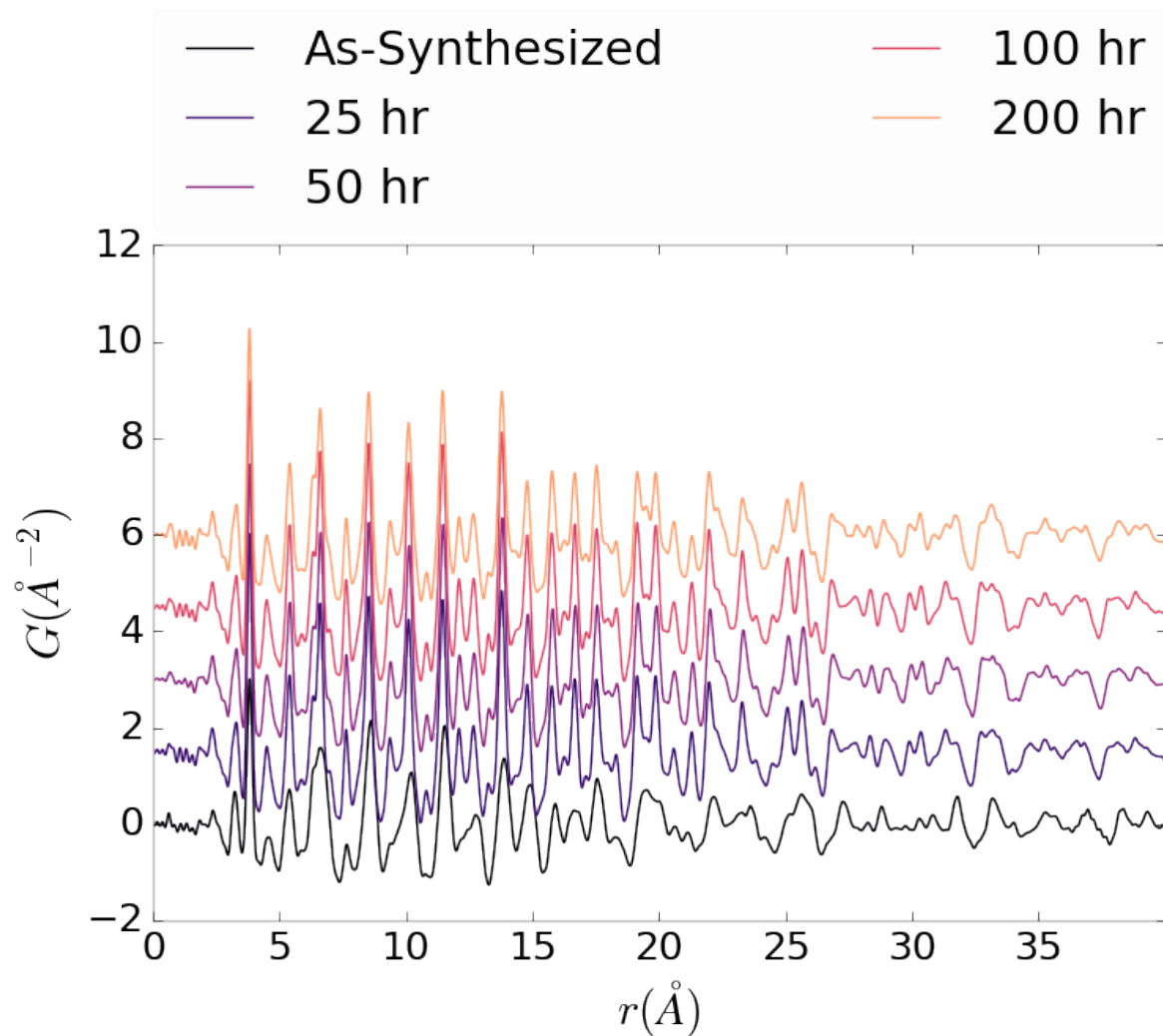


Figure A.24: Comparison of PNO sample PDFs as a function of annealing time cooled back to room temperature

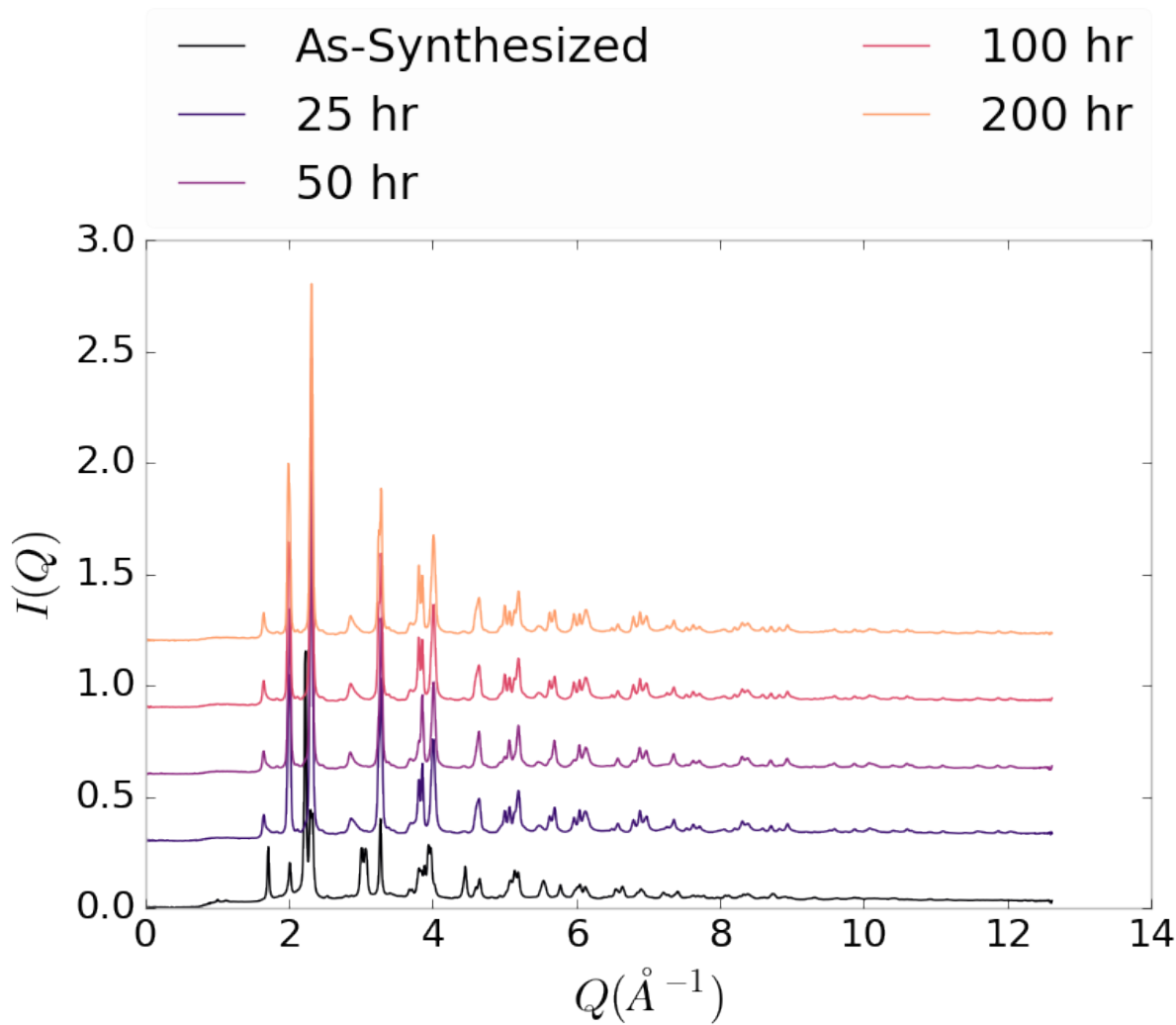


Figure A.25: Comparison of PNO sample $I(Q)$ as a function of annealing time at room temperature

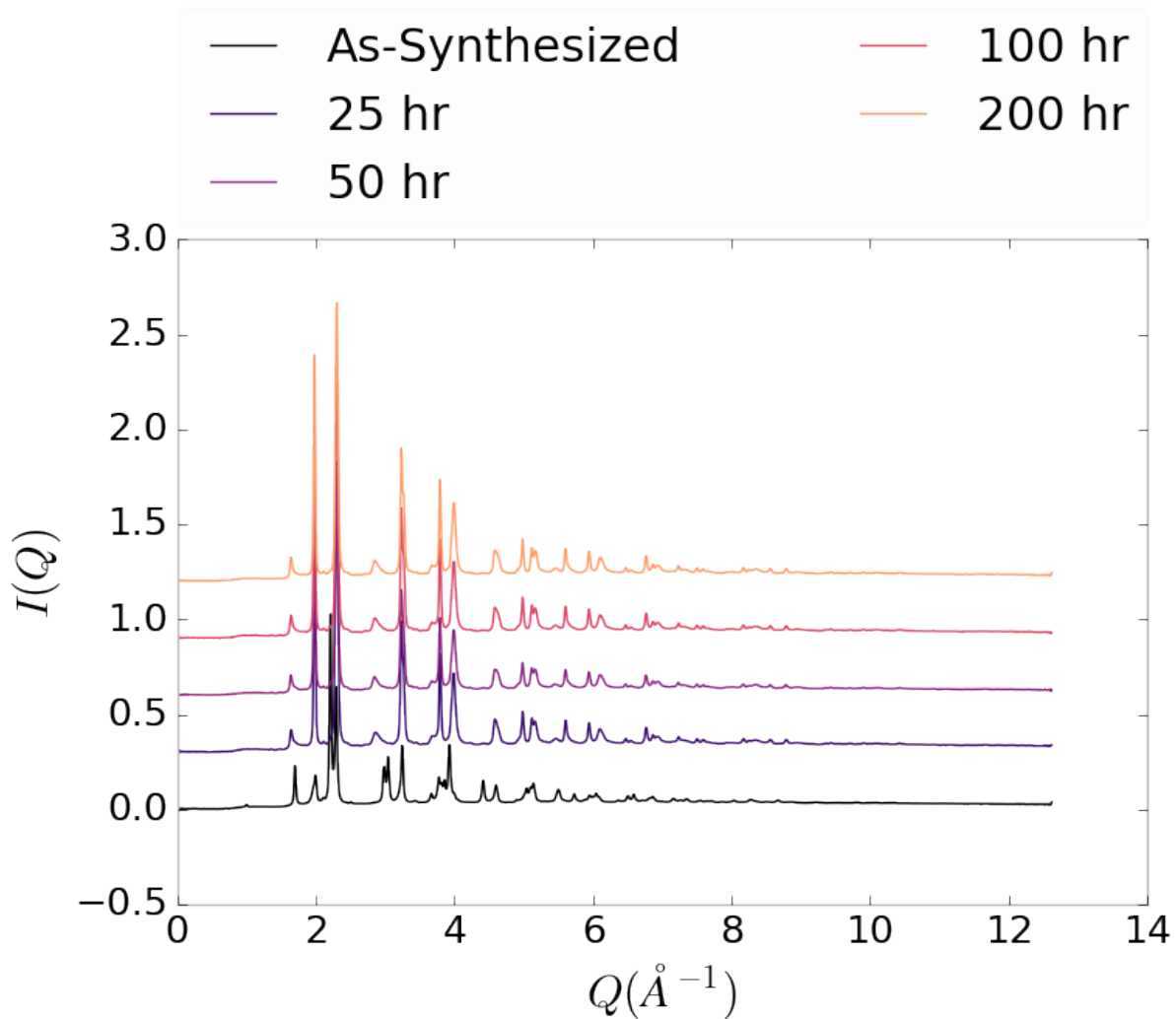


Figure A.26: Comparison of PNO sample $I(Q)$ as a function of annealing time at operating temperature

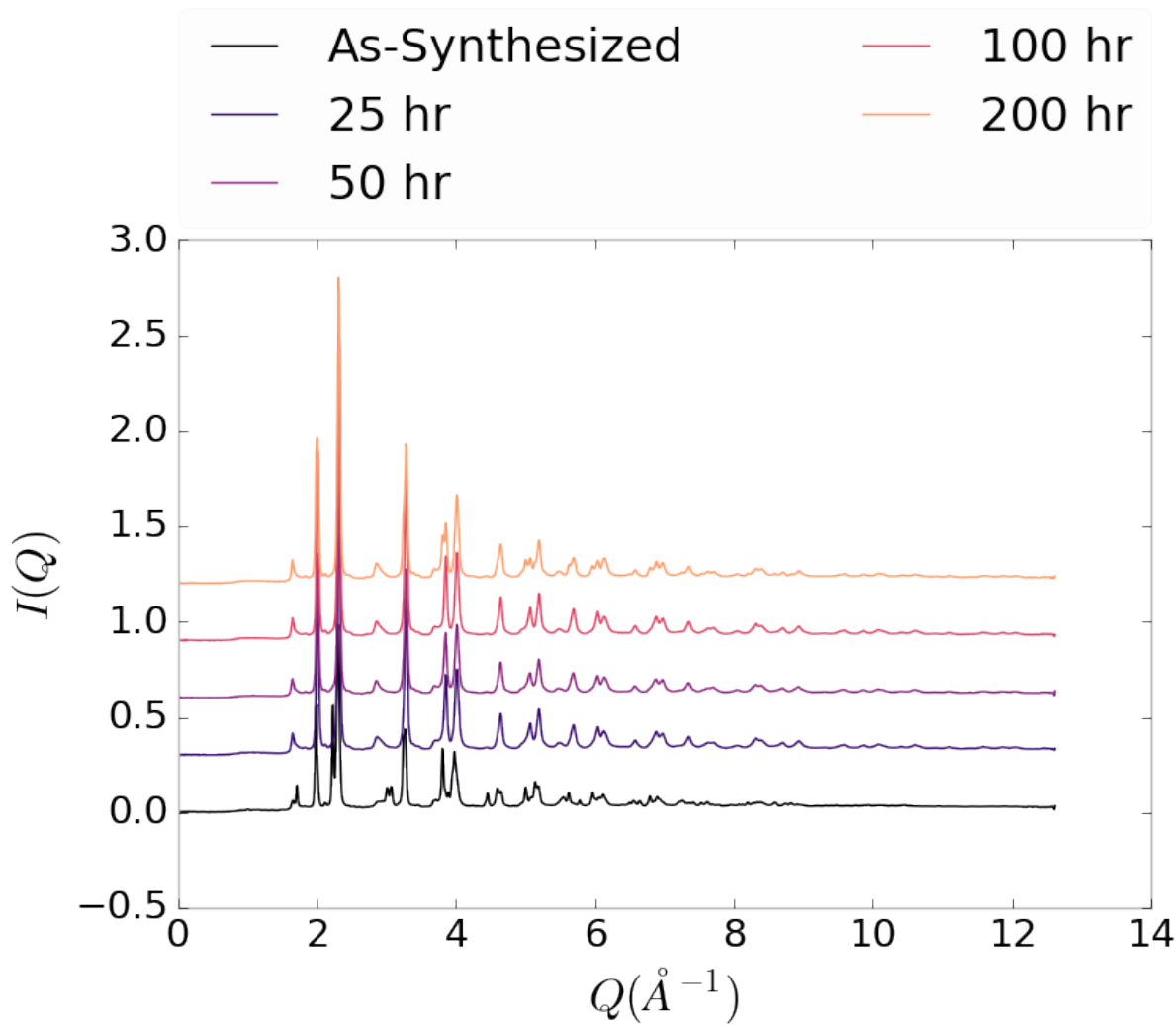


Figure A.27: Comparison of PNO sample $I(Q)$ as a function of annealing time cooled back to room temperature